Updated Geoneutrino Measurement with the Borexino Detector

Aktualisierte Geoneutrino-Messung mit dem Borexino-Detektor

von
Sindhujha Kumaran

Master arbeit in Physik
vorgelegt der
Fakultät für Mathematik, Informatik und Naturwissenschaften
der
RWTH AACHEN

September 2018

angefertigt im
Physikalischen Institut III. B

Erstgutachter und Betreuer
Prof. Dr. Livia Ludhova
Physikalischen Institut III. B
RWTH Aachen

Zweitgutachter
Prof. Dr. Achim Stahl
Physikalischen Institut III. B
RWTH Aachen

Ich versichere, dass ich die Arbeit selbstständig verfasst und keine anderen als die angegebenen Quellen und Hilfsmittel benutzt sowie Zitate kenntlich gemacht habe.

Aachen, den

To my dearest brother, Aswin.

"That you are here—that life exists and identity,
That the powerful play goes on, and you may contribute a verse."
-O Me! O Life!, Walt Whitman

Abstract

Geoneutrinos are electron antineutrinos and neutrinos emitted in the radioactive decays from the Earth's interior. Due to the intrinsic dependence of the geoneutrino flux and the heat produced in the radioactive decays, geoneutrinos contribute uniquely to our knowledge about the Earth. The main goal of neutrino geophysics is to use the obtained geoneutrino signals in estimating the abundance and distribution of the heat producing elements such as ^{238}U, ^{235}U, ^{232}Th and ^{40}K. The radiogenic heat contribution, especially the mantle contribution to the total surface heat flux and the nature of the mantle still remain as open questions. The combination of the total geoneutrino flux ($\approx 10^{6}$ cm^{-2}s^{-1}) and the weak interaction cross section ($\approx 10^{-42}$ cm^{-2}s^{-1}) lead to huge statistical uncertainties in the current measurements. This has made the study of geoneutrinos quite challenging and so far, only two detectors, namely KamLAND and Borexino, have measured geoneutrinos.

The Borexino Detector located at the Laboratori Nazionali del Gran Sasso (LNGS), Italy first observed geoneutrinos in 2010 followed by two measurements in 2013 and 2015. The latest geoneutrino measurement included a 5.9σ evidence of geoneutrinos and the rejection of the null hypothesis of the mantle signal at a 98% C.L. The uncertainty in the latest published result is 26.2%. This work concentrates on the further improvement of the geoneutrino measurement. The increased statistics and the optimised selection cuts used for the analysis have made it possible to reduce the uncertainty to 20.6%. An uncertainty of less than 20% can be achieved by the further optimisation of the selection cuts and needs more investigation.

Contents

1 Geoneutrinos

Geoneutrinos are electron antineutrinos and neutrinos coming from the radioactive decays occuring inside Earth. Geoneutrinos aid in studying the abundance and distribution of the Heat Producing Elements (HPE) causing these radioactive decays. Almost 99% of the Earth's radiogenic heat is produced in the radioactive decays of ^{232}Th, ^{235}U, ^{238}U, and ^{40}K. The flux of the geoneutrinos from these decays provides the direct measurement of the abundances of HPE and their respective contribution to the radiogenic heat. This helps in calculating the radiogenic heat contribution to the total surface heat flux and the mantle contribution can be extracted using the relatively well known crustal contribution.

$$^{238}U \rightarrow^{206} Pb + 8\alpha + 8e^{-} + 6\bar{\nu_e} + 51.7 \text{ MeV} \tag{1.0.1}$$

$$^{235}U \rightarrow^{207} Pb + 7\alpha + 4e^{-} + 4\bar{\nu_e} + 46.4 \text{ MeV} \tag{1.0.2}$$

$$^{232}Th \rightarrow^{208} Pb + 6\alpha + 4e^{-} + 4\bar{\nu_e} + 42.7 \text{ MeV} \tag{1.0.3}$$

$$^{40}K \rightarrow^{40} Ca + e^{-} + \bar{\nu_e} + 1.31 \text{ MeV } (89.3\%) \tag{1.0.4}$$

$$^{40}K \rightarrow^{40} Ar + \bar{\nu_e} + 1.505 \text{ MeV } (10.7\%) \tag{1.0.5}$$

Since the isotopic abundance of ^{235}U is small, the overall contribution of ^{238}U, ^{232}Th, and ^{40}K is largely predominant. The geoneutrino spectrum extends up to 3.26 MeV and the contributions originating from different elements can be distinguished according to their different end points, that is, geoneutrinos with energy greater than 2.25 MeV are produced only due to the Uranium chain. ^{232}Th is more abundant than ^{238}U and their mass ratio in the bulk Earth is expected to be m(^{232}Th)/m(^{238}U) = 3.9. The Earth's radius of ≈6371 km is very large compared to the oscillation length ($L_0 \approx \pi c\hbar\frac{4E}{\Delta m^2_{21}}$) even for a high energy geoneutrino of 3 MeV. Thus, the effect of neutrino oscillation to the total neutrino flux is well averaged, giving an overall survival probability of

$$\langle P_{ee} \rangle \cong \cos^4\theta_{13}(1 - \frac{1}{2}\sin^2 2\theta_{12}) + \sin^4\theta_{13}. \tag{1.0.6}$$

According to the neutrino oscillation mixing angles reported in [5], $P_{ee} \approx 0.54$. The matter effect due to the different electron densities in the Earth contributes to an increase of around 2% in the survival probability and the spectral distortion is below 1%.

1.1 Detection Principle

Geoneutrinos are detected in liquid scintillators through the Inverse Beta Decay (IBD) reaction (Figure 1.1.1):

$$\bar{\nu_e} + p \rightarrow e^{+} + n \tag{1.1.1}$$

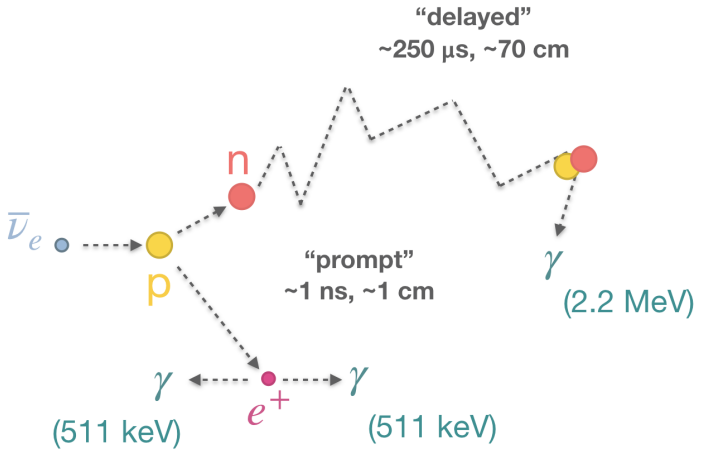

Figure 1.1.1: Schematic of Inverse Beta Decay (IBD) showing the prompt and delayed coincidences.

The IBD kinematic threshold of 1.806 MeV ($\approx(m_n + m_{e+}) - m_p$) as shown in Figure 1.1.2 makes it impossible to measure geoneutrinos coming from ^{40}K and ^{235}U. The emitted positron annihilates with the electron in the scintillator and gives two annhilation γ's of energy 1.22 MeV (2x0.511 MeV). This acts as the prompt signal of IBD interaction and its energy can be given as E_{prompt} = E_{geonu} - 1.806 + 1.22 MeV = E_{geonu} - 0.784 MeV. The neutron emitted can be captured by the protons (2.2 MeV γ) or other materials in scintillator detectors and it is the delayed signal of the IBD interaction. The typical flux of geoneutrinos is around 10^6 cm^{-2}s^{-1} and the cross section of the IBD interaction is of the order 10^{-42} cm^2. This leads to only a hand-full number of interactions, few or few tens per year with the current size detectors.

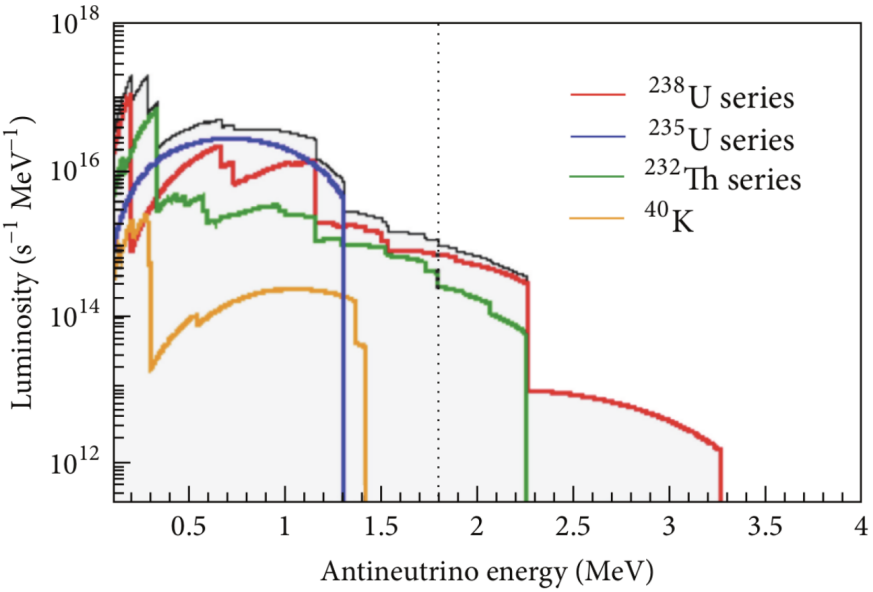

Figure 1.1.2: Geoneutrino luminosity as a function of energy shown for the most important reaction chains and nuclides [42]. Only geoneutrinos of energies above the 1.8 MeV energy (dashed black line) can be detected by means of IBD.

1.2 Structure of the Earth

The Earth was created in the process of accretion from undifferentiated material, to which chondritic meteorites are believed to be the closest in composition and structure. Bodies with a sufficient mass undergo the process of differentiation, for example, a transformation from an ho-

mogenous object to a body with a layered structure. A schematic representation of the different layers of Earth is shown in 1.2.1.

Core The metallic core of the Earth began to differentiate and today the core has a radius of 2890 km (about 45% of the Earth radius) and represents less than 10% of the total Earth volume [42]. From seismologic studies, the fact that transverse/shear waves do not propagate through the so called Outer core, we know that is it liquid where turbulent convection occurs. These movements have a crucial role in the process of the generation of the Earth's magnetic field. The chemical composition of the core is inferred indirectly as Fe-Ni alloy with up to 10% admixture of light elements, most probable being oxygen or sulphur. There are also other arguments such as a ^{40}K powered or U-driven georeactor. Later, the rest of Earth's volume composed of presumably homogeneous Primitive Mantle built of silicate rocks differentiated into the present mantle and crust.

Mantle Above the Core Mantle Boundary (CMB), there is a ≈200 km thick zone called D" (pronounced D-double prime), a seismic discontinuity characterized by a decrease in the gradient of both P (primary) and Secondary (S) wave velocities. The origin and character of this narrow zone is under discussion and there is no widely accepted model.
The Lower Mantle is about 2000 km thick and extends from the D" zone up to the seismic discontinuity at the depth of 660 km [42]. This discontinuity does not represent a chemical boundary while a zone of a phase transition and mineral recrystallization. The dominant mineral phases are perovskite, ferropericlase, and Ca-perovskite. The temperature at the base of the mantle can reach 3700 K while at the boundary the temperature is about 600 K. The Lower mantle is solid because of the high lithostatic pressure but vicose and undergoes plastic deformation on long time-scales. Due to the high temperature gradient and the ability of the mantle to creep, there is an ongoing convection in the mantle. This drives the movement of tectonic plates with characteristic velocities of few cm per year.
The mantle between the two seismic discontinuities at 410 km and 660 km depths is called the Transition Zone. This zone consists primarily of peridotite rock with dominant minerals garnet and high pressure polymorphs of olivine, ringwoodite, and wadsleyite below and above ca. 525 km depth, respectively [42].
In the Upper Mantle above the 410 km depth discontinuity, the dominant minerals are olivine, garnet, and pyroxene. The upper mantle boundary is defined with seismic discontinuity called Mohorovicic often referred to as Moho. It is average depth is about 35 km. The Moho lies within the lithosphere, the mechanically defined uppermost Earth layer with brittle deformations composed of the crust and the brittle part of the upper mantle, Continental Lithospheric Mantle (CLM). The lithospheric tectonic plates are floating on the more plastic asthenosphere entirely composed of the mantle material.

Crust The partial melting of the mantle through geological times due to different temperatures of solid and liquid led to the formation of Earth's crust. The mantle rocks have higher Mg to Fe ratio and a smaller proportion of Si to Al than the crust. Due to the lower density, the crust which is an accumulation of solidified partial liquid, tends to move upwards with respect to the denser solid residual. There are two types of the Earth's crust. The simplest and youngest is the oceanic crust, less than 10 km thick. It is created by partial melting of the Transition-Zone mantle along the mid-oceanic ridges on top of the upwelling mantle plumes. The typical rock types of the oceanic crust created along the rifts are Midoceanic Ridge Basalts (MORB). The continental crust is thicker, more heterogeneous and older and has a more complex history with respect to the oceanic crust. It forms continents and continental shelves covered with shallow waters. Continental crust covers about 40% of the Earth surface [42]. It is much thicker than the oceanic crust, from 20 to 70 km. The average density is less than that of the oceanic crust,

therefore, the continental slab rarely subduct. Therefore, while subducting oceanic crust gets destroyed and remelted, the continental crust persists.

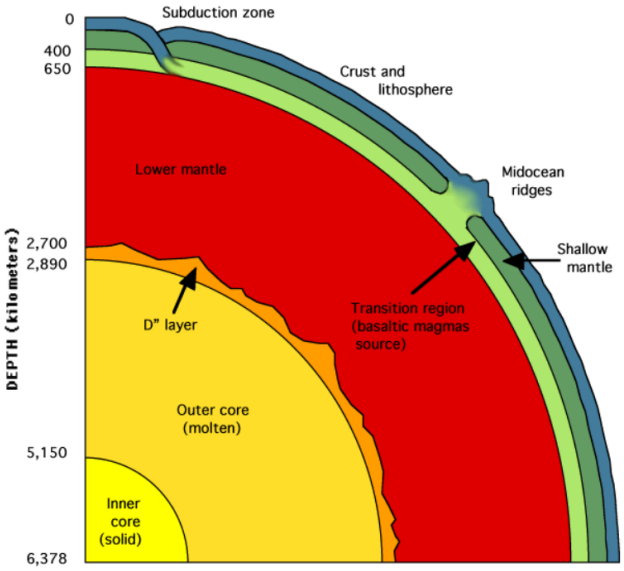

Figure 1.2.1: Structure of the Earth showing the different transitional layers according to the depth [37].

1.3 Bulk Silicate Earth (BSE) Models

The chemical composition of the Earth is subject of Geochemistry. The direct rock samples are however limited. The deepest bore-hole ever made is 12 km in Kola peninsula in Russia. Some volcanic and tectonic processes can bring samples of deeper origin to the surface but, they are often altered during transport. The composition of the crust is relatively well known with respect to the mantle.
The bulk composition of the silicate Earth i.e. the composition of the Primitive Mantle before the crust-mantle differentiation, is called the Bulk Silicate Earth (BSE). The mantle signal can be predicted by subtracting the known crustal signal from the prediction of the BSE models.

Geochemical models These models rely on the fact that the composition of carbonaceous (CI) chondrites matches the solar photospheric abundances in refractory lithophile, siderophile and volatile elements. The models assume that the ratios of Refractory Lithophile Elements (RLE) in the BSE are the same as in the CI chondrites and in the solar photosphere. The typical chondritic value of the bulk mass Th/U ratio is 3.9 and K/U ≈13,000. The absolute RLE abundances are inferred from the available crust and upper mantle rock samples. These models include [43], [8], [31], [48] and [12].

Cosmochemical models These models build the Earth from the enstatite chondrites [34] which show the closest isotopic similarity with mantle rocks and have sufficiently high iron content to explain the metallic core. The "collision erosion" model [46] is covered in this category as well. The models predict typical bulk U concentration of 10-12 ppb.

Geodynamical models These models are based on the energetics of the mantle convection. Considering the current surface heat flux, which depends on the radiogenic heat and the secular cooling, the parametrized convection models require higher contribution of radiogenic heat (and higher U and Th abundances) with respect to geo and cosmochemical models. The typical bulk U concentration is 35±4 ppb.

The surface heat flux is estimated based on the measurements of temperature gradients along several thousands of drill holes along the globe. The most recent evaluation of these data lead to the prediction of 47 ± 2 TW ([22], [33]). The geoneutrino measurement plays an important role in predicting the contribution of radiogenic heat to the total surface heat flux. The geochemical, cosmochemical and geodynamical models predict the radiogenic heat of 20 ± 4, 11 ± 2 and 33 ± 3 TW respectively.
There are different predictions regarding the distributions of HPE in the mantle:

i) Homogeneous mantle The case when the HPE are distributed homogeneously in the mantle. It corresponds to the maximal geoneutrino signal.

ii) Sunken Layer The case when the HPE are concentrated in a limited volume close to the core-mantle boundary corresponds to the minimal geoneutrino signal.

iii) Depleted Mante + Enriched Layer (DM + EL) This is a model of layered mantle, with the two reservoirs (DM and EL). Since in the process of differentiation, the HPE are rather concentrated in the liquid part, the residual mantle remains depleted in HPE. The total mass of HPE in the DM + EL corresponds to a chosen BSE model. There are estimates of the composition of the upper mantle (DM), from which the oceanic crust (composed of Mid-Ocean Ridge Basalts, MORB) has been differentiated ([11], [50], [54]). The measure MORB compositions indicate that their source must be depleted in HPE with respect to the rest of the mantle.

1.4 Geoneutrino Signal Around the World

The geoneutrino signal is expressed in Terrestrial Neutrino Units (TNU) which is defined as the number of interactions detected in one year on a target of 10^{32} protons(≈1 kton of liquid scintillator) and with 100% detection efficiency. The conversion of the signal in TNU to electron flavour flux (ϕ) requires knowledge of the geoneutrino energy spectrum and the interaction cross section which scales with the energy [23], and can be expressed as:

$$S(^{232}Th)[TNU] = 4.07 \cdot \phi(^{232}Th) \tag{1.4.1}$$

$$S(^{238}U)[TNU] = 12.8 \cdot \phi(^{238}U) \tag{1.4.2}$$

In order to estimate the crustal contribution of the geoneutrino signal at a particular place, it is necessary to know the signal that comes from the area with a radius of few hundreds of km around the detector called the Local Crust (LOC). The contribution from the Rest of the Crust (ROC) is estimated by taking the mean crustal compositions into account. The mantle signal is then calculated by subtracting these two contributions from the total signal.
So far, only two liquid scintillator detectors namely Borexino and KamLAND have provided geoneutrino measurements. Borexino is placed on a continental crust in cental Italy and KamLAND is situated in Japan, in an area with very complicated geological structure around the suduction zone. The characteristics and the predicted signals for both detectors are compared in Table 1.4.1.
KamLAND (Figure 1.4.1 (a)) was the first experiment to perform experimental investigations on geoneutrinos in 2005 [10] and an updated measurement was published in 2008 [4]. Consequently a geoneutrino observation at 99.97% C.L. was achieved in 2011 [21]. The Japanese nuclear reactors were temporarily switched off due to the Fukushima nuclear accident that occurred in March 2011. This helped in understanding the backgrounds better and led to further publication in 2013 [24] with $N_{geo} = 116^{+28}_{-27}$ events corresponding to 24% precision (Figure 1.4.1 (b)).

Criteria	Borexino	KamLAND
Depth	3600 m.w.e ($\phi_\mu = 1.2$ m^{-2}h^{-1})	3700 m.w.e ($\phi_\mu = 5.4$ m^{-2}h^{-1})
Scintillator mass	278 ton (PC + 1.5 g/l PPO)	1 kt (80% dodec. + 20% PC + 1.4 g/l PPO)
Inner detector	13 m sphere, 2218 8" PMTs	18 m sphere, 1325 17" + 554 20" PMTs
Outer detector	2.4 kt HP water + 208 8" PMTs	3.2 kt HP water + 225 20" PMTs
Energy resolution	5% at 1 MeV	6.4% at 1 MeV
Vertex resolution	11 cm at 1 MeV	12 cm at 1 MeV
Reactors mean distance	≈1170 km	≈180 km
Exp. LOC	9.7 ± 1.3 TNU	17.7 ± 1.4 TNU
Exp. ROC	$13.7^{+2.8}_{-2.3}$ TNU	$7.3^{+1.5}_{-1.2}$ TNU
Exp. Total Crust	$23.4^{+3.1}_{-2.6}$ TNU	$25.0^{+2.1}_{-1.8}$ TNU
Exp. CLM	$2.2^{+3.1}_{-1.3}$ TNU	$1.6^{+2.2}_{-1.0}$ TNU
Exp. Mantle	8.7 TNU	8.8 TNU
Exp. Total signal	$34.3^{+4.4}_{-2.9}$ TNU	$35.4^{+3.0}_{-2.1}$ TNU

Table 1.4.1: Comparison of the characteristics and expected signals for Borexino and KamLAND [42].

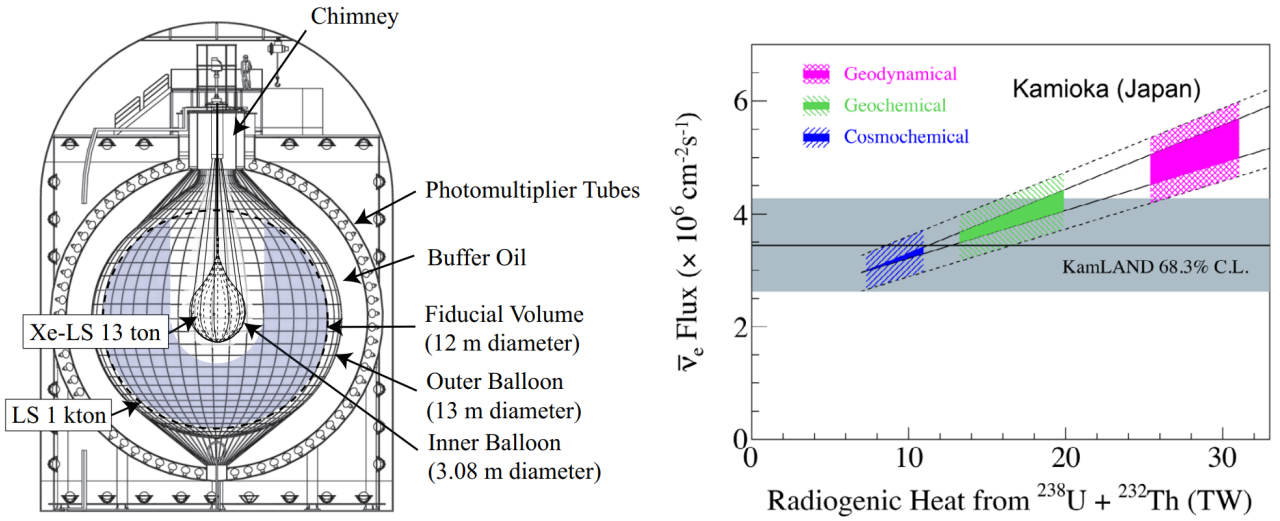

(a) (b)

Figure 1.4.1: (a) Schematic of the KamLAND detector. (b) Latest published geoneutrino results from KamLAND compared to BSE models. Figures taken from [24]

A detailed description of the Borexino detector, previously published results and the method of geoneutrino analysis is explained in detail in the next sections. The latest published Borexino results rejected the null-hypothesis of the mantle signal at 99.98% C.L. with a 5.9σ evidence of geoneutrinos.

2 The Borexino Detector

Borexino is a large volume liquid scintillator detector built with the primary purpose of solar neutrino detection i.e. measuring the neutrino fluxes that come from the different nuclear fusion processes in the sun. Besides solar physics, the unprecedented characteristics of its apparatus make Borexino very competitive in the detection of antineutrinos coming from the Earth and reactors. The physics goals also include detection of nearby supernova, measurement of the neutrino magnetic moment on solar neutrinos, and the search of very rare events like electron decay or the nucleon decay into invisible channels.

2.1 Experimental Setup

Borexino is designed to provide the largest possible fiducial volume of ultra-clean scintillator. The inner part of the detector is a Stainless Steel Sphere (SSS) that is both the container of the scintillator and the mechanical support of the PMTs. Two nylon vessels inside the SSS separate the scintillator volume into three shells of radii 4.25, 5.50 and 6.85 m. The inner nylon vessel (IV) contains the liquid scintillator solution, namely PC (pseudocumene, 1,2,4-trimethylbenzene $C_6H_4(COOCH_3)_2$) as a solvent and fluor PPO(2,5-diphenyloxazole, $C_{15}H_{11}NO$) as a solute at a concentration of 1.5g/l (0.17% by weight). The second and the third shell contain PC with a small amount (currently 2g/l) of DMP (diphenylphthalate, $C_6H_4(COOH_3)_2$). Nylon has approximately the same refractive index (1.53) as PC and thin nylon sheets are made to be very transparent. It is chemically compatible with both the scintillator and the buffer liquid. Nylon retains its material strength even when immersed in water. The liquid scintillator satisfies the following specific requirements which are essential for good energy resolution, precise spatial reconstruction, and good discrimination of β-like events and events due to α particles:

- High scintillation yield: 10^4 photons/MeV
- High light transparency: mean free path of typically 8 m
- Fast decay time: $\approx$3 ns

The PC+PPO has its emission spectrum peak at 360 nm thus matching well with the phototube peak efficiency. This fact, together with the low absorption of the scintillator and buffer liquid leads to an overall light collection of $\approx$ 500 photons/MeV of deposited energy corresponding to a resolution (1σ) of $\approx$ 5%. Since the PC/PPO solution is slightly lighter (about 0.4%) than the PC/DMP solution, the IV is anchored to the bottom (south pole of the SSS) with a set of nylon strings. The outer nylon vessel (OV) has a diameter of around 11 m and is built with the same material as the inner one. The OV is a barrier that prevents ^{222}Rn emanated from the external materials (steel, glass, PMT materials) to diffuse into the fiducial volume. The buffer liquid made of PPO/DMP is the last shielding against external background and is placed between the IV and the SSS. The use of PC as buffer is convenient because it matches both the density and the refractive index of the scintillator, thus reducing the buoyancy force for the nylon vessel and avoiding optic aberrations that would spoil the spatial resolution. The addition of DMP quenches the scintillation yield of the buffer liquid by a factor of 20. This is important to avoid the unacceptable trigger rate due to radioactivity of the PMTs.

The scintillation light is collected by 2212 PMTs that are uniformly attached to the inner surface of the SSS. All but 384 PMTs are equipped with light concentrators that are designed to reject

photons not coming from the active scintillator volume. The 384 PMTs without light concentrators are used to study this background due to radioactive decays in the buffer liquid or γ's from the PMTs. They also help in identifying muons that cross the buffer and not the IV. The SSS is supported by 20 steel legs and enclosed within a large tank filled with ultra pure water. The tank has a cylindrical base with a diameter of 18 m and a hemispherical top with a maximum height of 16.9 m. The Water Tank (WT) is a powerful shielding against external background (γ rays and neutrons from the rock) and is also used as a Cherenkov muon counter and muon tracker. The WT is equipped with 208 PMTs that collect the Cherenkov light emitted by muons in water. In order to maximize the light collection efficiency, the SSS and the interior of the WT surface are covered with a layer of Tyvek, a white paper like material made of polyethylene fibers.

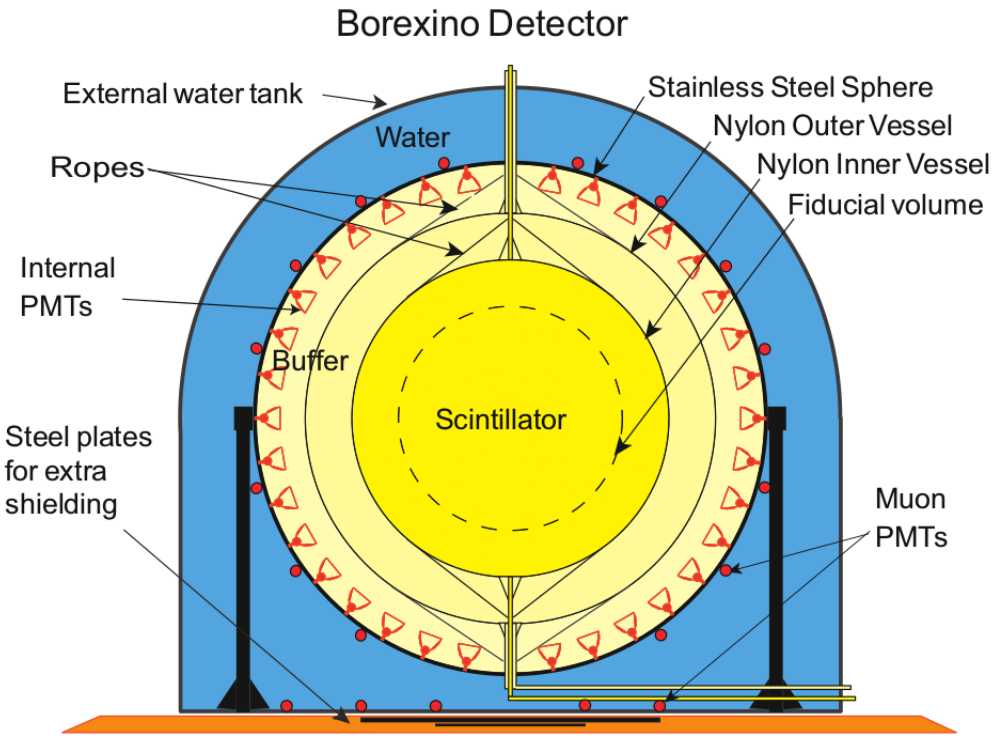

Figure 2.1.1: Schematic representation of the Borexino detector [14].

2.2 Data Aquisition (DAQ) and Event Structure

Borexino's electronics must handle 10^5 events per hour. The Inner Detector (ID) consists of 2212 PMTs and collects scintillation light inside the SSS. The Outer Detector (OD) is composed of 208 PMTs and detect the Cherenkov light produced by muons in water. These are two independent systems and a complex trigger system takes care of the integration of the ID and the OD. The ID electronics is organized in 14 identical racks, each of them handling 160 PMTs. Each rack supplies High Voltage (HV) to the PMTs, processes the signals through the front ends and eventually records the event information with dedicated digital boards called Laben Boards. Borexino PMTs are AC coupled, i.e. the signal and the HV travel along the same cable. After the decoupling stage, the negative signal has therefore a bipolar shape with a positive overshoot and a null area. The front end electronics of the OD is constituted by 14 Charge-to-time Converters (QTCs), each of which is made of 16 channels. The output of the QTC is connected to a commercial double-edge Time to Digital Converter, which measures the time of the rising and falling edges of the signal. The first rising edge yields the time of the PMT pulse, while the time distance to the second falling edge yields the charge.
After data acquisition and storage in memory, the trigger establishes whether the signal is worthy

to be recorded by establishing how many channels are hit in a given time window of 90 ns. This is set at 20 PMTs. The trigger time window is decided according to the photon transit time of about 50 ns throughout the SSS. The Borexino triggering system has to identify scintillation events that are detected by the quasi simultaneous occurrence of several PMT hits in the ID. The Borexino Trigger Board (BTB) handles several other additional triggers such as random triggers, electronic pulse triggers, and timing laser triggers which are fired for monitoring purposes apart from the main trigger types trigger type 1 (events that triggers the ID) and trigger type 2 (events that exclusively triggers the OD). The Muon Trigger Board (MTB) is another custom made trigger to generate the OD's trigger signals and evaluate appropriately the coincidence with BTB. Clock electronics are implemented through the Quartz Oscillator of the ClocK Generator board. Absolute time tagging is kept with a GPS receiver connected with the satellites through a precision fiber optic link upgraded to about 100 ns precision during the Cern to Gran Sasso (CNGS) campaign [51]. There are in total six types of trigger (tt), listed in the order of priority:

- tt1 - neutrino
- tt2 - muon MTB
- tt128 - muonTotC
- tt8 - laser394
- tt32 - calibration
- tt64 - random

During a physical event, the raw hits are the actual hits recorded during the event and the decoded hits are all the valid raw hits according to their time and space correlation. Thus, the event structure of a physical event is the depiction of these decoded hits in the DAQ time window. The event structure of different types of events in the ID and OD is shown in Figures 2.2.2 and 2.2.1.
The triggers 8, 32, and 64 are service triggers that are sent periodically to the BTB by a Nuclear Instrumentation Module (NIM) dual timer. The laser trigger 16 is enabled and sent periodically. The trigger type 128 is opened for 1.6 ms right after MTB is triggered for tt1 events to "catch" all the fast neutrons that might be formed due to the spallation of the muons (Figure 2.2.3). The BTB inputs in the initial state is at 0 and the bit 2^2 is set once the OD PMTs are triggered. Thus, events that happen inside the scintillator ("neutrino" or point-like events) have BTB inputs 0 and trigger type 1, muons that pass only through OD have BTB inputs 4 and trigger type 2 (external muons) and muons that pass through both the ID and OD have BTB inputs 4 and trigger type 1 (internal muons). The different kinds of muons in Borexino are explained in Section 4.2.

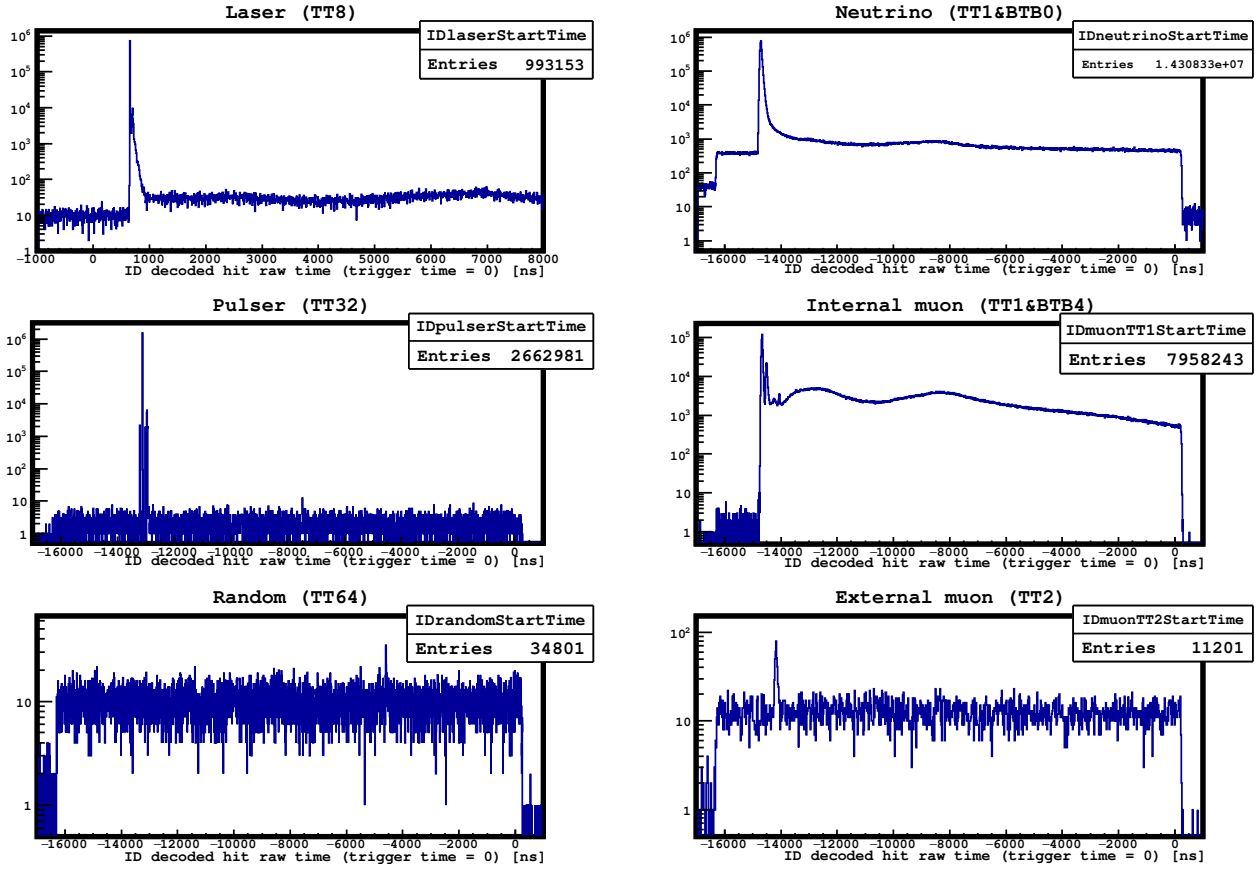

Figure 2.2.1: Event structure in the Inner Detector (ID) for different trigger types for a typical 6h run.

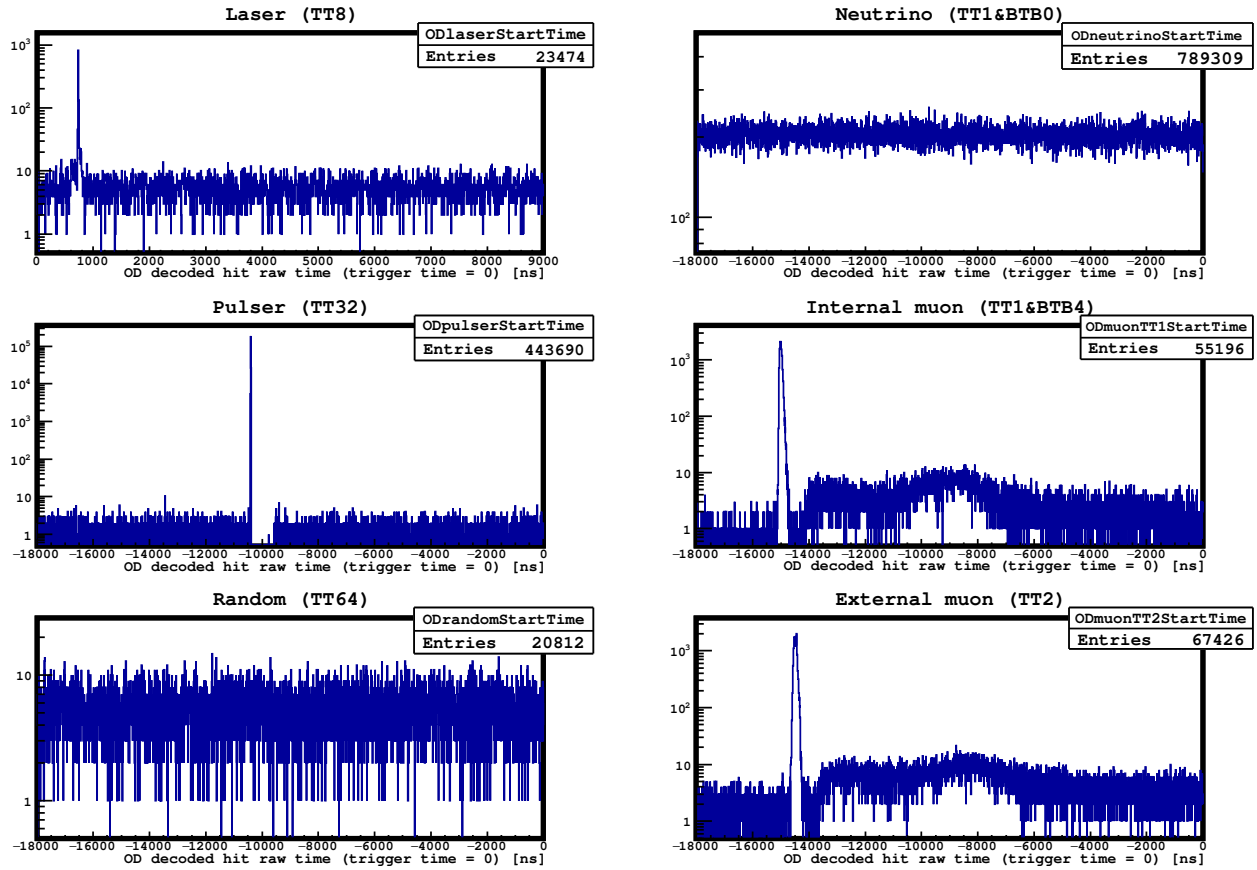

Figure 2.2.2: Event structure in the Outer Detector (OD) for different trigger types for a typical 6h run.

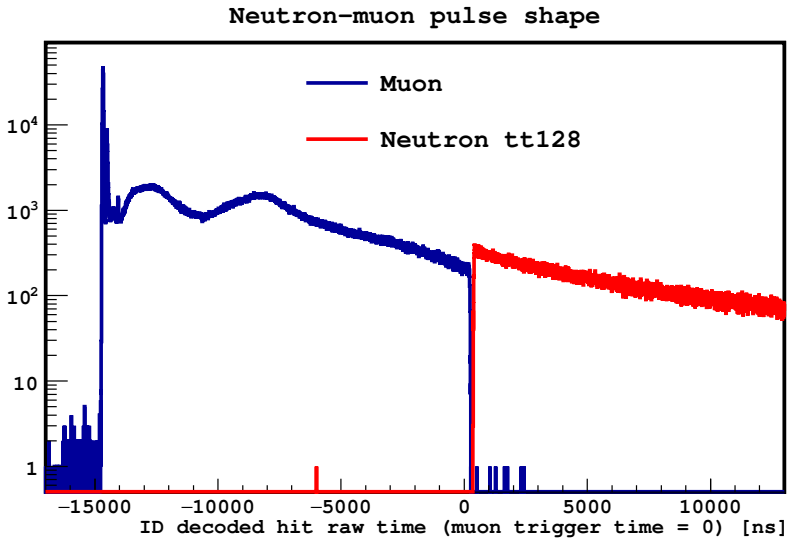

Figure 2.2.3: Event structure of BTB 4 muon (blue) and the first 13 μs of the 1.6 ms tt128 gate (red) opened after them for a typical 6h run.

2.3 Energy and Position Reconstruction

The energy deposited by a particle interacting in the Borexino scintillator is proportional to the number of photons collected by the PMTs. An electron with kinetic energy of 1 MeV produces approximately 500 photoelectrons in the Borexino detector. The three energy estimators used are: N_{pe}-the sum of charge of all hits collected in the DAQ gate, N_P - the number of triggered PMTs and N_h- number of hits which is similar to the number of PMTs but, this variable allows for multiple signals from the same PMT. The light production in an organic scintillator is affected by non-linear effects such as light quenching. Furthermore, due to the large size of the detector, light collection is significantly perturbed by photon propagation effects like absorption, re-emission, and scattering processes. In addition, geometrical shadowing effects, effects of electronics and an asymmetric distribution of operational PMTs have to be taken into account. The non-uniform energy response due to these effects requires MonteCarlo (MC) simulations capable of reproducing the details of the emission and the propagation of photons within the scintillator.

The reconstruction of event position $\vec{r_0}$ in Borexino is based on the time distribution of the collected hits: the algorithm considers for each photon its arrival time t_i and the position $\vec{r_i}$ of the PMT which detected it, subtracts its time of flight T^i_{flight}, and compares the photon time distribution with the reference probability density function (pdf) of the Borexino scintillator. The event position is calculated by maximizing the likelihood $L_E(\vec{r_0}, t_0 \mid (\vec{r_i}, t_i))$.

The internal and external calibrations [13] held at the beginning of data taking aided in studying the energy response of the detector. The internal calibration was done using many mono energetic γ sources, ^{222}Rn-^{14}C as an α/β source, ^{241}Am-^{9}Be as a neutron source, placed in different positions. This helped in studying the energy scale in different parts of the detector, testing the position reconstruction algorithm, validating the MC simulations, and studying the detector trigger efficiency. Laser sources placed at different positions helped in studying the PMT synchronization and equalization. The external calibration was done using ^{228}Th whose daughter nuclide ^{208}Tl is a strong gamma source. This helped in studying the exact determination of the IV shape, the external γ background near the IV, and the asymmetries in the energy response near the IV.

Two kinds of energy and position variables are used for data analysis in Borexino: the primary Echidna variables and the secondary Mach4 variables. Both these variables have independent

reconstruction algorithms starting from the Echidna decoded hits. The primary energy variable used for the geoneutrino analysis is the Echidna charge variable measured in p.e. The current version is the cycle 18 version of Echidna and all the variables used in this work corresponds to this version.

2.4 Flash Analog to Digital Converter (FADC) System

The Flash Analog to Digital Converter (FADC) system is an auxiliary hardware architecture built from 34 Fast Wave Form Digitizing (FWFD or FADC) 400 MHz, 8 bit VME boards (CAEN V896), 3 input channels each. 98 out of 102 channels receive the analog sums of 16 or 24 PMTs (two FEBs). These sum signals are provided by 13 analog adders (one per rack). Four NIM FAN OUT blocks distribute 50 MHz synchronization frequency and trigger signal to each board. Each channel of the 13-input channel fraction discriminator keeps its unique threshold and 4 discriminator channels are required to fire in ≈100 ns time gate or total analog sum of all PMTs should be above threshold.
An FADC event (Figure 2.4.1) consists of 512 digitizations 2.5 ns each. This gives a 1280 ns time gate called the FADC page.

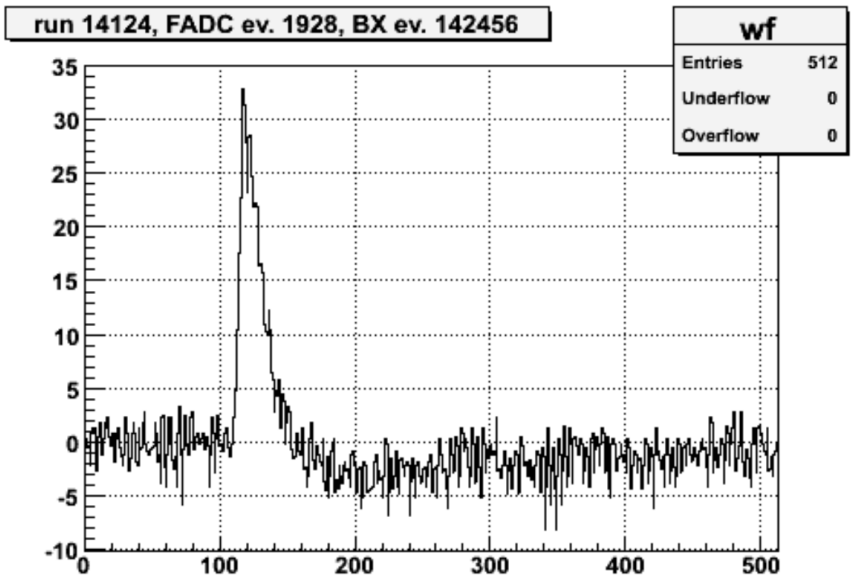

Figure 2.4.1: Typical FADC event. Window length is 1280 ns (512 digitizations of 2.5 ns each) [35].

The different trigger types used in the FADC system are as follows:

- tt1- Normal ("neutrino") event
- tt3- 100 Hz pulser at the beginning of each run
- tt5- Laser394
- tt8, tt40- Muon (or light leak) in the OD
- tt9, tt33, tt41- Muon through both ID and OD
- tt11- 0.1 Hz pulser during the run
- tt32- OD-sum discriminator ("CNGS" trigger)

The energy variables used in FADC are (1) analog sum i.e. the analog sum signal over all 13 racks, (2) attenuated (factor 3.2) analog sum, (3) digital sum i.e. digital sum over all 98 FADC channels, and (4) corrected digital sum which employs waveform correction algorithms. An FADC event always has one or more clusters unlike the normal DAQ where zero cluster events are also present. A cluster is defined as the aggregation of decoded hits in the DAQ window. In addition,

the FADC analysis software also has tools to differentiate muons and noise events using their pulse shape.

2.5 Monte Carlo Simulations

Particles depositing energy in the IV or in the buffer region produce scintillation and Cherenkov photons which propagate inside the detector and possibly reach the PMTs yielding a detectable signal. The agreement between measured observables (energy estimators and PMT pulse times) and the physical quantities (deposited energy, position, type of particles generating the signal) depends on the knowledge and understanding of all the physical processes governing the particle energy loss in the various materials, the scintillator light production, propagation, and detection. The MC simulation chain consists of a set of numerical codes that:

1. provide a wide range of event generators, from solar neutrino interactions, to radioactive decays, geoneutrinos, and calibration source events.

2. simulate the energy loss of each specific particle in every material present in the detector, either active (the scintillator, buffer liquid, and water in the muon detector) or passive.

3. generate a number of scintillation or Cherenkov photons considering the particle energy loss in the media and the properties of the scintillator and/or the buffer.

4. track each single optical photon including its interactions with the scintillator and with the materials, until a PMT is reached or the photon is absorbed.

5. generate the PMT response for photons absorbed at the PMT cathode, considering the effective quantum efficiency of each individual PMT.

6. generate the PMT pulse signal taking into account the specific design of the front end of the digital electronics chain of Borexino.

7. simulate the trigger generation and save the final output for triggering events.

8. produce a raw data file with the same structure as the one produced by the Borexino data aquisition system.

The MC code is structured in two separate programs namely, event generation and light tracking, simulations of electronic response. Finally event reconstruction that converts the binary data generated by the DAQ into physical observables.
The event generation is implemented within the Geant4 package, an object oriented C++ toolkit for the simulation of passage of particles through matter and uses its standard libraries. As mentioned in the end of Section 2.3, MC validation is performed using the data from calibration campaigns (Figure 2.5.1).

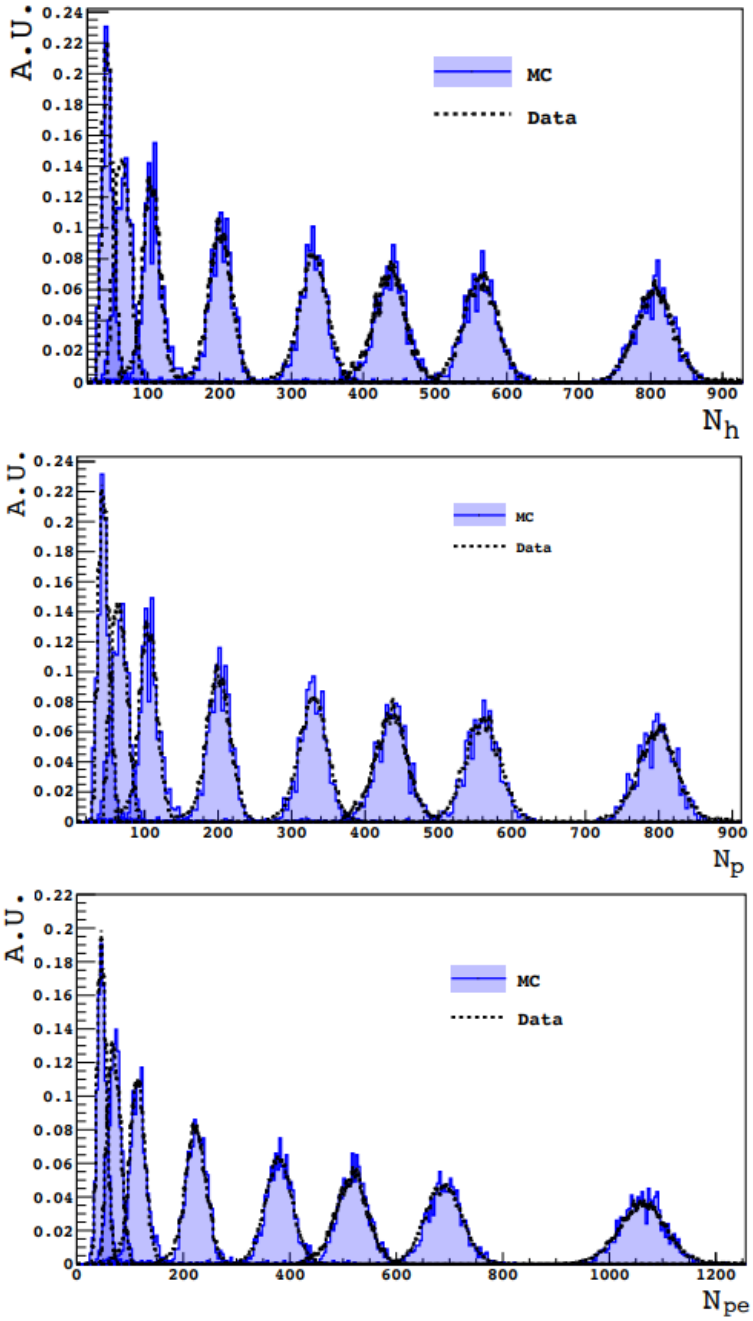

Figure 2.5.1: Agreement between MC and data for the three different energy variables nhits(N_H), npmts (N_P), and n.p.e.(N_{pe}) for the different γ sources and 2.22 MeV γ from ^{241}Am-^{9}Be source [5].

3 Previous Geoneutrino Results with Borexino

The depth of the Borexino detector (3800 m w.e.), huge volume (278 ton), the large distance from reactor antineutrinos (≈1200 km away from reactors) and the extreme radiopurity of the scintillator has made it possible for Borexino to measure geoneutrinos. The Borexino collaboration has published the first observation of geoneutrinos in 2010 [19] and the first measurement in 2013 [17]. The latest geoneutrino measurement with the Borexino detector published in 2015 [7] included a 5.9σ evidence of geoneutrino and the rejection of the null-hypothesis of the mantle signal at a 98% C.L. The analysis was done for a total exposure of $(907 \pm 44$ ton$) \cdot$ yr and a livetime of 1841.9 days. This section aims to summarize the selection cuts, background study, and the final results published in 2015.

3.1 Standard Selection Cuts

Muon vetoes:
The live time of the measurement is dependent on the dead time cut that is applied once a muon passes through the detector. It is crucial to reject IBD like signals coming from the muon daughters which is explained in detail in Section 4.2. In the 2015 analysis, a 2 ms dead time was applied to the external muons, i.e. the muons passing only through the OD to reject the fast neutrons that might enter the scintillator volume. In order to eliminate the hadronic background coming from the internal muons, i.e. muons passing through the scintillator, a 2 s veto was applied, which is 8 lifetimes of ^{9}Li and 12 lifetimes of ^{8}He. This resulted in a 10.41% live time loss.

Energy cuts:
In Borexino, the charge is measured in terms of photoelectrons (p.e.). The light yield of the detector is measured to be 500 p.e./MeV with an energy resolution of approximately $5\%/\sqrt{E}$. In the previous analysis, the minimum charge of the prompt event (Q_{min}(prompt)) was required to be above 408 p.e., corresponds to 1.022 MeV in order to also detect the minimum energy of prompt of 1 MeV after considering the energy resolution. The delayed event was looked for between 860 - 1300 p.e. which corresponds to the energy of the gammas emitted from neutron capture on the protons in the scintillator (2.2 MeV) after including the low energy tail at larger radii. The reasons for the energy cuts are explained in detail in Section 6.4

Time and space correlation:
The time difference between prompt and delayed was required to be between 20-1280 μs, i.e. five times the neutron capture time. In order to decrease the amount of random coincidences in the sample, the distance between the prompt and the delayed (dR) events was required to be 1 meter. The role of electronics in choosing the time window and role of the signal to background (S/B) ratios for different dR cuts are explained in detail in Section 6.2

α/β discrimination - Gatti cut:
The gatti parameter is a pulse shape discrimination technique to distinguish α and β decays. This is explained in detail in Section 6.3. In the 2015 analysis, a cut of < 0.015 was applied on the delayed event's gatti parameter in order to reject α and γ decays that happened due to Rn events during the water extraction periods.

Dynamical Fiducial Volume (DFV) cut:
In addition, a fiducial volume cut of 30 cm was applied to eliminate events that enter the scintillator volume from the buffer and the surrounding detector parts. Thus only prompt events that are farther than 30 cm from the time varying inner vessel (IV) were used for the analysis. This reduced the overall exposure by around 18%. Detailed study of the DFV cut is reported in Section 6.5.

Multiplicity cut:
A multiplicity cut was applied to eliminate neutron like events ($>$ 408 p.e.) 2 ms before prompt, 2 ms after prompt, and between prompt and delayed events. This was applied in order to tag neutrons from the muons that were missed by the muon identification flags, explained in Section 4.2.

3.2 Summary of Backgrounds

The most relevant backgrounds for geoneutrino analysis apart from the major reactor antineutrino background are the following:

^{9}Li-^{8}He background:
The main muon daughters namely the ^{9}Li and ^{8}He isotopes can produce IBD-like decays. Such coincidences are looked for within 2 s from the passage of muon through the scintillator (dead time from internal muons). The decay time of the hadronic components is then obtained and the estimated background that might remain after 2 s is calculated. This is explained in detail in Section 4.2.1. The ^{9}Li-^{8}He background estimated in 2015 for the standard selection cuts was $0.194 \pm 0.015\ (\text{stat})^{+0.124}_{-0.088}$ (syst). The distribution of the time difference between the muon and the prompt event (dt(prompt-muon)) for the candidates obtained in 2015 is shown in Figure 3.2.1

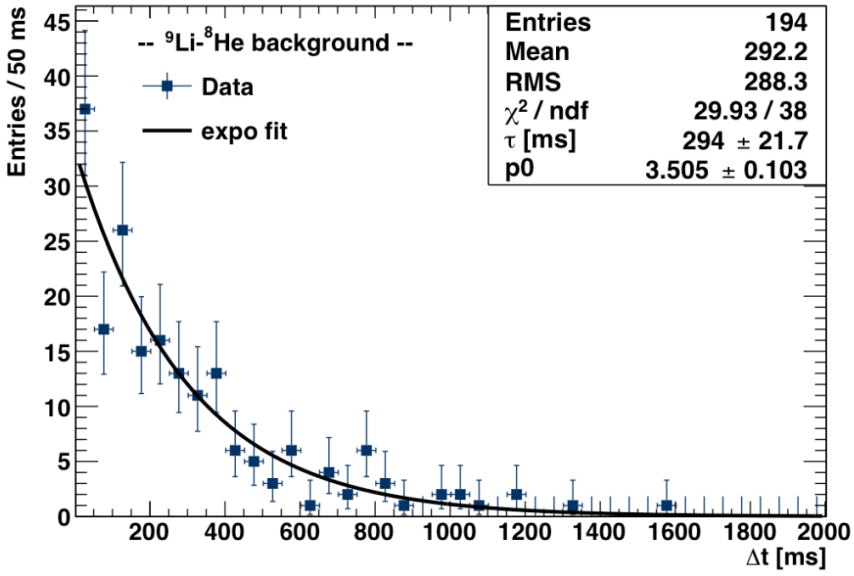

Figure 3.2.1: Distribution of time difference Δt between the prompt event and muon for the ^{9}Li-^{8}He candidates without any DFV cut to estimate decay time in the 2015 analysis. [27]

Random coincidences:
In order to calculate the amount of random coincidences in the geoneutrino sample, IBD signals away from the geoneutrino time window of [20, 1280] μs were searched for. A constant accidental background in the time window [2, 20] s and a time correlated background in the time window

[2 ms, 2 s] were studied. The number of events found were scaled to the [20,1280] μs geoneutrino window. These backgrounds are explained in detail in Section 4.3. The accidental and time correlated background estimated during the 2015 analysis were 0.221 ± 0.004 and 0.035 ± 0.028 (stat)$^{+0.005}_{-0.003}$ (syst), respectively. The random coincidental background estimated in 2015 is shown in Figure 3.2.2

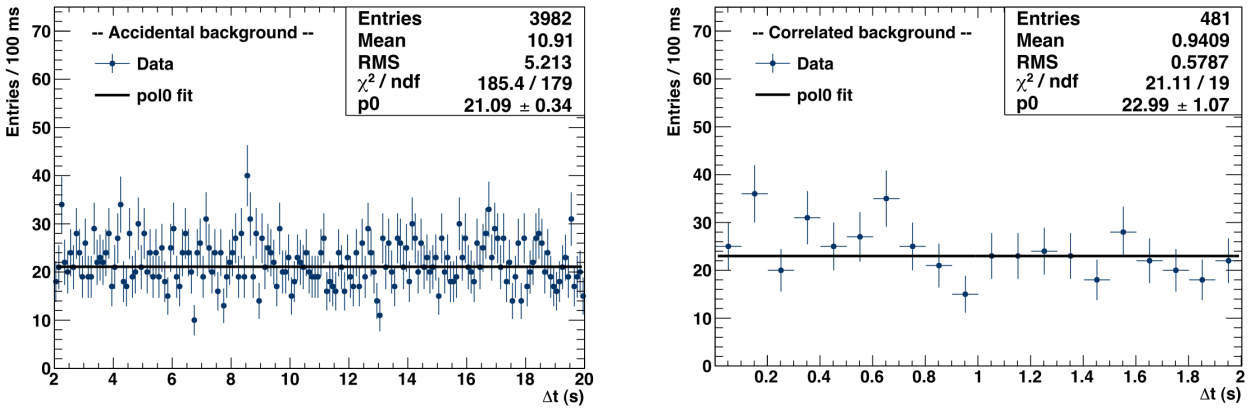

(a) Accidental background

(b) Time correlated background

Figure 3.2.2: Distribution of time difference Δt between prompt and delayed events for accidental and time correlated backgrounds estimated for the 2015 analysis [27].

(α, n) background:
The alpha particles coming from internal radioactive decays can enter the scintillator volume and react with the ^{13}C isotope in the scintillator. The IBD like signals produced due to such reactions are explained in detail in Section 4.4. Based on the probability of this interaction and the mean activity of ^{210}Po in the buffer, the (α, n) background for the 2015 analysis was calculated as 0.165 ± 0.01.

Apart from these major backgrounds, the other backgrounds such as fast neutrons from rock and water tank (Section 4.2.4), (γ, n) reactions (Section 4.5), untagged muons (Section 4.2.3), ^{214}Bi-^{214}Po coincidences (Section 4.6), and fission due to the impurities in PMTs are listed in Table 3.2.1.

Background	Value
^{9}Li-^{8}He	$0.194^{+0.125}_{-0.089}$
Accidental coincidences	0.221 ± 0.004
Time correlated background	$0.035^{+0.029}_{-0.028}$
(α, n) in scintillator	0.165 ± 0.010
(α, n) in buffer	<0.51
Fast n's (μ in WT)	<0.01
Fast n's (μ in rock)	<0.43
Untagged muons	0.12 ± 0.01
Fission in PMTs	0.032 ± 0.003
^{214}Bi-^{214}Po	0.009 ± 0.013
Total	$0.78^{+0.13}_{-0.10}$

Table 3.2.1: Estimated number of background events in [7]. Upper limits are given with 90% C.L.

3.3 Final Results

A maximum likelihood fit was performed using two methods. In the first method, the ^{232}Th to ^{238}U ratio of the energy of the prompt event of the selected 77 candidates was fixed to the chondritic value and the fit was performed to obtain the observed geoneutrino and reactor antineutrino signals. In the second method, the amount of geoneutrinos coming from the ^{238}U and ^{232}Th was left free. The fits were performed using fixed values ($\pm$ 1σ) for the non-antineutrino backgrounds. The spectra used for p.d.f.s construction was taken from MC for geoneutrinos, reactor antineutrinos, ^{9}Li-^{8}He, and (α,n) backgrounds and from data for the accidental background. The best fit yielded $S_{geo} = 23.7^{+6.5}_{-5.7}$(stat) $^{+0.9}_{-0.6}$(syst) [$43.5^{+11.8}_{-10.4}$(stat) $^{+2.7}_{-2.4}$(syst) TNU] and $S_{rea} = 52.7^{+8.5}_{-7.7}$(stat) $^{+0.7}_{-0.9}$(syst) [$96.6^{+15.6}_{-14.2}$(stat) $^{+4.9}_{-5.0}$(syst) TNU] (Fig 3.3.1 (a)). Borexino alone observed geoneutrinos with a 5.9σ significance. The measured signal corresponds to antineutrino fluxes at the detector from decays in the U and Th chains ϕ(U) = (2.7$\pm$0.7) x 10^6 cm^{-2}s^{-1} and ϕ(Th) = (2.3$\pm$0.6) x 10^6 cm^{-2}s^{-1}, respectively (Fig 3.3.1 (b)).

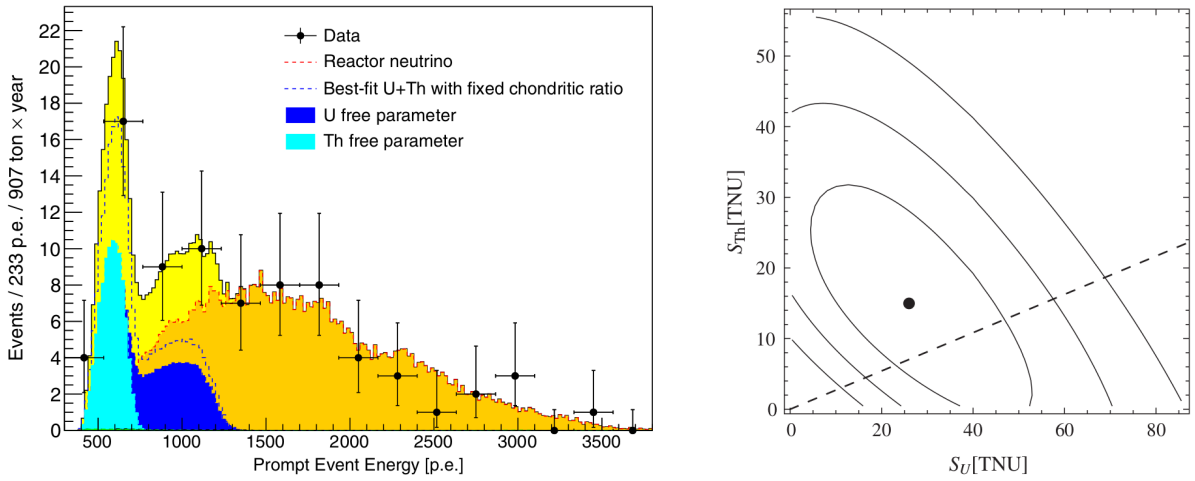

(a) (b)

Figure 3.3.1: Final results published in the 2015 geoneutrino analysis with Borexino [7]. (a) shows the fit results obtained for using the prompt light yield spectra of the signal and background components and (b) shows the best-fit contours for 1σ, 2σ and 3σ by keeping U and Th as distinct and free parameters.

Based on the chondritic ratio for U/Th and assuming the Potassium-to-Uranium mass ratio of m(K)/m(U) = 10^4, the total measured terrestrial radiogenic power was P(U+Th+K) = 33^{+28}_{-20} TW, to be compared with the global terrestrial power output P_{tot} = 47 $\pm$ 2 TW. The mantle geoneutrino signal was calculated as S_{geo}(Mantle) = S_{geo} - S_{geo}(LOC + ROC) using the experimental likelihood profile of S_{geo} and a Gaussian approximation for the crust contribution. The final values reported in the 2015 analyis were S_{geo}(LOC) = (9.7 $\pm$ 1.3) TNU, S_{geo}(LOC+ROC) = (23.4 $\pm$ 2.8) TNU and S_{geo}(Mantle) = $0.9^{+15.1}_{-10.3}$ TNU. The null hypothesis of the mantle signal was rejected at 98% C.L.
The best value of Borexino's geoneutrino signal and radiogenic heat with the errors were compared to the three BSE models as shown in Figure 3.3.2.

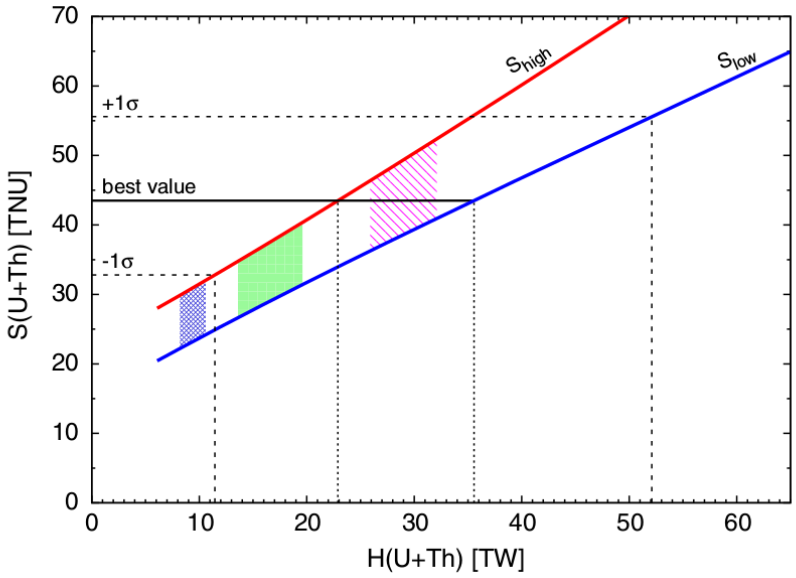

Figure 3.3.2: Borexino values with $\pm 1\sigma$ compared to the three different Bulk Silicate Earth (BSE) Models namely the cosmochemical (blue), geochemical (green), and geodynamical (magenta) models [7].

4 Backgrounds

4.1 Reactor Antineutrino Signal at LNGS

The most important antineutrino background for the geoneutrino analysis is the reactor antineutrino background coming from the 194 European nuclear reactors. The reactor antineutrinos with energies above the IBD threshold are produced dominantly by the beta decay of fission products from the four isotopes i = ^{235}U, ^{239}Pu, ^{238}U, and ^{241}Pu (Figure 4.1.1 (a)). The contribution from other isotopes and fission fragments are less than 0.1%. The antineutrino flux per fission produced by each of these isotopes is parameterized by [32] and given as,

$$\phi_i(E_\nu) = exp(\sum_{k=0}^{5}(a_{ki})E_\nu^k) \tag{4.1.1}$$

The reactor antineutrino flux at LNGS can be calculated using 4.1.2 after summing over all the months $|m|$ and all the European reactors $|r|$ for the four isotopes ($|i| = 4$):

$$\Phi(E_\nu) = \sum_r \sum_m \frac{T_m}{4\pi L_r^2} P_{rm} \sum_i \frac{f_{ri}}{E_i} \phi_i(E_\nu) P_{ee}(E_\nu, L_r), \tag{4.1.2}$$

where ϕ_i is the antineutrino flux per fission, L_r is the distance between LNGS and the reactor, T_m is the measuring time, P_{ee} is the survival probability of the antinutrinos, P_{rm} is the thermal power calculated month-by-month for each reactor, E_i is the energy release per fission, and $f_i = \frac{N_i^{fiss} E_i}{P}$ is the power fraction given (N_i^{fiss} is the number of fission per second).
The so-called reactor anomaly (Figure 4.1.1 (b)), where a slight bump at 5 MeV in the reactor antineutrino spectra, has been observed in a few experiments is also taken into account in the systematic studies of this analysis discussed in Section 7.4. This adds an additional rate of 1.7% to the total IBD cross section. The prediction of the reactor antineutrino flux using the above method for the period Dec 2007 - May 2018 is given as (84.8 ± 4.2) TNU and (79.9 ± 4) TNU without and with the bump, respectively [49].

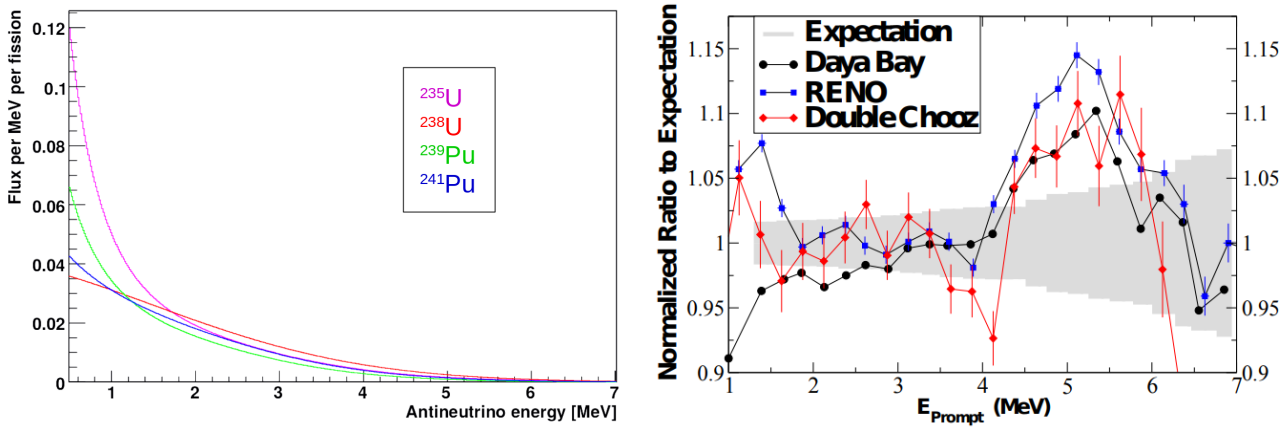

(a) (b)

Figure 4.1.1: (a) Antineutrino fluxes per fission [38]. (b) Reactor energy spectra compared to expectations from [32] and normalised to the same number of events for different experiments showing the bump at 5 MeV [29].

4.2 Cosmogenic Background: Muon and Muon Daughters

One of the most important non-antineutrino backgrounds for geoneutrino detection in Borexino is the cosmogenic background due the residual muon flux. It is necessary to tag these muons efficiently and eliminate them along with the muon daughters as they can imitate the IBD signals.

Muons that only trigger the Outer Detector (OD) are called external muons and muons which pass through the scintillator and buffer are called as internal muons. Most of the internal muons (99.98%) trigger the OD while the remaining muons are tagged by the Muon Cluster Reconstruction (MCR) flag, the Inner Detector Flag (IDF) and other special flags. The events which are detected by the MTB have BTB inputs = 4 and the events which are not detected by the Muon Trigger Board (MTB) have BTB inputs = 0 as explained in Section 2.2. Apart from this, muon identification is also performed by an independent FADC system explained in Section 2.4.

Muon Trigger Board (MTB):
MTB muons trigger the OD. Muons are identified when there is a considerable increase in the number of hits in a time window comparable to the muon transit time. The threshold is set to 6 PMTs firing in a time span of 150 ns. Once an MTB muon pases the detector, a 1.6 ms gate is opened (tt128) so that the fast neutrons followed by muon spallation does not go undetected.

Muon Cluster Reconstruction (MCR):
The MCR flag is a software reconstruction algorithm based on the acquired hits in the OD PMTs and similar to the MTB flag. The main difference is that, MCR takes into account two subsets of PMTs: PMTs on the SSS + PMTs mounted on the floor. The condition is met if 4 PMTs of either subset are fired within 150 ns.

Inner Detector Flag (IDF):
The Inner Detector Flag identifies muons based on the peak time and the mean time of the cluster of hits from ID. The mean time is the mean value of the decoded hit times that belong to the cluster and the peak time is the time at which most of the decoded hits are deposited. It uses the fact that the peak time is a better discriminator for muons and point-like events in the lower energy ranges and mean time is a better discriminator in the higher energy ranges. This is shown in Figure 4.2.1. The visible energy is measured using the number of hits (nhits).

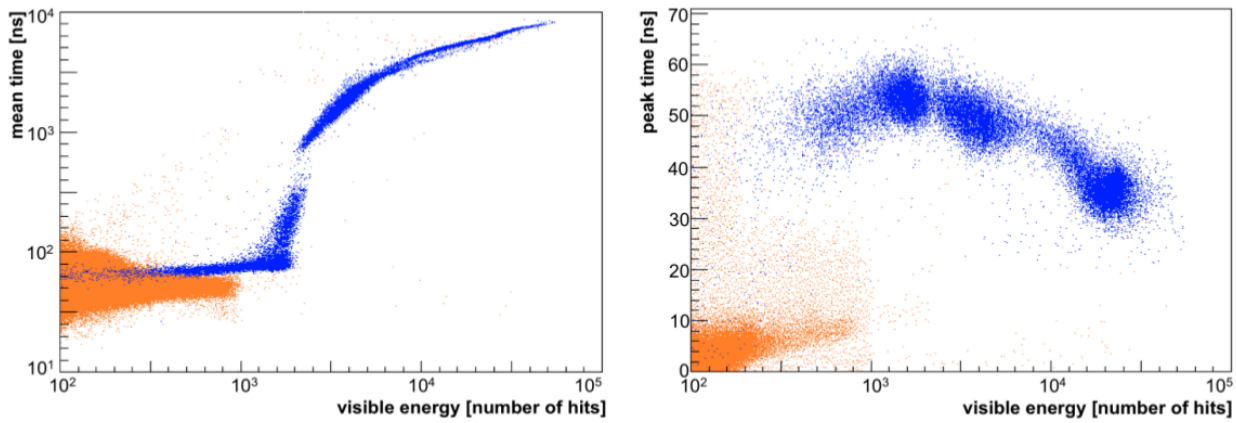

Figure 4.2.1: Plots showing the mean time and peak time vs visible energy for point-like (orange) and muon (blue) events (mean time and nhits used are for the short Echidna cycle 11 cluster variables). [15]

In the higher energy ranges a gatti cut (α/β discrimination parameter, explained in Section 6.3)

is applied to reject electronic noise and retriggering of muons. A gatti cut is applied to the lower energy ranges as well to avoid scintillation pulses coming from the buffer. Summary of parameters used for IDF is given in Table 4.2.1

Visible Energy (nhits)	**Mean Time (ns)**	**Peak Time (ns)**	**Gatti**
80-900	x	>40	> 0.2 (if z > 4 m)
900-2100	x	>30	x
> 2100	>100	x	< 0.55

Table 4.2.1: Summary of Inner Detector Flag (IDF) muon tagging conditions [15].

Special Muons:
Muons detected by the above three (MTB, MCR, IDF) main muon detector flags are tagged as strict muons. Apart from these strict flags, there are also five kinds of special flags which tag the remaining small fraction of muons, however tag also some noise events.

Special d1- This flag was introduced to tag muons when the electronics is too saturated to tag muons i.e. sufficiently high amount of raw hits (NR) but very few decoded hits (ND) (see Section 2.2). Therefore, special d1 tags events when only 5% of raw hits are decoded if the events have more than 200 raw hits.(ND/NR $<$ 0.05 if NR $>$ 200)

Special d2- The special d2 flag tags muons that were interrupted by service triggers. When the OD trigger with BTB inputs = 4 is followed by a service interrupt, the BTB inputs change from 4 to 4U. If such events have more than 100 decoded hits, they are tagged as special d2 muons.

Special d3- Events with cluster start time out of the DAQ gate are tagged as special d3 muons.

Special d4- In order to tag all the muons missed by the IDF, all events with a cluster mean time greater than 200 ns are tagged as special d4 muons.

Special d5- The extremely few number of tt1 MTB or MCR muons with zero clusters in the ID are tagged as special d5 muons.

Flash Analog to Digital Converter (FADC) Identification of muons:
Borexino also has an independent FADC system to identify muons. The FADC pulse shape analysis of muons can be used to identify muons that are missed by the main DAQ. Unlike the Borexino DAQ window of 16 μs, FADC has a time window of 1.28 μs, i.e. number of FADC clusters $\geq$ number of borexino clusters for a single event. This system was helpful in the previous analysis to check if there were any untagged muons in the geoneutrino sample. It helped in eliminating one geoneutrino candidate since it was a muon which was exclusively detected by the FADC system. But, it is also important to apply dead times to these exclusive FADC muons and evaluate the resulting exposure. The method of identifying these muons and applying dead times after them is explained in detail in Section 6.1. Figure 4.2.2 shows the comparison of pulse shapes between the same muon detected by the Borexino trigger board and the FADC system.

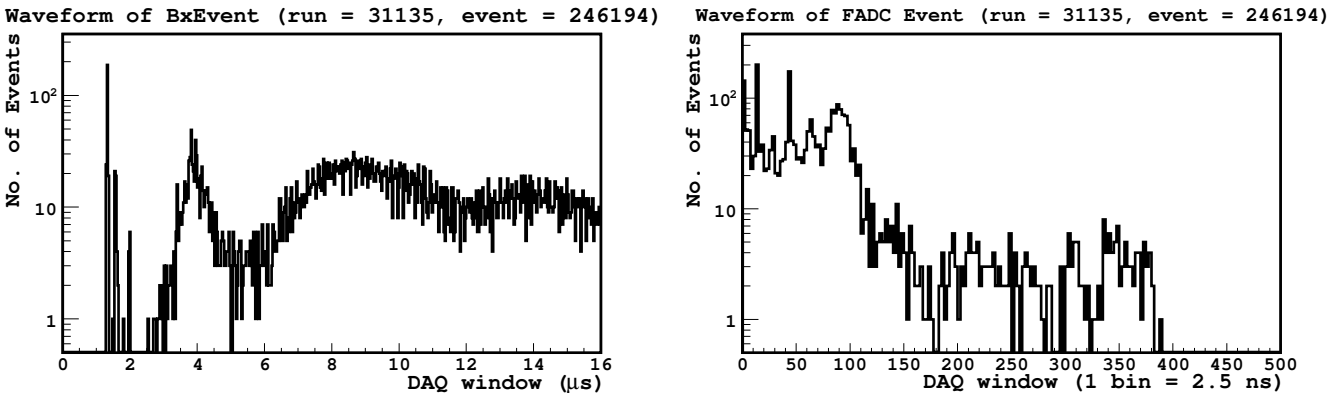

(a) (b)

Figure 4.2.2: Decoded hits distributions of a typical muon event: (a) Distribution in the 16 μs DAQ time window of the the Borexino Trigger System. (b) Distribution in the 1280 ns DAQ window (512 digitizations) of the FADC System.

Annual Modulation of Muons: The study of the stability of the three main muon detector flags namely MTB, MCR, and IDF year by year confirmed the indication of annual modulation in muons according to the equation 4.2.1, as published in [52].

$$I_\mu(t) = I_\mu^0 + \delta I_\mu cos(\frac{2\pi}{T}(t - t_0)) + \delta I_\mu^{long} cos(\frac{2\pi}{T_{long}}(t - t_0^{long})). \quad (4.2.1)$$

Here, $I_\mu^0 = (4329.1 \pm 1.3)$ d^{-1} $= (3.432 \pm 0.001)\cdot 10^{-4}$ m^{-2}s-1, $\delta I_\mu = (58.9 \pm 1.9)$ d-1 $= (1.36 \pm 0.04)\%$, $T = (366.3\ pm\ 0.6)$ d, $t_0 = (174.8 \pm 3.8)$ d, $T^{long} = (3010 \pm 299)$ d $= (8.25 \pm 0.82)$ yr, $t_0^{long} = (1993 \pm 271)$ d and $\delta I_\mu^{long} = (14.7 \pm 1.8)$ d^{-1}. This modulation of muons was observed in all three detector flags when corrected for their mutual inefficiencies (Section 4.2.3), as shown in Figure 4.2.3 (a). The equation (4.2.1) was fit to MCR muons and is reported in [52] after statistically subtracting the seasonal modulation. (Figure 4.2.3 (b))

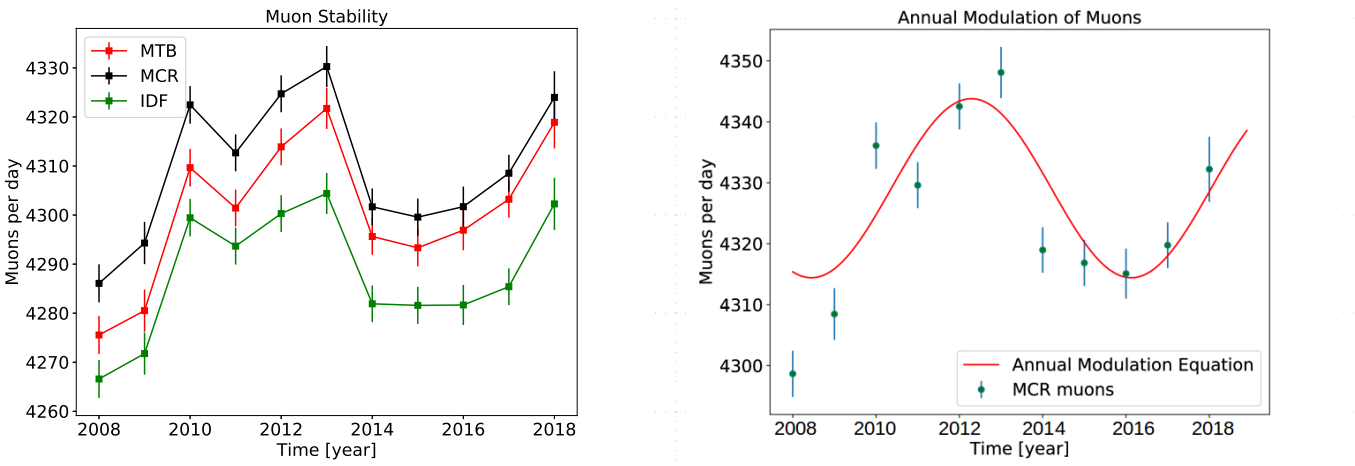

(a) (b)

Figure 4.2.3: (a) Stability of the three detector flags over the years. (b) Annual modulation observed as reported in [52].

4.2.1 ^{9}Li-^{8}He Background

The ^{9}Li-^{8}He background, the spallation products of muons, can affect the antineutrino analysis as they can imitate IBD signals.

$$\mu + {}^{12}\mathrm{C} \rightarrow \mu' + {}^{9}\mathrm{Li} + 3p, \;\; \mu + {}^{12}\mathrm{C} \rightarrow \mu' + {}^{8}\mathrm{He} + 4p \tag{4.2.2}$$

$$^{9}\mathrm{Li} \rightarrow e^{-} + \bar{\nu}_e + n + \alpha + {}^{4}\mathrm{He}, \;\; {}^{8}\mathrm{He} \rightarrow e^{-} + \bar{\nu}_e + n + \alpha + {}^{7}\mathrm{Li} \tag{4.2.3}$$

The decay of ^{9}Li to the stable ^{4}He has a branching ratio (BR) of 51% while the BR of the ^{8}He transition emitting neutrons is less than 16%.
The IBD signals from the ^{9}Li and ^{8}He transitions are estimated for antineutrino analysis by first looking for IBD signals within 2 s after a muon has been detected. The decay time τ is calculated after performing an exponential fit to the distribution of the time difference between the prompt event and muon, dt(prompt-muon). After disregarding the fast neutrons until 2 ms, the time window [2ms, 2s] has [exp(-0.002/τ) - exp(-2/τ)] = x% of all produced signals from ^{9}Li-^{8}He. The signals in the [2s, ∞] time window is exp(-2/τ) = y% of the total signals. Thus, the number of IBD signals in the antineutrino candidate sample can be calculated as:

$$N_{\text{Li-He}} = N_{\text{IBD}} * y/x \tag{4.2.4}$$

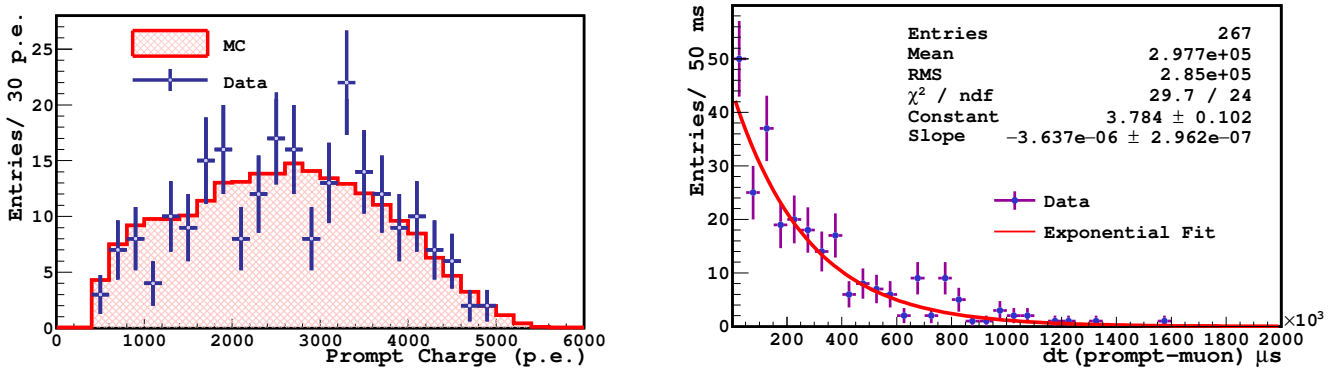

(a) (b)

Figure 4.2.4: (a) Comparison of the prompt energy spectra of ^{9}Li-^{8}He candidates for data and MC for the standard selection cuts (b) Exponential fit of the absolute time difference between the prompt event and muon (dt(prompt-muon)) for the 267 ^{9}Li-^{8}He candidates without any DFV cut.

In the previous geoneutrino analysis, 175 ^{9}Li-^{8}He candidates were found passing all the selection cuts and 194 without any fiducial volume cut as shown previously (Figure 3.2.1). The decay time was calculated as (0.294 ± 0.022) s by fitting the dt(prompt-muon) distribution of the 194 candidates. The $N_{\text{Li-He}}$ was estimated to be (0.194 ± 0.015) within the geoneutrino candidate sample. The systematic error that can arise due to the exponential fit was also taken into account and the final estimate can be given as $N_{\text{Li-He}} = 0.194 \pm 0.015\ (\text{stat})^{+0.124}_{-0.088}\ (\text{syst})$. Extending the same logic to the current statistics, there were 230 candidates that satified all the standard selection cuts. The decay time was calculated as (0.275 ± 0.023) s for the 267 candidates without any DFV cut as shown in Figure 4.2.4 (b) and $N_{\text{Li-He}}$ was estimated as (0.162 ± 0.011). Taking the error in the decay time fit also into consideration,

$$\boxed{N_{\text{Li-He}} = 0.162 \pm 0.011(stat)^{+0.14}_{-0.07}(syst)}$$

4.2.2 ^{12}B Background

While studying the hadronic background for SOX [20] with enlarged energy and distance cuts, it was noticed that there was an additional exponential in the dt(prompt-muon) window with a decay time of around 30 ms along with the ^{9}Li and ^{8}He exponentials (Figure 4.2.5). When looking at the dt(prompt-delayed) window, an additional exponential component was found when extending the window from 1280 μs to 200 ms. This decay time was around 30 ms as well (Figure 4.2.6). This indicated an extra hadronic background ^{12}B where the prompt and delayed coincidences were caused by the electron coming from two ^{12}B decays ($^{12}\mathrm{B} \rightarrow {}^{12}\mathrm{C} + \mathrm{e}^{-}$).

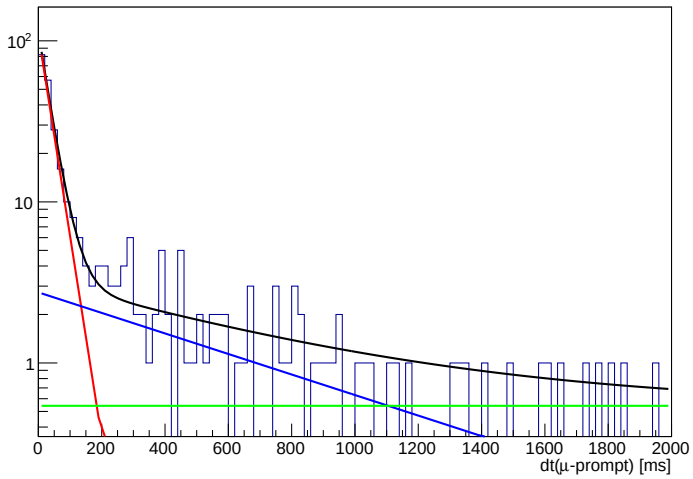

Figure 4.2.5: Distribution of time difference between muon and prompt events (dt(muon-prompt)) with enlarged cuts showing the ^{12}B exponential (red), ^{9}Li-^{8}He exponential (blue), and constant accidental background (green). The fit was performed by fixing the ^{9}Li-^{8}He background for standard selection cuts, and keeping ^{12}B and accidentals free [45].

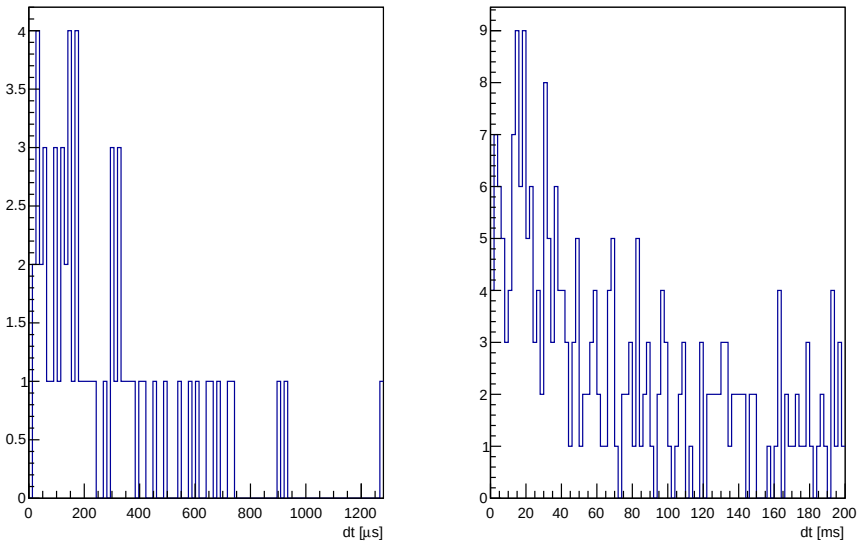

Figure 4.2.6: Distributions of time difference between the prompt and delayed events (dt(delayed-prompt)) the geoneutrino time window [20, 1280] μs (left) and for an extended time window of [20 μs, 200 ms] (right) for the standard selection cuts [45].

Since these events are very few in the geoneutrino selection time window of 20-1280 μs, given the production and branching ratios, this exponential is not fit separately, only a single exponential fit is performed for ^{9}Li, ^{8}He, and ^{12}B backgrounds in this analysis.

4.2.3 Untagged Muons

The mutual efficiencies of the three detector flags MTB, MCR, and IDF were studied over the years (Table 4.2.2) in order to estimate the amount of untagged muons that might affect the geoneutrino candidate sample.

Visible Energy (nhits)	**Mutual Efficiency** ϵ	**vs IDF**	**vs MTB**	**vs MCR**
$\geq$80	ϵ_{idf}	x	0.9885±0.004	0.9889±0.0004
$\geq$80	ϵ_{mtb}	0.9955±0.004	x	0.9983±0.0004
$\geq$80	ϵ_{mcr}	0.9886±0.004	0.9920±0.0004	x
80-110	ϵ_{idf}	x	0.0930±0.0020	0.0932±0.0020
110-500	ϵ_{idf}	x	0.5703±0.0020	0.5676±0.0020
500-7k	ϵ_{idf}	x	0.9959±0.0005	0.9957±0.0005
$\geq$7k	ϵ_{idf}	x	1.0000±0.0006	1.0000±0.0006

Table 4.2.2: Mutual efficiencies of the three detector flags for the period Dec 2007 - May 2018.

Since all the detector flags were not stable during the initial period of data taking i.e before Dec 2007, the plots of mutual efficiencies (Figure 4.2.7) are shown for Jan 2008 - May 2018. We can see that the IDF efficiency has been decreasing since 2014, a closer look on each of the IDF conditions in the three energy ranges listed in Table 4.2.1 indicated that the efficiency has been decreasing in the lower energy ranges and this can be attributed to the decreasing amount of active PMTs in the detector. This is discussed in detail in Section 8.1. The MCR efficiency, even though being the most efficient after 2011 has only been slowly increasing since 2008 (Figures 4.2.7 (e) and 4.2.7 (f)). MTB efficiency has been mostly stable over the years (Figures 4.2.7 (c) and 4.2.7 (d)).
The highest mutual inefficiency is 1.15%, the inefficiency of the IDF flag w.r.t the MTB flag and the highest mutual efficiency is 99.83%, the efficiency of the MTB flag w.r.t the MCR flag can be used to calculate the overall inefficiency of the three muon flags as 1.15*(1-0.9983) = 0.196%. This inefficiency can be used to calculate the possible amount of untagged muons that might affect the geoneutrino analysis which is explained in Section 8.4. The amount of IBD-like signals arising from untagged muons reported in the 2015 paper with a livetime of 1841.9 days was 0.12±0.01. Scaling it to the extended statistics of 2647 days, the amount of untagged muons can be given as 0.17 ± 0.01.

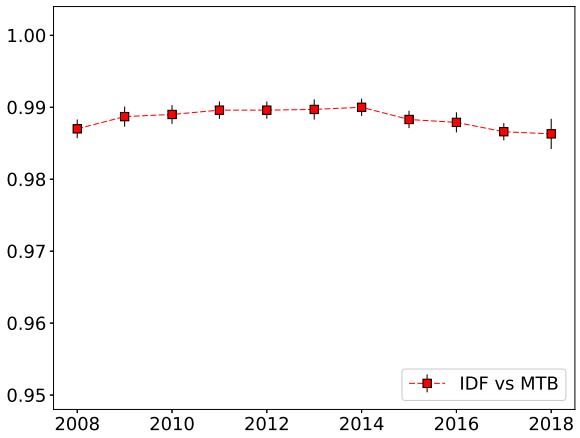

(a)

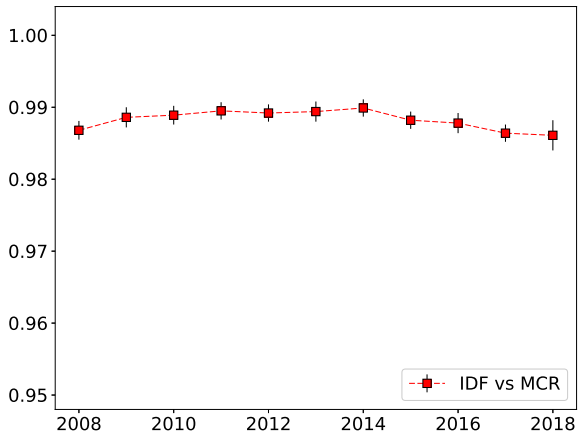

(b)

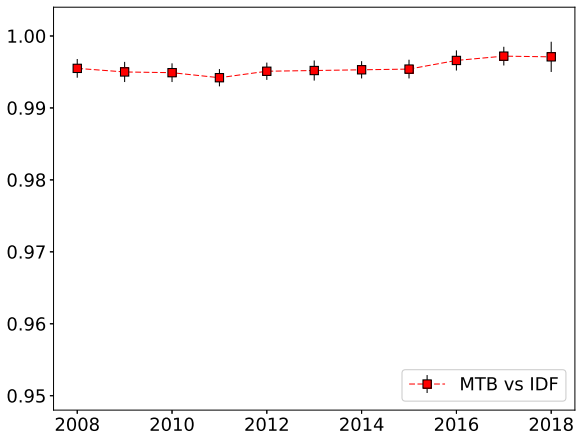

(c)

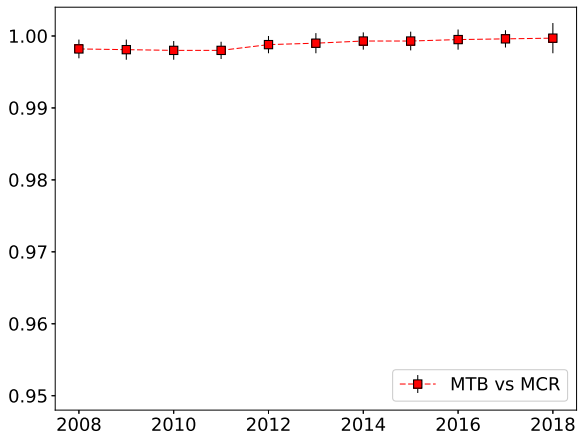

(d)

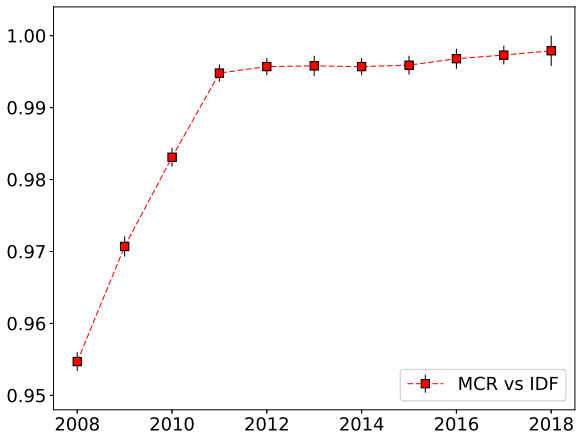

(e)

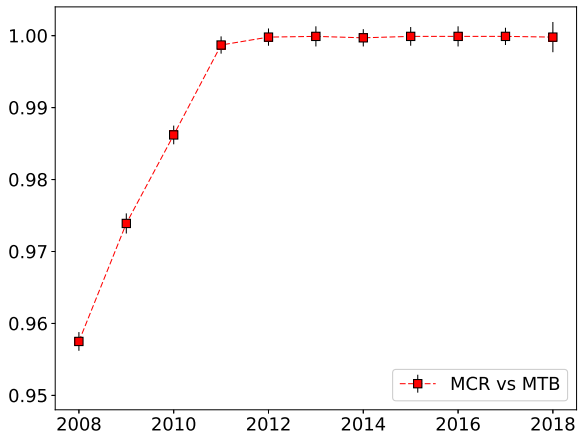

(f)

Figure 4.2.7: Mutual efficiencies of the three detector flags (period: Jan 2008 - May 2018).

4.2.4 Fast Neutrons

The muons that pass through the water tank and rock may produce fast neutrons that might be mistaken for IBD signals when they pass through the scintillator. The amount of fast neutrons due to the muons passing through the water tank can be searched using the same way IBD singals are searched for. The prompt signal can be produced by a scattered proton from neutron thermalisation and the delayed signal can be produced by the 2.2 MeV gamma due to neutron capture. The prompt event must be tagged by MTB or MCR. It should not be an IDF muon since the prompt event is not the muon which passes through the scintillator but the scattered proton from neutron thermalisation. The charge cut on the delayed should be between 100 and 1300 p.e. in order to include neutrons depositing energy in the buffer. Such prompt events without any energy cuts and delayed events in the tt128 gate were looked for in the geoneutrino time window [20,1280]μs without any dR and DFV cuts. This study was done for June 2007-January 2009. 50 coincidences were found but only one candidate satisfied all the geoneutrino selection cuts. The decay time obtained by fitting dt(prompt-delayed) distribution (Figure 4.2.8 (a)) was (250$\pm$50) μs, proving that all of them are not fast neutrons but simple buffer muons followed by neutrons. The charge distribution of the delayed events (Figure 4.2.8 (b)) indicated two classes of neutrons $<$ 400 p.e. and $>$ 600 p.e. The ones below 400 p.e. have been reported to possibly be 2.2 MeV gammas depositing energy in the buffer.

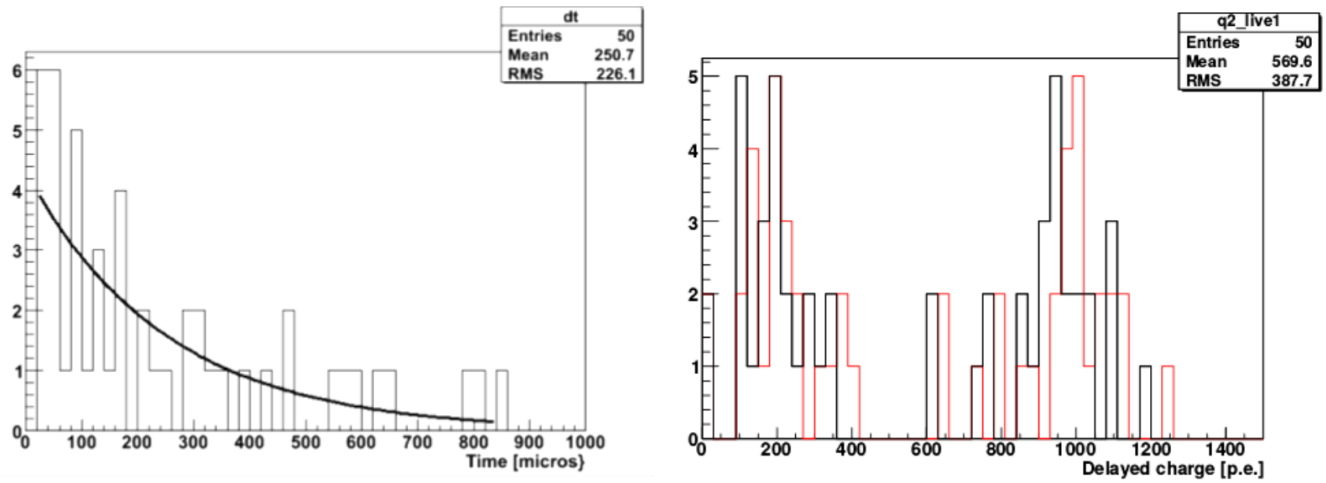

(a) (b)

Figure 4.2.8: (a) Distribution of time difference between the prompt and delayed events (dt(delayed-prompt)). (b) Charge distribution of delayed events with (red) and without (black) consideration of empty boards (Figures used from [40]).

In order to calculate the impact of fast neutrons from the rock, 5 million neutrons were simulated according to their energy and angular distribution in Gran Sasso. Only one prompt-delayed pair of energy with prompt energy of 9000 p.e. was found and the limit was reduced to 0.06 when taking into account the measured neutron fluxes [44]. Since the prompt energy spectra seen in the detector is between 408 and 4000 p.e. and since the simulation did not take into account that most of the neutrons are accompanied by muons, the final limit on the background was reported as $<$ 0.05 from an analytical calculation for 535 days of livetime [25].
The limits reported for fast neutrons from muons in water tank and from muons in rock in the 2015 paper for a livetime of 1841.9 days were $<$ 0.01 and $<$ 0.43 respectively. Extending the values to the current statistics with a livetime of 2647 days, the limits can be given as $<$ 0.014 and $<$ 0.62 for fast neutrons due to muons in the WT and muons in the rock, respectively.

4.3 Random Coincidences

In the detection time window of [20, 1280] μs, it is possible that there are random coincidences. In order to evaluate such coincidences, events outside the antineutrino search time window were counted and scaled back to the duration of antineutrino selection time window. Two kinds of backgrounds were evaluated during the previous analysis.

(1) The accidental background was evaluated by looking for events in the time window [2, 20] s which gave a constant accidental rate as shown previously in Figure 3.2.2 (a). Scaling the 3153±56 events to the geoneutrino time window of [20,1280] μs i.e. 3153*0.001260/18 gives N_{acc} = 0.221 ± 0.004.

(2) When coincidences were searched in the time window [2 ms, 2 s], 376 events were found. The number of expected events after scaling the accidentals to the [2ms,2s] time window, i.e. 3153*(2-0.002)/18 is 350±6 events. There was an excess of 26±20 events indicating a time correlated component within 2 ms to 2 s. This background was not very prominent for the standard geoneutrino selection cuts owing to the low statistics as shown in Figure 3.2.2 (b). When the cuts were relaxed, for example by removing the DFV and dR cuts, the mean lifetime of this time correlated compound could be extracted. The decay time obtained from the fit during the 2015 analysis was 1.124±0.239 s. In the [2 ms, 2 s] time window, a fraction equal to [exp(-0.002/1.124) - exp(-2/1.124)] = 0.829 of events is expected while in the [20, 1280] μs time window, [exp(-0.00002/1.124) - exp(-0.00128*1.124)] = 0.00112 is expected. By scaling, 26*0.00112/0.829 = 0.035 events were obtained for the geoneutrino time window. Hence $N_{correlated}$ was estimated as $0.035 \pm 0.028(\text{stat})^{+0.006}_{-0.004}(\text{syst})$.

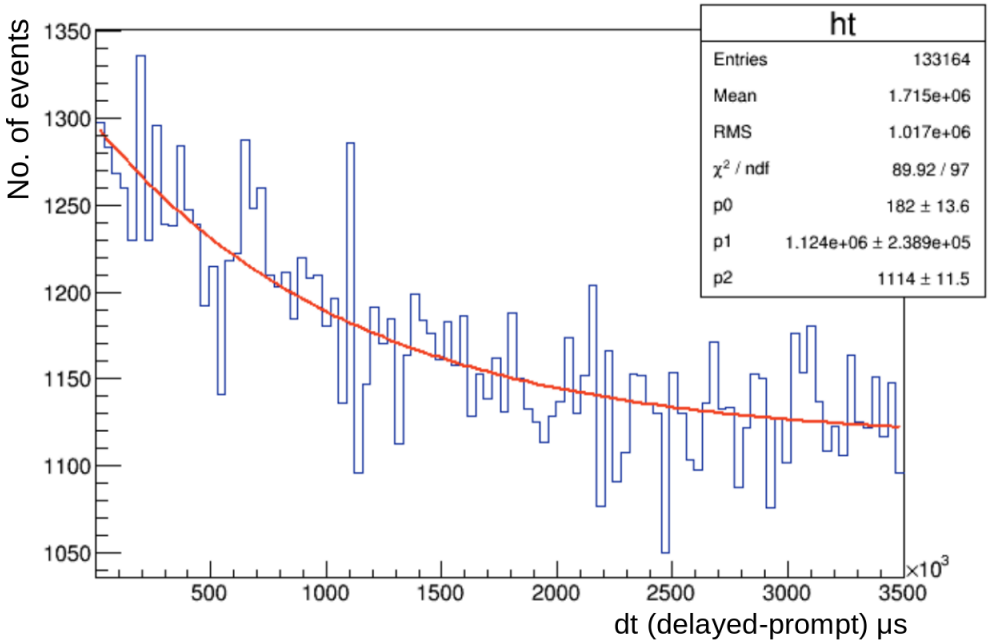

Figure 4.3.1: Distribution of time difference between prompt and delayed (dt(delayed-prompt)) events in without any dR and DFV cuts. [27]

The charge spectra of the prompt events of these random coincidences is shown in Figure 4.3.3 (a). It was found that the entire time window [2 ms, 2 s] should be used to evaluate the random coincidences, when studying this background for SOX [20]. This behaviour of a decreasing time correlated background and a constant accidental background has a rather simple explanation. It is due to the implementation of the 2 s dead time after internal muons. The probability to see a muon in between the prompt and delayed events and thus the probability to reject the delayed

events decreases until 2 s i.e. p0 · exp(-p1 · dt) and becomes a constant after 2 s i.e. p0 · exp(-p1 · 2). Thus, the actual background rate is the constant background rate previously evaluated along with an additional suppression factor of exp(-p1 · dt). Here p1 is the muon rate observed in Borexino i.e. 0.05 Hz which is seen in the Figure 4.3.2.

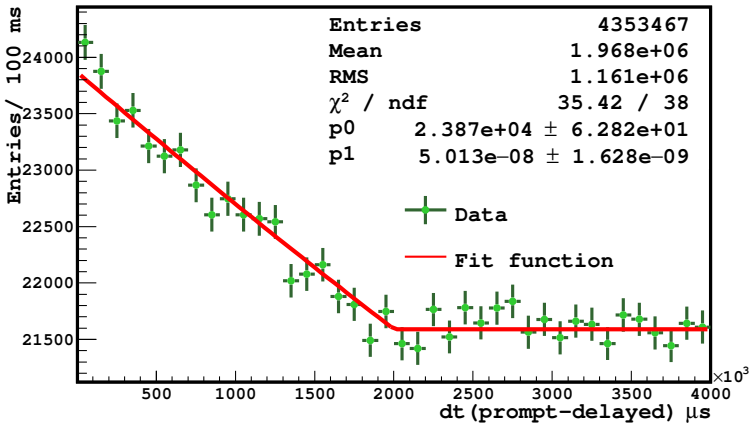

Figure 4.3.2: Absolute time distribution between prompt and delayed (dt(prompt-delayed)) events showing a decreasing accidental rate until 2s and a constant accidental rate after 2s. Antineutrino candidates selected with relaxed cuts.

The fit function [45] used was:

$$dt{<}2s : r_{acc}(dt) = p0 \cdot \exp(-p1 \cdot dt) \tag{4.3.1}$$

$$dt{>}2s : r_{acc}(dt) = p0 \cdot \exp(-p0 \cdot dt) \tag{4.3.2}$$

Including the statistics from March 2015 to May 2018 (Figure 4.3.3 (b)), the accidental rate in the time window [2s , 20s] is 4714*0.001260/18 = 0.330±0.005 events. Taking the suppression factor exp(-p1 · 2s) = exp(-0.05 · 2) = 0.9048 into account, the accidental background can be obtained as 0.330/0.9048 = 0.365±0.005 events. Thus, the number of random coincidences in the geoneutrino sample after taking into account the errors due to the fit can be given as:

$$\boxed{N_{\text{random}} = 0.365 \pm 0.005(stat) \pm 0.0012(syst)}$$

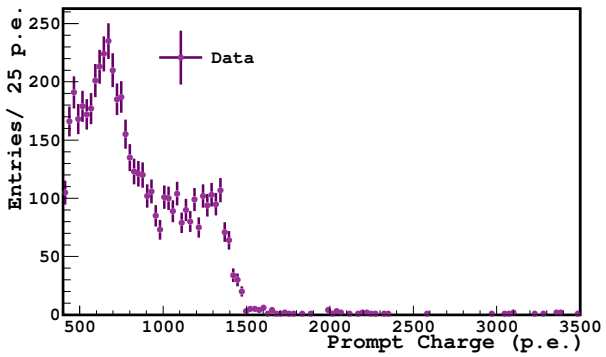

(a)

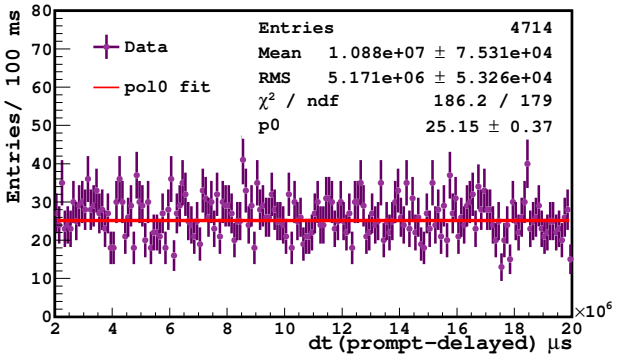

(b)

Figure 4.3.3: (a) Prompt energy spectra for the random coincidences. (b) The absolute time distribution between prompt and delayed (dt(prompt-delayed)) events for the constant accidental rate in the window [2s, 20s].

4.4 (α, n) Background

The main source of alpha particles in the detector is due to the internal radioactivity of ^{210}Po coming from the ^{238}U chain and also additionally from various parts of the detector like storage tanks and pipes. The decay time of ^{210}Po ($^{210}\text{Po} \rightarrow {}^{208}\text{Pb} + \alpha$) is approximately 200 days. The ^{210}Po rate has been out of equilibrium since the beginning of data taking and its evolution (Figure 4.4.1) has been carefully studied.

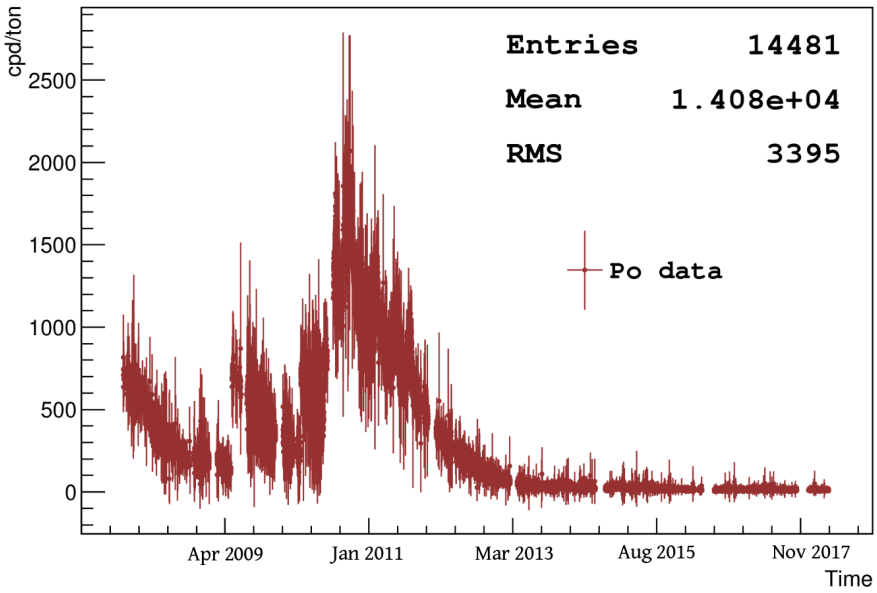

Figure 4.4.1: Evolution of ^{210}Po in the Borexino detector (Every data point corresponds to a single (≈6h) run from December 2007 to May 2018).

The natural isotopic abundance of ^{13}C in the scintillator is 1.1%. The alpha particles from the ^{210}Po decay can react with ^{13}C. The de-excitation gammas from ^{16}O and ^{12}C* can imitate the prompt signal of IBD and the the thermalisation of the neutrons can imitate the delayed signal of IBD. This is depicted in Figure 4.4.2 (a) and the MC spectrum of for such prompt events is shown in Figure 4.4.2 (b). The three peaks in the MC spectrum correspond to the imitation of the prompt signal from the recoiled proton, ^{12}C* from neutron, and ^{16}O*, respectively.

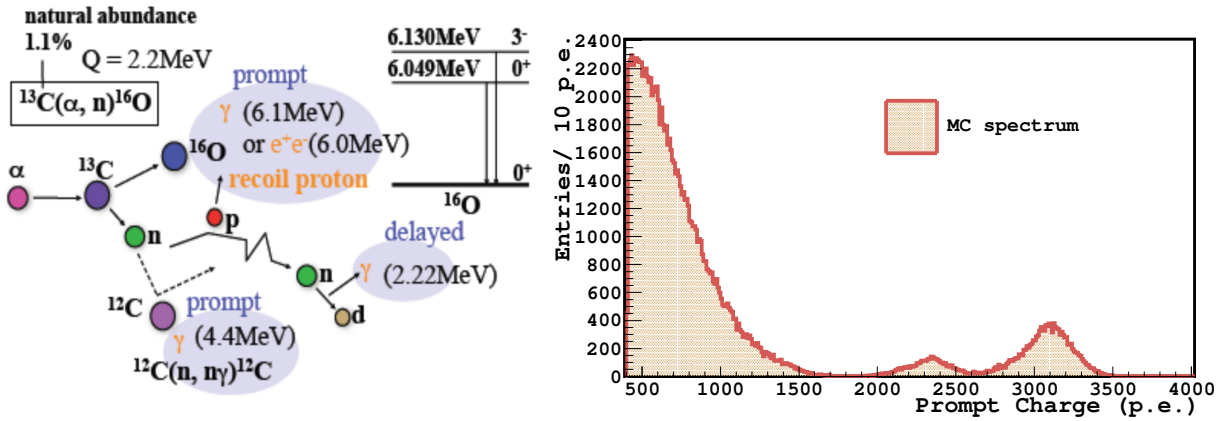

(a) (b)

Figure 4.4.2: (a) ^{13}C(α,n)^{16}O reaction [37]. (b) The MC prompt energy spectrum of the (α, n) reaction in Borexino for the geoneutrino selection.

N(α, n), the amount of (α, n) background calculated in 2010 using the probability of interaction from MC was 0.014 ± 0.001 events/100 ton·year. The mean activity of ^{210}Po for a DFV cut of 30 cm is 14.1 cpd/ton, which is 1.02 times the mean activity in 2010 (12.8 cpd/ton). Therefore N(α, n) = (0.014 ± 0.001)*1.02 = (0.014 ± 0.001) events/ 100 ton·year. Considering the current exposure of 1271 ± 74 ton·year, N(α, n) in the scintillator = 0.178 ± 0.01. The (α, n) background due to the buffer reactions was calculated using MC and a limit was set to 0.43 events for the 2015 analysis. The limit on this can be given as < 0.62 when considering the current statistics.

4.5 (γ, n) Background

The (γ, n) reactions due to the γ's produced by the external backgrounds can imitate IBD signals, hence it is important to evaluate this type of background depending on the parent nuclides. The (γ, n) reaction thresholds for the most abundant isotopes in Borexino are listed in Table 4.5.1

Target	**Abundance**	**Threshold (MeV)**
^{1}H	99.985%	-
^{2}H	0.015%	2.22
^{3}H	-	6.26
^{12}C	98.90%	18.7
^{13}C	1.10%	4.95
^{14}C	-	8.18
^{14}N	99.634%	10.6
^{15}N	0.366%	10.8
^{16}N	-	2.49
^{16}O	99.762%	15.7
^{17}O	0.038%	4.14
^{18}O	0.200%	8.04
^{19}O	-	3.96

Table 4.5.1: (γ, n) reaction thresholds for most abundant nuclides in Borexino [3].

The lowest energy threshold is given by the gamma reaction on ^{2}H (2.22 MeV). Taking into account the positron candidate energy threshold used in the analysis (0.8 MeV), it can be concluded that only energies higher than 3 MeV could be source of background. The U and Th chains inside the scintillator do not emit gammas of energies above 3 MeV, therefore intrinsic scintillator/ vessel contaminations are not an important source of background. This analysis was performed on data between June 2007 and September 2009 where 9001 events at energies above 2.9 MeV were selected after applying a 2 s veto after all internal muons [39]. The induced reaction yield was calculated using the gamma's penetration depth into PC. The gamma ray attenuation coefficients in the scintillator was calculated using the XCOM program [1]. A value of λ= 29 (39) cm was expected for a 3(5) MeV gamma. A conservative value of 2 mbarn for the ^{2}H(γ,n) reaction cross section was considered and the photodisintegrations of D in Borexino was calculated as:

Yield (D) $< N_\gamma * N_D * \sigma * 3\lambda = 9001 * 7.8\ 10^{18} * 2\ 10^{-27} * (3*29) = 1.22\ 10^{-2}$ events in 584 days.

Photodisintegration of ^{13}C has a threshold of 4.95 MeV. 601 events selected at energies above 4.8 MeV (4.95 MeV corrected for energy resolution) gave the following yield:

Yield (^{13}C) < N_γ * N_{13C} * σ * 3λ = 610 * 4.33 10^{18} * 1 10^{*26} * (3*39) = 3.1 10^{-3} events in 584 days.

No events above 18.7 MeV were found, indicating no such reactions for ^{12}C nuclides.
The (γ, n) limit reported for the 2013 analysis for an exposure of 1353 days was < 0.04. Extending it to the extended statistics of 2647 days, the limit can be given as 0.04*1.4 i.e. (γ, n) < 0.06 for the current statistics with standard selection cuts.

4.6 ^{214}Bi-^{214}Po Coincidences

The Water Extraction (WE) cycles done during July 2010 to August 2011 introduced Rn background of the order 10^5 and hence ^{214}Bi-^{214}Po background.

$$^{222}\text{Rn} \xrightarrow{\alpha} {}^{218}\text{Po} \xrightarrow{\alpha} {}^{214}\text{Pb} \xrightarrow{\beta} {}^{214}\text{Bi} \xrightarrow{\beta} {}^{214}\text{Po} \tag{4.6.1}$$

When increasing the charge window during the previous analyses, there were a lot of additional antineutrino-like events found during this period. ^{214}Bi (beta spectrum has an end point of 1800 p.e.) can imitate the prompt signal while the (α+γ) decay of ^{214}Po whose branching ratio is of the order 10^{-4} can imitate the delayed signal. The end point of this decay is around 860 p.e. and thus the Q_{min} of delayed for the geoneutrino analysis was increased to 860 p.e. in 2012, see Section 6.4.2. This background was estimated as 0.009 ± 0.013 for the 2015 analysis [41], and was scaled using the exposure as 0.013 ± 0.012 to give a conservative value for this work.

4.7 Comparison of Backgrounds with Previous Results

The backgrounds evaluated with the current statistics and with the statistics used in [7] are compared to the values published in [7]. The modification of the data validation procedure done in 2017, led to the removal of certain noisy runs in the previous dataset, which in turn led to a decrease of 40.8 days in the livetime. As a result, there was a difference of 3 antineutrino candidates while reproducing the previously published results. There were 77 antineutrino candidates found in 1841.9 days of livetime as reported in [7]. Thus the loss of 3 candidates lies within the expected loss of 2 ± 1 candidates in 40.8 days.
Small differences were found in the backgrounds as well. Even though candidates with high energy events between the prompt and delayed (multiplicity cut) events were eliminated in the estimation of ^{9}Li-^{8}He background in 2015, candidates with high energy events 2 ms before prompt and 2 ms after delayed were not eliminated. This led to a difference of 5 ^{9}Li-^{8}He candidates without any DFV cutand 3 ^{9}Li-^{8}He candidates with 30 cm DFV cut for the current analysis done with the old statistics.
The multipicity cut applied in the 2015 analysis was not extended to the evaluation of accidental background in 2015. Taking this and also the loss of 40.8 days into account, there is a difference of 319 candidates in the [2, 20] s time window for the evaluation of accidental background using the old statistics. The re-evaluation of the background without multiplicity cut yielded 3153 accidental candidates as previously reported.
All the other reported backgrounds are scaled using the livetime for the current statistics. The evaluated backgrounds in this work are consistent with the results published in [7].

Category	**Published values from [7]**	**This work with statistics from [7]**	**Current statistics with standard selection cuts**
Livetime	1841.9 days	1801 days	2647 days
Antineutrino Candidates	77	74	102
^{9}Li-^{8}He	$0.194^{+0.125}_{-0.089}$	$0.121^{+0.2}_{-0.05}$	$0.162^{+0.14}_{-0.071}$
Accidental coincidences (old)	0.221 ± 0.004	0.202 ± 0.004	0.330 ± 0.005 (2 - 20s)
Time correlated background	$0.035^{+0.029}_{-0.028}$	-	-
Accidental coincidences (new)	-	0.223 ± 0.004	0.365 ± 0.006 (2ms -20s)
(α, n) in scintillator	0.165 ± 0.010	-	0.178 ± 0.01
(α, n) in buffer	<0.51	-	< 0.73
(γ, n)	-	-	< 0.08
Fast n's (μ in WT)	<0.01	-	<0.014
Fast n's (μ in rock)	<0.43	-	<0.62
Untagged muons	0.12 ± 0.01	-	0.17 ± 0.01
Fission in PMTs	0.032 ± 0.003	-	0.046 ± 0.004
^{214}Bi-^{214}Po	0.009 ± 0.013	-	0.009 ± 0.013

Table 4.7.1: Antineutrino candidates and estimated backgrounds within the candidate sample evaluated with the statistics published in [7] and with current statistics compared to values published in [7].

5 Analysis Tools

5.1 Monte Carlo (MC) Simulations for Geoneutrino Analysis

The MC simulated charge distributions are used in the sensitivity study and in the final likelihood fit. To validate the MC simulation of neutron (IBD delayed candidate), the ^{241}Am-^{9}Be calibration data and MC were compared for the source placed at different positions to ensure that there are no issues in the MC simulated spectra used for the analysis. The n-capture peak on proton around 2.2 MeV (around 1000 p.e.) in data and MC agree well.

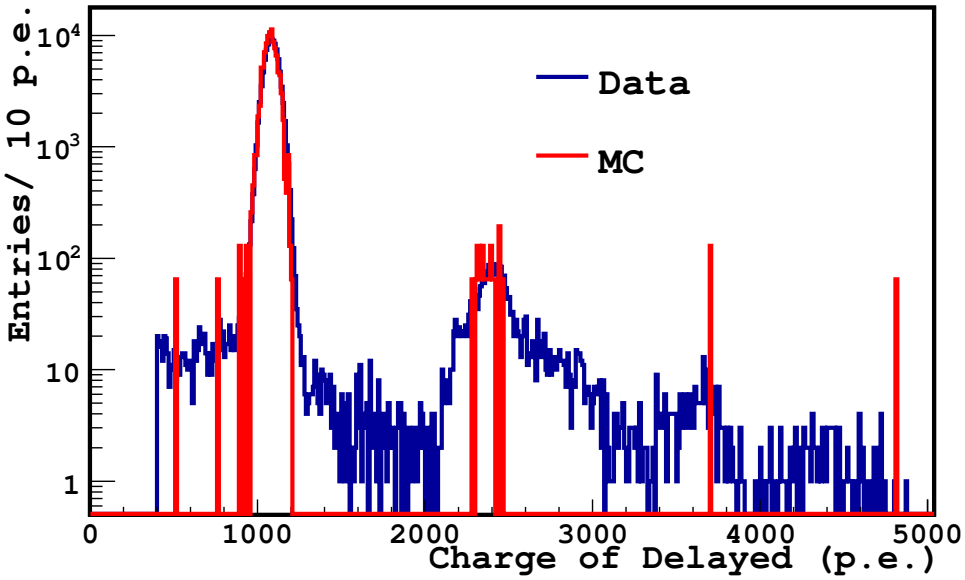

Figure 5.1.1: Comparison of the data and MC charge spectra of delayed events from ^{241}Am-^{9}Be calibration data for a single run where the source was placed at the center (MC was scaled to the number of events in the data for comparison).

The energy spectra of the prompt event for different signal and background components are shown in Figure 5.1.2. The prompt energy spectra of random coincidences was taken from data as shown in Figure 6.6.2 (b). The MC simulations of ^{9}Li and (α, n) backgrounds were simulated for three equidistant runs in the analyswhile the remaining simulations were done for every run. The simulated number of events were distributed according to the livetime of every run. The MC simulation of only the ^{9}Li background was used and not the ^{8}He background after taking into account the branching ratio of their decay chains (BR), and their production ratios (PR) (taken from [16]).

$$\frac{(BR \cdot PR)_{Li}}{(BR \cdot PR)_{He}} = \frac{4}{0.007}. \tag{5.1.1}$$

The effect of (α,n) background in the inner buffer (IB), outer buffer (OB), and in the scintillator (IV) was studied. Two million (prompt + delayed) events were simulated for the OB but none of them passed the geoneutrino selection cuts. Only around 3000 out of the 783750 pairs passed the selection cuts for the IB. The prompt energy spectrum was exactly the same as the ones generated in the scintillator, closer to the IV. Therefore, only the events simulated in the IV were used for the analysis. The number of events (prompt + delayed) generated for every component are as follows:

- Geoneutrinos with fixed U/Th ratio - 973514
- Reactor antineutrinos - 1922430
- Geoneutrinos from ^{238}U - 444243
- Geoneutrinos from ^{232}Th - 444243
- (α,n) in scintillator -81600
- ^{9}Li background - 100000

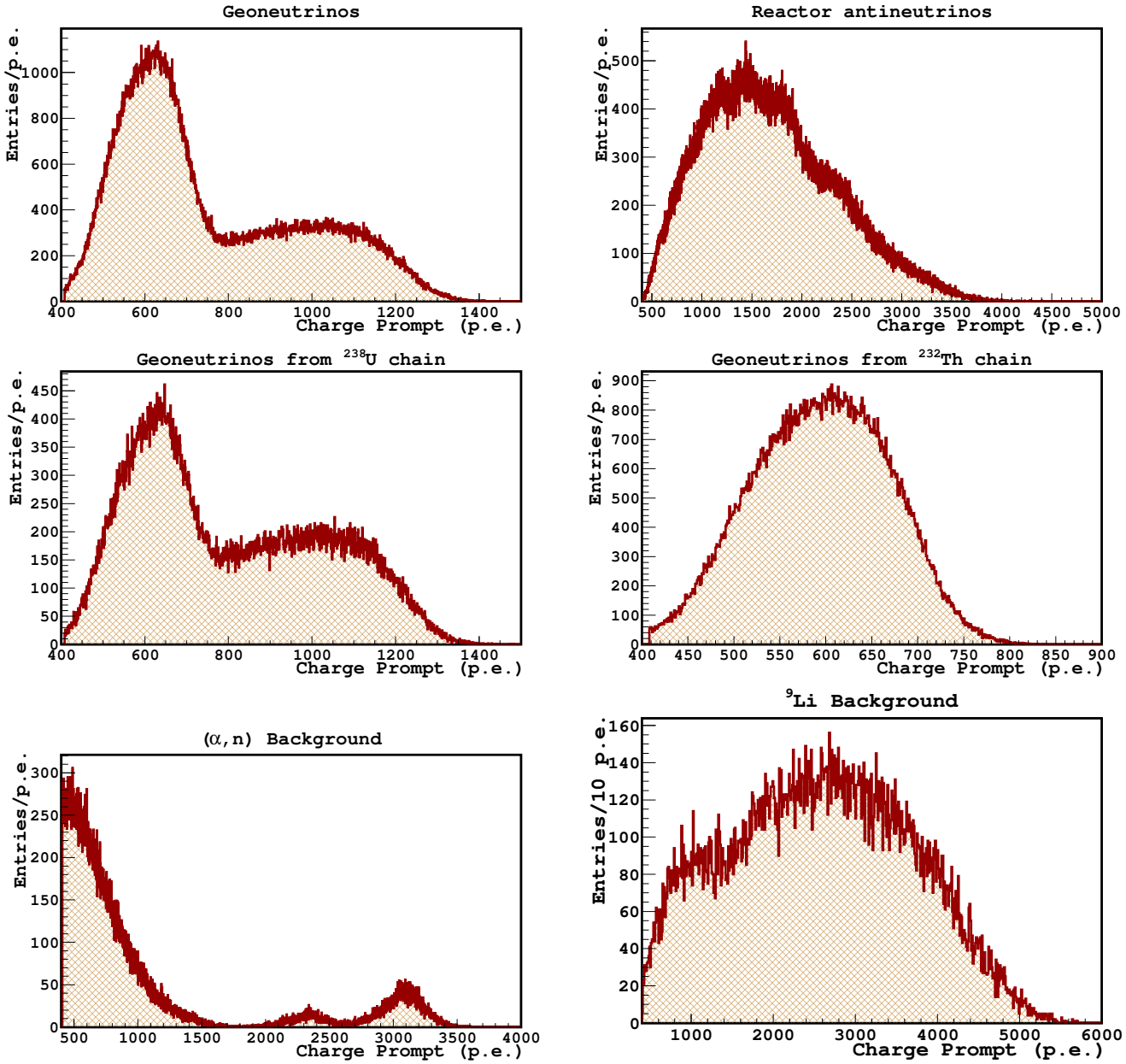

Figure 5.1.2: Energy spectra of prompt events from signal and backgrounds obtained from MC. These spectra are used in the sensitivity studies and likelihood fit.

5.2 Likelihood Fit

A likelihood fit is performed using the shapes of the signal and backgrounds from the MC prompt charge spectra (from data for random coincidences) and the prompt charge of the final antineutrino candidates. This is done using RooFit, a toolkit in ROOT framework which is used for modeling probability distribution functions (p.d.f.s) in a compact and abstract way [2]. Using the

MC generated prompt charge spectra for the signals and backgrounds, p.d.f.s are generated for the different components using a charge in an optimized fit range. An unbinned maximum likelihood fit is done on the data points using these p.d.f.s to create higher dimensional p.d.f.s. The amplitude of the different non-antineutrino background components is constrained using defined models and can be used to perform the fit.
In the geoneutrino analysis, the fit is performed by leaving the geoneutrino and reactor antineutrino components free. In the previous analysis, the MC spectra were rebinned to 20 p.e. per bin while in the current analysis, 1 p.e. binning is used to remove the small bias (2%) in the sensitivity studies and to be more precise. The non-antineutrino backgrounds were fit by defining fit ranges between -1σ and +1σ of their expected values during the previous analysis. In the current analysis, the fit ranges for the non- antineutrino backgrounds are constrained using Gaussian pull terms. Two kinds of fit are performed for the geoneutrino analysis. The first type is performed by fixing the chondritic ratio of 3.9 for U/Th and the second type is performed by leaving the U and Th parameters free.

5.3 Sensitivity Tool

The sensitivity tool used for JUNO sensitivity to measure geoneutrinos [9] was adjusted for the current geoneutrino analysis with Borexino. It is a method of studying the effect of the different combinations of selection cuts on the precision of the measurement. The method of sensitivity studies is as follows:

(1) For a given set of selection cuts, the exposure, efficiency, backgrounds are estimated. The p.d.fs of the prompt energy are also used.

(2) We generate 10000 toy MC experiments based on the expected values of the geo, and reactor antineutrinos, and non-antineutrino backgrounds (explained in Section 6.6.3).

(3) Each of these experiments is fit using the same method used to fit the data, as explained in the previous subsection.

(4) Finally, a gaussian fit is performed for the FitResults/MCTruth ratio in order to estimate the statistical uncertainty (σ) for a certain set of selection cuts. The mean of the fit gives the systematic bias and the RMS gives the statistical uncertainty.

5.4 Results for 2015 Statistics from the Analysis Tools

The final gaussian fit performed using the inputs from the previously published results is shown in Figure 5.4.1. The uncertainty obtained is 24.27 $\pm$ 0.2%. This agrees well with the statistical uncertainty of 25.7 $\pm$ 3.4% published in [7]. Since, the errors in the published results are asymmetric ($23.7^{+6.5}_{-5.7}$ events), the uncertainty value was calculated as $\frac{(6.5+5.7)/2}{23.7}$ and the error on the uncertainty was calculated as ($\frac{5.7}{23.7}$ - $\frac{6.5}{23.7}$) for comparison purposes.

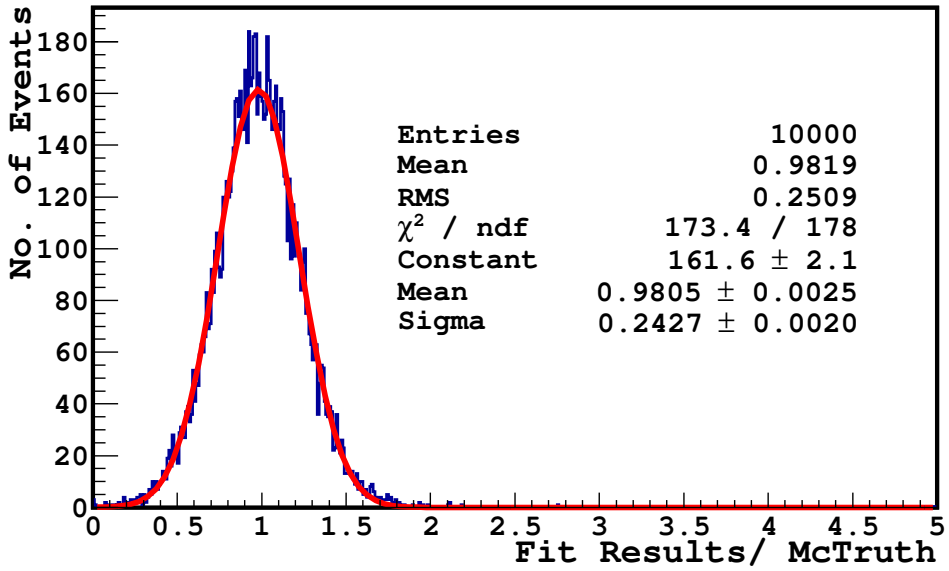

Figure 5.4.1: Gaussian fit performed for FitResults/McTruth ratio from the inputs used for the 2015 analysis showing an uncertainty of 24.27 ± 0.2%.

The likelihood fit was performed for the newly selected 74 candidates from the period used in [7]. The fit results obtained with the old and new way of constraining the non- antineutrino backgrounds for the fit with fixed U/Th ratio are given in Table 5.4.1.

Category	**2015 [7]**	**This work with old constraints for non- antineutrino backgrounds**	**This work with gaussian pull terms for non- antineutrino backgrounds**
N_{geo}	$23.7^{+6.5}_{-5.7}$	22.1 ± 5.8	22.1 ± 5.8
N_{rea}	$52.7^{+8.5}_{-7.7}$	49.1 ± 7.8	49.2 ± 7.8
N_{LiHe}	-	0.224 ± 0.121	0.123 ± 0.103
N_{random}	-	0.206 ± 0.004	0.202 ± 0.004
$N_{(alpha,n)}$	-	0.175 ± 0.02	0.165 ± 0.01

Table 5.4.1: Number of events for signal and background components reported in [7] compared to the current analysis on the same period.

The fit results obtained are shown in Fiqure 5.4.2. The obtained number of events are N_{geo} = 22.1 ± 5.8 events and N_{rea} = 49.2 ± 7.8. The TNU values (number of events per 10^{32} target protons per year with 100% efficiency) obtained using the number of events are S_{geo} = 43.9 ± 11.2 TNU and S_{rea} = 97.8 ± 15.5 TNU. This is to be compared to the values $S_{geo} = 43.5^{+11.8}_{-10.4}$ (stat) TNU and $S_{rea} = 96.6^{+15.6}_{-14.2}$(stat) TNU reported in [7]

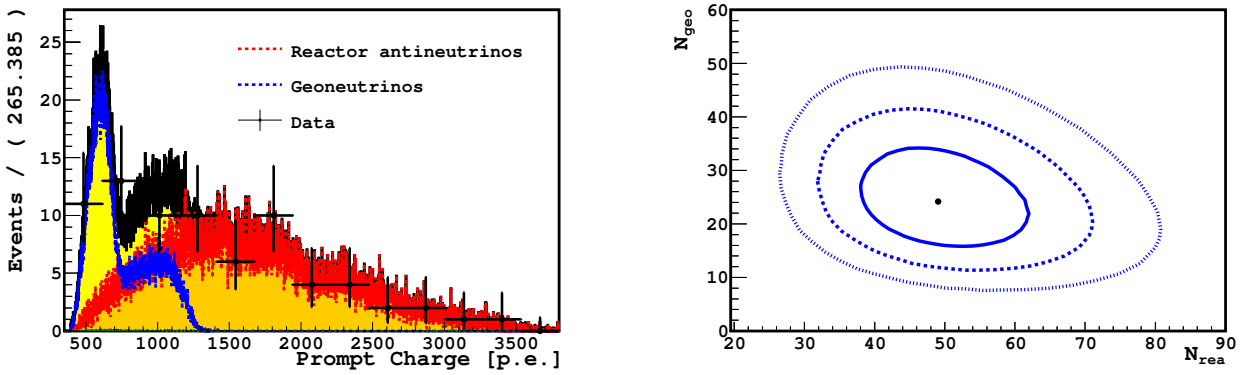

(a) (b)

Figure 5.4.2: (a) Likelihood fit and (b) 1σ, 2σ, and 3σ contours for N_{geo} and N_{rea} performed for statistics from [7] with fixed chondritic ratio.

The second type of fit is performed without using the U/Th chondritic ratio and leaving the ^{238}U and ^{232}Th components free as shown in Figure 5.4.3. The values obtained from this type of fitting are $N_U = 17 \pm 9.3$ events and $N_{Th} = 6.4 \pm 5.8$ events and $N_{rea} = 49.9 \pm 8.3$ events.

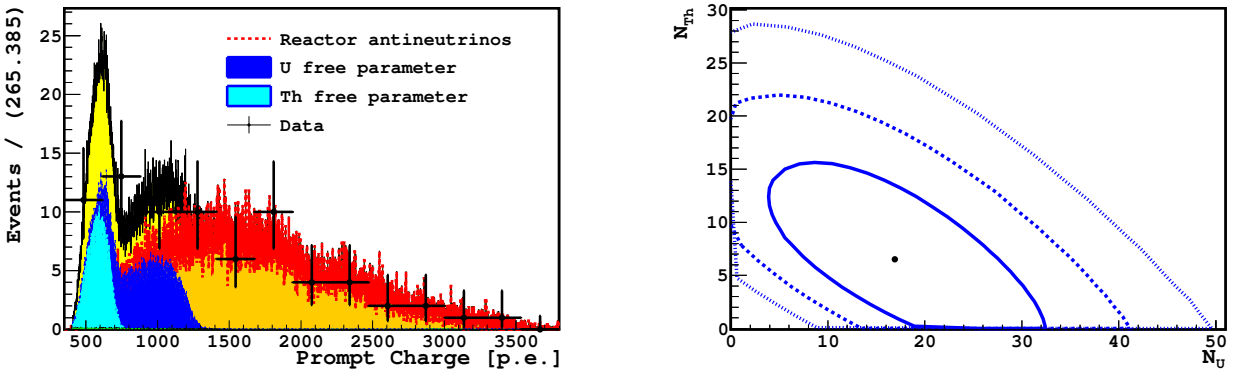

(a) (b)

Figure 5.4.3: (a) Likelihood fit and (b) 1σ, 2σ, and 3σ best-fit contours performed for N_U and N_{Th} for statistics from [7] with U and Th as free parameters.

6 Optimisation of Selection Cuts

6.1 Muon Vetoes

The live time to be considered for the geoneutrino analysis takes into account the dead time applied once a muon is detected, in order to eliminate the muons and the muon daughters. The detection methods and the efficiency of detection of these muons have already been explained in Section 4.2. In the previous geoneutrino analysis, a 2 ms dead time was applied for all external muons, i.e. muons that pass only through the outer detector (OD). This efficiently eliminated all the fast neutrons since 2 ms is about 8 times the neutron capture time of (254.5 ± 1.5) μs [15]. In addition, a dead time of 2 s was applied for the muons that pass through the inner detector (ID) to eliminate all hadronic backgrounds (^{12}B and ^{9}Li-^{8}He).

6.1.1 Muon Vetoes developed for SOX

Studies of cosmogenic background indicate that only a small fraction of muons are probable to produce neutrons that we detect [53]. As a result, the livetime of the detector can be increased by a considerable amount by identifying such muons. The internal muons were further classified into two types:

(1) Muons which are followed by neutrons (μ + n): Once, an internal muon is tagged by the MTB flag, a 1.6 ms time window is opened for fast neutrons. If there is one or more neutron clusters present in the tt128 gate, then the previous muon is classified as a muon followed by neutrons.

(2) Muons which are not followed by neutrons (μ - n).

The muons which are followed by neutrons have high probability of producing ^{9}Li-^{8}He background that can imitate IBD signals. Thus, a dead time cut of 2 s was applied only to such kind of internal muons and a 2 ms dead time was applied to the rest of the internal muons. This was the muon veto developed for the SOX (Short Oscillations with Borexino) [20] analysis and it led to an excess of events (23% more than expectation) indicating the presence of residual ^{9}Li-^{8}He and ^{12}B. This residual background was not an issue for SOX analysis owing to the high statistics of the antineutrino source. Given the low statistics of geoneutrino candidates, it was necessary to be more conservative with the ^{9}Li-^{8}He vetoes.

6.1.2 BTB 0 muons

Apart from the MTB muons, it was impossible to know if the remaining muons missed by the OD are followed by neutrons since a 1.6 ms gate is not opened for such events. Thus, a strict dead time cut of 2 s was necessary for such muons as well. These muons were a combination of IDF, MCR, and special muons (BTB 0 events) explained in Section 4.2.

Special d1 muons: Further studies on BTB 0 muons showed that there was a high amount of BTB 0 muons (38% of internal muons) and this was because there were many events tagged as special d1 (80-90% of BTB 0 muons). As explained in Section 4.2, special d1 tags events whose ratio of decoded-to-raw hits is less than 5%. Since this flag was introduced to tag muons that pass the detector when electronics is saturated, it also tagged first events after the tt128 gate when electronics sometimes gets saturated after high energy muons. Since the time difference between

the BTB 4 muon and special d1 muon was very small to cause any effect in the overall dead time, it did not affect the previous analysis when a 2 s dead time was applied to all internal muons. In the new analysis, an additional condition was added to the flag such that events preceded by BTB 4 + tt128 were not tagged as special d1. This decreased the dead time by 1.2% and increased the exposure by 0.13%. The amount of BTB 0 muons in the internal muon sample decreased by from 38% to 6.5%.

6.1.3 Spatial Cuts for Muons

In an independent study done for ^{9}Li-^{8}He vetoes [53], it was found that all muons followed by neutrons where the ^{9}Li-^{8}He candidates were seen always had more than 8000 decoded hits (Figure 6.1.1). Such muons cross not only the buffer, but also the scintillator thereby increasing the probability to detect also neutrons. It is also to be noted that 90% of the total hadronic background formed is due to this kind of muon. Thus, the remaining BTB 4 muons which were not followed by neutrons (μ - n) were sub-divided into two more categories.

(1) BTB 4 (μ - n) muons with decoded hits $\geq$ 8000
(2) BTB 4 (μ - n) muons with decoded hits $<$ 8000.

A 1.6 s dead time was applied to BTB 4 (μ - n) muons with more than 8000 decoded hits considering the fact that only around 10% of the candidates are from this kind of muons and also the fact that only 1% of the ^{9}Li-^{8}He candidates remains after 1.6 s. This can be seen in the dt(prompt-muon) distribution in Figure 3.2.1 (b). A 2 ms dead time was applied to the rest of the muons (μ - n) to reject fast neutrons. The hadronic background resulting from the different kinds of dead times is explained in detail in Section 6.6.2

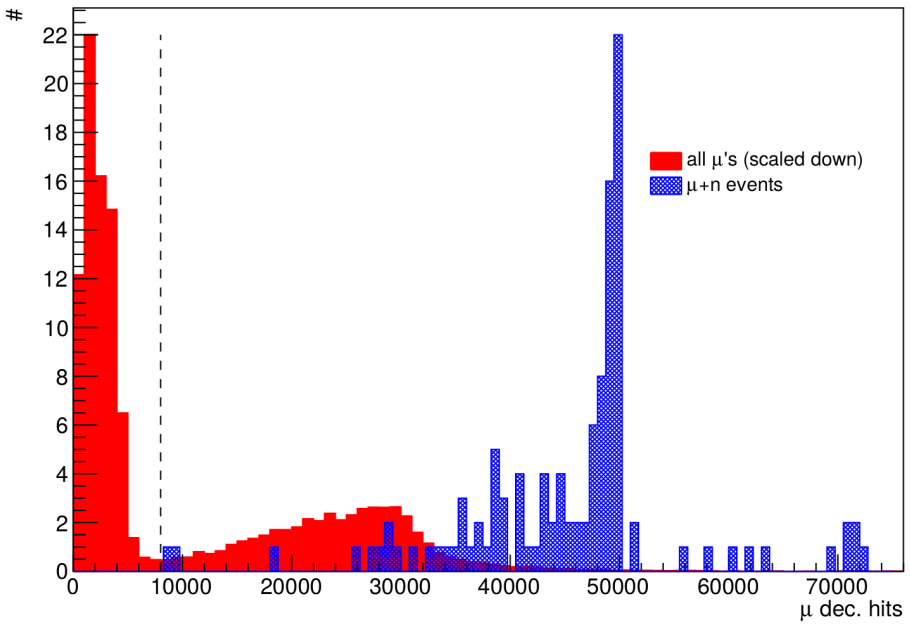

Figure 6.1.1: Comparison of decoded hits spectrum for all the muons (red) and (μ + n) (blue) which produce ^{9}Li-^{8}He candidates identified via coincidence tag [53].

Before the modification of the special d1 flag, the increase in livetime was only 1.8% with these spatial vetoes and an additional 4 candidates were found when the expectation was 2±2 candidates after scaling the exposure. The expected increase in the exposure was 6.6 ± 0.8 % when considering an ideal rate of 4300 internal muons per day and the amount of each kind of muon. After changing the special d1 condition, the increase in livetime was 7.3%.

6.1.4 Inclusion of FADC Analysis with Laben Analysis

The FADC system identifies muons using their pulse shapes. It has a different DAQ time window and different trigger types as previously explained in Sections 2.4 and 4.2. In the new analysis, the identification of FADC muons was done along with that of the laben muons. Every Borexino event corresponds to 0 or more FADC events defined as FADC clusters.

(i) Identification of FADC events: If the FADC system was active during data taking and if a particular event has FADC clusters, the event goes through the next identification process.

(ii) Distinction between muons and noise: If an event has a muon FADC cluster, it is identified as a muon using booleans developed for FADC analysis. This distinction is done using pulse shape analysis by the FADC system.

(iii) Differentiating external and internal FADC Muons: Further, if the muons had an FADC trigger type 8 or 41, they were classified as external FADC muons and the remaining muons were classified as internal FADC muons.

(iv) Dead time for exclusive FADC muons: A 2 s dead time was applied to the internal FADC muons and a 2 ms dead time was applied to the external FADC muons that were tagged exclusively by the FADC system and not the muon detector flags explained in Section 4.2.

This resulted in a 0.13% increase in dead time and a 0.02% decrease in exposure in comparison to the exposure reported in [7]. It also eliminated one geoneutrino candidate which was actually a muon missed by the OD and ID muon flags. This muon was also eliminated in the previous analysis once a final independent check was done on the geoneutrino candidate sample.

The new muon vetoes yielded five more candidates for the standard selection cuts when the expectation from scaling the livetime was 7±3 candidates After optimising all the selection cuts, there were 6 candidates resulting from the new muon vetoes. The increase in the livetime led to an improvement in precision of 0.6% which is discussed in Section 6.6.4. The final muon vetoes for the different kinds of muons are summarized in Figure 6.1.2.

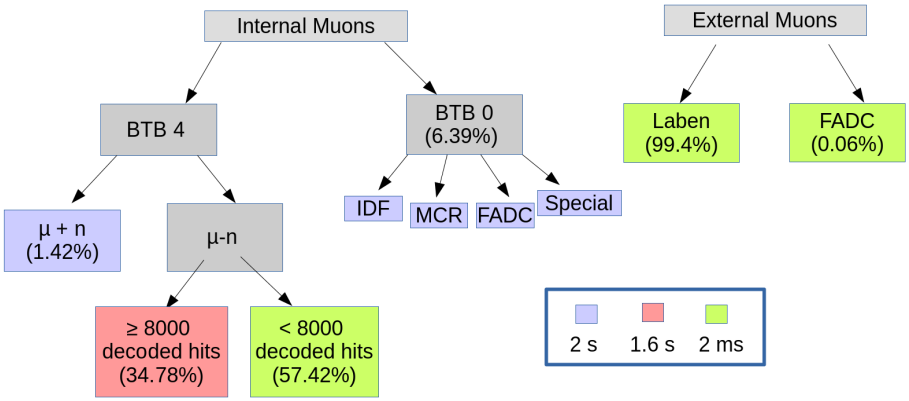

Figure 6.1.2: Scheme of the new muon vetoes with the relative amount of each category of muon. External muons constitute around 50% of the total muons and contribute to 1% of the dead time.

6.2 Time and Space Correlation

Optimum selection cuts for the time and distance between the prompt and delayed are required in order to balance the correlations between signal and the number of random coincidental back-

ground and minimize the Signal-to-Background (S/B) ratio.

6.2.1 Distance between Prompt and Delayed (dR) Events

In the previous analysis, the distance between the prompt and the delayed events (dR) was required to be less than one meter. In this study, the behavior of dR = 1 m and dR = 1.5 m on the S/B ratio was studied where S and B are defined as follows:

$$S = \frac{\text{No. of events passing the selection cuts in the geoneutrino MC sample}}{\text{No. of geoneutrino events generated in MC in a certain fiducial volume}} \tag{6.2.1}$$

$$B = \frac{\text{No. of accidentals passing the selection cuts}}{\text{Total No. of accidentals with extended selection cuts}} \tag{6.2.2}$$

The extended selection cuts for the accidental sample were chosen as $Q_{prompt} > 400$ p.e., 400 p.e. $< Q_{delayed} < 3000$ p.e., dR < 2.5 meters, no DFV cut, dT between 2-20 s, $Gatti_{delayed} < 0.015$ and multiplicity cut.

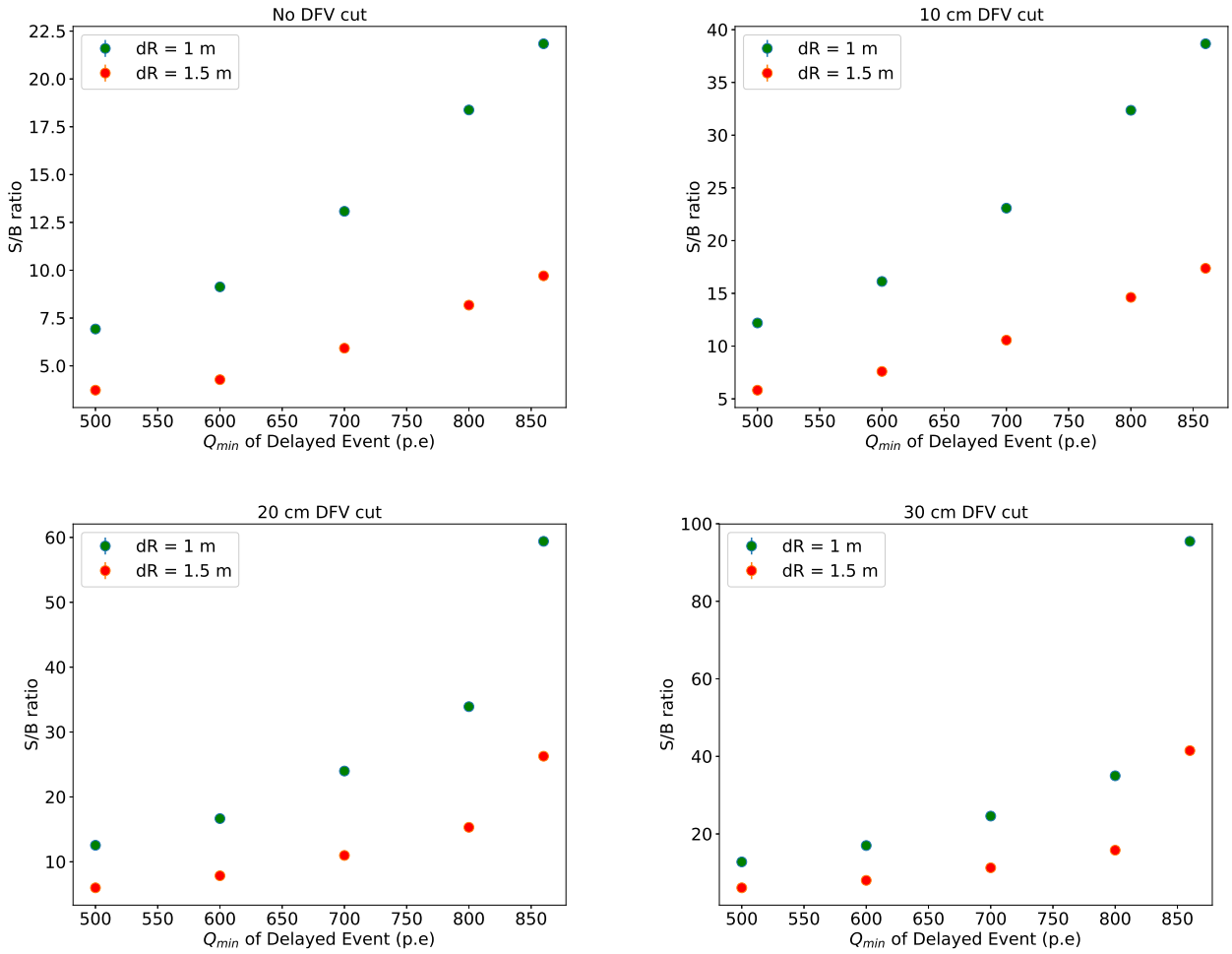

Figure 6.2.1: Signal-to-Background Ratios for dR = 1 m (green) and 1.5 m (red) for different DFV cuts as a function of Q_{min} of delayed.

This study was also done with different DFV cuts and different Q_{min} of delayed to check if there was any correlation. From Figure 6.2.1, it can be observed that the S/B for dR = 1.5 m is always half or less than half of the S/B for dR = 1 m, independent of the DFV cut and Q_{min} of delayed. In the next step, the S/B ratio was studied and sensitivity studies were performed for dR = 1 m to 1.5 m after deciding the DFV cut and Q_{min} of delayed which is discussed in Section 6.5.

The S/B ratio increased by a factor of approximately 1.2 for every 10 cm. The uncertainty from sensitivity studies indicated the lowest uncertainty for dR = 1.4 m and the next lowest for dR = 1.1 m. Considering the S/B ratios, a dR cut of 1.1 m was chosen (Figure 6.2.2).

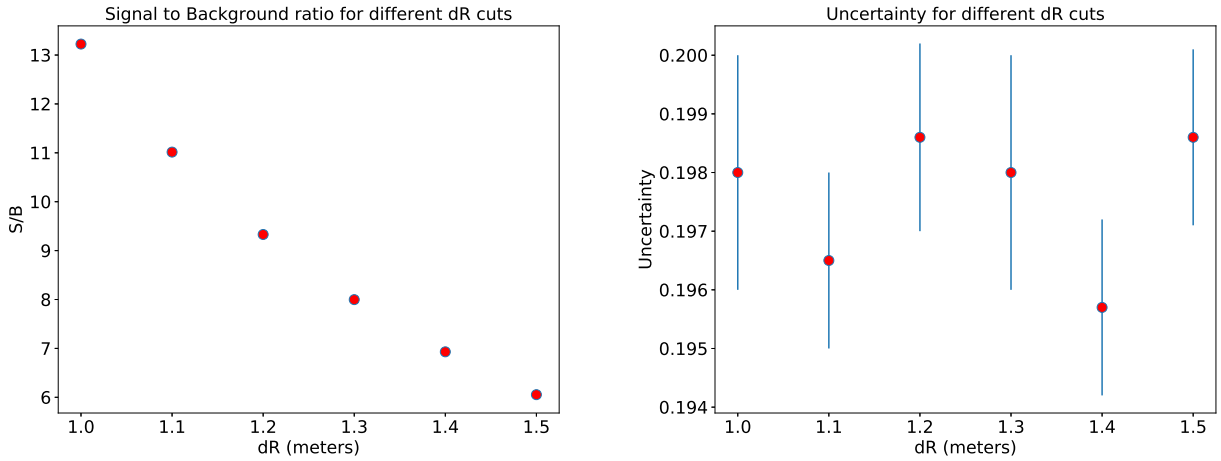

(a) (b)

Figure 6.2.2: Signal to background Ratio (a) and uncertainty (b) for different dR values for the optimised selection cuts.

One additional candidate with the optimised cuts was found when increasing the dR from 1 to 1.1 m. Increasing dR to 1.1 m led to an increase of 0.9% in the efficiency with a 0.1% improvement in precision as discussed in Sections 6.6.3 and 6.6.4.

6.2.2 Time Difference between Prompt and Delayed (dt) Events

The cut for the time difference between the prompt and delayed events can be implemented using the neutron capture time. This neutron capture time was calculated from the ^{241}Am-^{9}Be calibration data to be (254.5 ± 1.5) μs, as explained in Section 2.3. The lower end of the time window was increased to 20 μs after taking into account the 16 μs Data Aquisitiion (DAQ) window of Borexino which is followed by an electronics dead time of 3- 4 μs. It was also made sure that the delayed event was not very close to the start of the DAQ window (dt = 20 μs). Thus, during the previous analysis, the time difference between the prompt and delayed (dt) events was required to be between 20 and 1280 μs, i.e. five times the neutron capture time.

Double cluster events In the new analysis, the 0-20 μs time window was additionally studied. Double cluster events can be defined as those events where the prompt and the delayed signal fall within the same DAQ window as shown in Figure 6.2.3 (c). The reactor MC spectra was used for the detailed study of clusters. In order to take into account the effect of electronics, dt_{min} was decided according to the cluster duration and dt_{max} was decided using the variation of the cluster start time in the DAQ window.

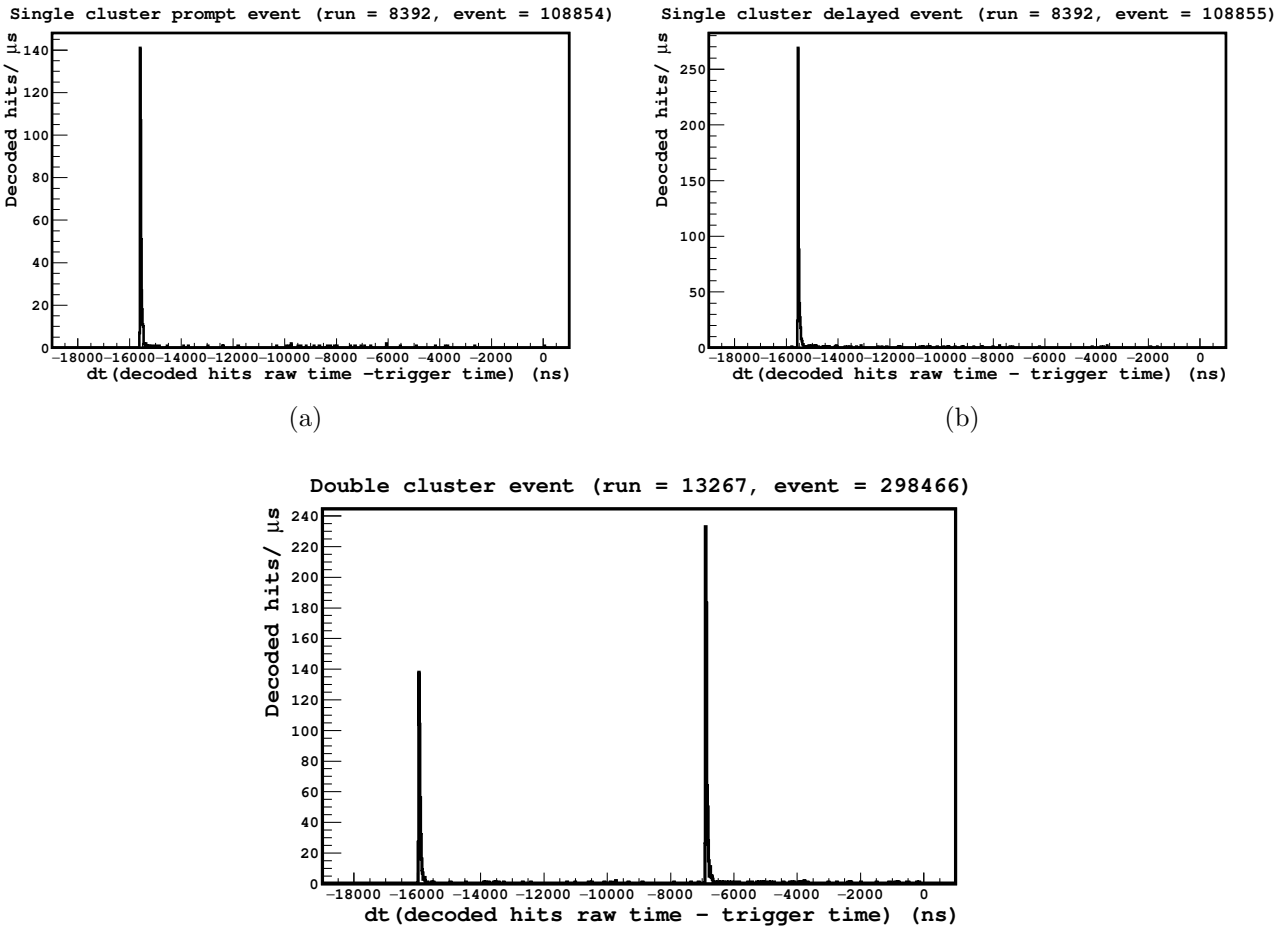

(a) (b)

(c)

Figure 6.2.3: Representation of single cluster prompt and delayed events ((a) and (b)) with a dt = 116.8 μs and double cluster event (c) with a dt of 9.1 μs in the 16 μs DAQ time window of Borexino.

The cluster duration of events in Borexino is not truncated for all events (Section 8.1). This is not a problem for low energy events, but for high energy events, the duration can be greater than 1.5 μs, a cut applied for majority of the events. In order to allow enough cluster duration for the prompt event and to avoid the overlap of prompt and delayed events, the simulated reactor antineutrino spectrum was studied (Figure 6.2.4 (a)) since the energy spectrum of reactor antineutrinos extends up to 8-10 MeV. Double cluster events with dt $<$ 2.5 μs were disregarded since the maximal cluster duration was found to be 2.5 μs. The cluster start time in the DAQ window was studied for a 6h run (Figure 6.2.4 (b)) and in order to make sure the delayed event was not very close to the end of the DAQ window, the upper limit on dt was set to 12.5 μs. This way the delayed event can have enough cluster duration of 2.5 μs even at the end of the DAQ gate.
The additional number of events expected from including double cluster events can be calculated as [exp(-2.5/254.5) - exp(-12.5/254.5)] = (3.8 $\pm$ 0.03)%. After taking into account that there are 91.8% of events present in the time window [20, 1280] μs, gives an expectation of 6 $\pm$ 2 candidates. The number of double cluster events found after all the optimised cuts are 8 which lies within the expectation. The increase in efficiency led to an improvement of 0.6% in the precision of measurement as discussed in Section 6.6.4.

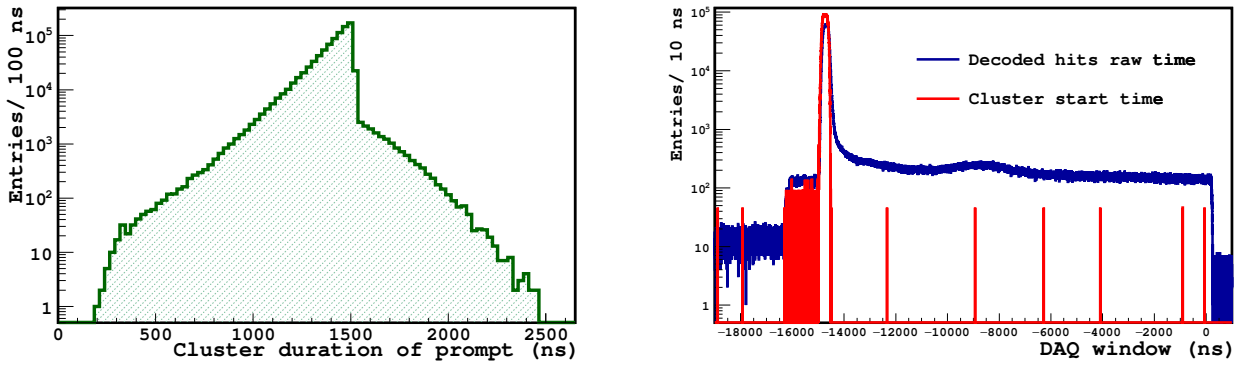

(a) (b)

Figure 6.2.4: (a) Cluster duration of simulated reactor antineutrinos. (b) Cluster start time of point like events compared with the decoded hits distribution in the DAQ window fr a 6 h run.

6.3 α/β Discrimination

6.3.1 Gatti Parameter

The gatti optimal filter is a linear discrimination technique which allows to separate two classes of events with different time shapes. The distinction is based on the fact that the time distribution of scintillation photons depends on the details of energy loss and it is very different for α and β particles. α particles have higher energy loss in the PC inside the liquid scintillator due to their higher charge and mass. The mean time of the hit times in the cluster or a "tail to total" (i.e. the fraction of hits in the tail of the time distribution with respect to the total number of hits in the clusters) are different for the two classes. In Borexino, this technique was developed using the ^{214}Bi-^{214}Po coincidence sample as typical β and α samples used to define the weights $w(t_n)$ in the equation (6.3.1). The gatti parameter G is defined as [14]

$$G = \sum_n f(t_n) w(t_n), \quad \text{where } w(t_n) \equiv \frac{P_\alpha(t_n) - P_\beta(t_n)}{P_\alpha(t_n) + P_\beta(t_n)}, \tag{6.3.1}$$

where $P_\alpha(t)$ and $P_\beta(t)$ are the probabilities that a photoelectron is detected at the time between t and $t + dt$ for α and β events respectively. t_n is the time of flight subtracted time profile of the studied events. Figure 6.3.1 shows the α/β distinction in Borexino done using the above mentioned method. The gatti limit for the delayed IBD candidate was set using ^{241}Am-^{9}Be calibration data and cross- checked with the Monte-Carlo (MC) simulated sample. All the β-like events simulated had a gatti value < 0.015.

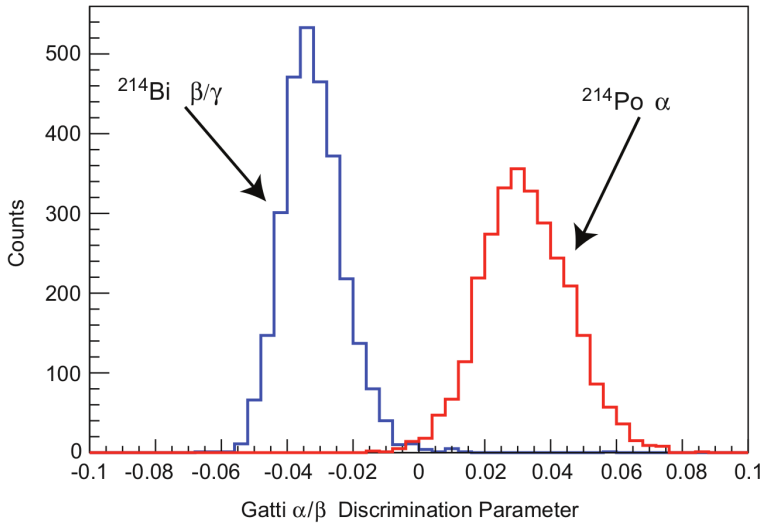

Figure 6.3.1: Gatti distinction of α and β particles in Borexino done using ^{214}Bi-^{214}Po sample [18].

6.3.2 Multi Layer Perceptron (MLP)

The Multi Layer Perceptron is a non-linear and different technique developed for α/β discrimination. It was developed using deep learning method for supervising binary classifiers i.e. functions that can decide whether an input (represented by vector of numbers) belongs to one class or another. This method uses many variables as inputs like different tails to totals, mean time of the hits in the cluster, kurtosis, variance, skewness and so on. The neural network is trained on two different samples (^{214}Bi-^{214}Po samples). The α-like events tend to have an MLP value of 0 while the β-like events tend to have an MLP value of 1. Figure 6.3.2 shows α/β distinction in Borexino using MLP.

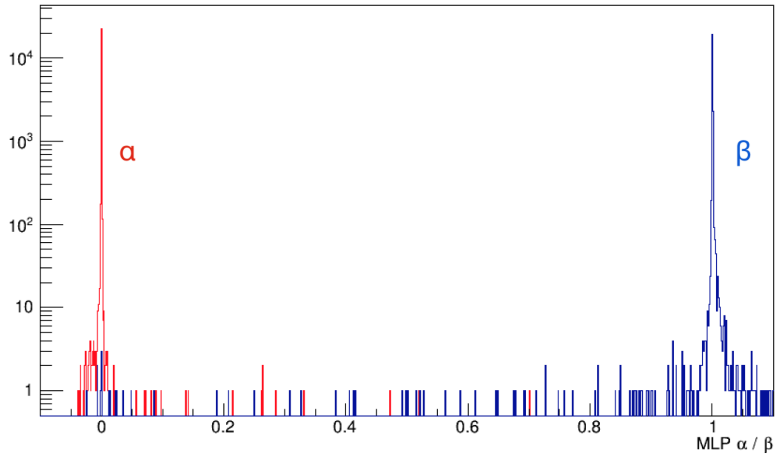

Figure 6.3.2: MLP distinction of α and β particles in Borexino done using ^{214}Bi-^{214}Po sample [6].

6.3.3 Gatti vs MLP

The study of MLP distribution of the geoneutrino candidate sample without any DFV or dt cuts shown in Figure 6.3.3 (a) indicated that there were a few candidates which had α-like MLP even though the gatti values were β-like (< 0.015). There were 5 such candidates and 4 of them were during the Water Extraction (WE) cycles, i.e. runs 13409-16503. 3 out of the 4 candidates from the WE period were not included in the 2015 analysis since they were either double cluster events or were less than 30 cm from the IV . This supports that these were actually background events and MLP seems to work better than Gatti during water extraction (WE) cycles. This can

also be seen from the higher concentration of events during WE, especially near the gatti value of 0.015 (geoneutrino selection) in Figure 6.3.3 (b). This distribution is to be compared to the MLP distribution in Figure 6.3.3 (c), where the distinction between α and β like events is better during WE period. Further, the energy cuts used for candidate selection are also dependent on Gatti/MLP, which is discussed in the next Section 6.4.

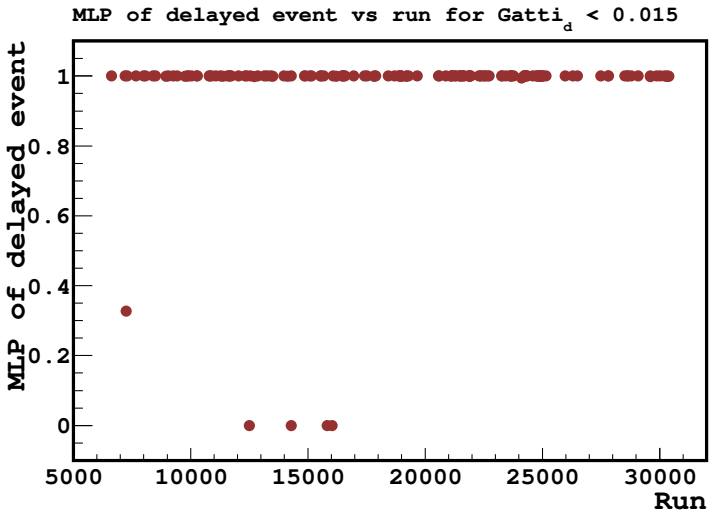

(a)

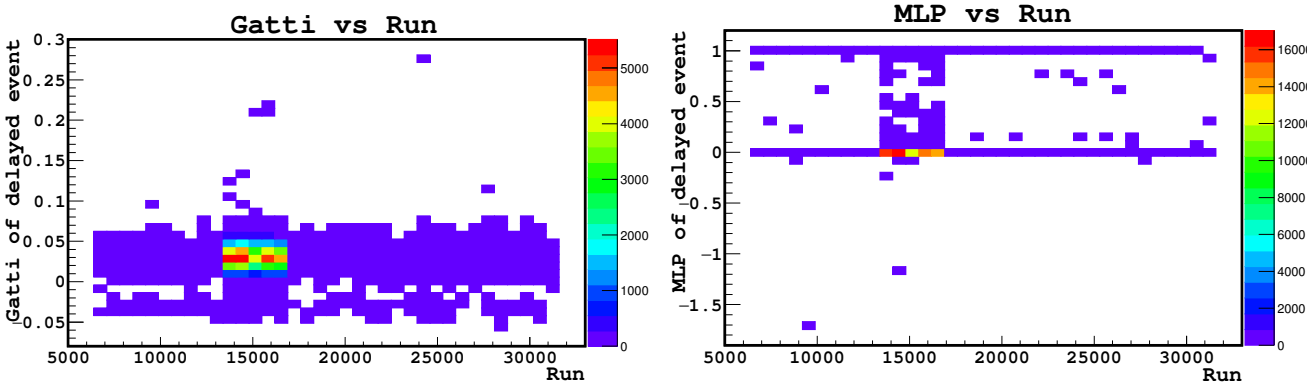

(b) (c)

Figure 6.3.3: (a) MLP distribution of delayed vs run for standard selection cuts without any DFV and dt cuts for the delayed events passing the old gatti cut used in [7]. (b) and (c) represent the gatti and MLP distributions of delayed event vs run for charge > 400 p.e for both prompt and delayed events, dt < 1280 μs, dR < 1 m and no DFV cut.

6.3.4 Study of MLP on ^{241}Am-^{9}Be Calibration Data

The MLP threshold for the delayed candidate used in the current analysis was set by observing the ^{241}Am-^{9}Be calibration data for source placed at the center, z = +4 meters from the center and z = -4 meters from the center after subtracting the accidentals (Figure 6.3.4). The MLP cut could not be decided using MC as it is was not simulated properly. Most events for source placed at the center have an MLP value > 0.9 while for the other positions a value of 0.8 seemed reasonable. The MLP threshold was set to 0.8 since less than 0.2% of the total number of events lie below 0.8 when combining all three positions.

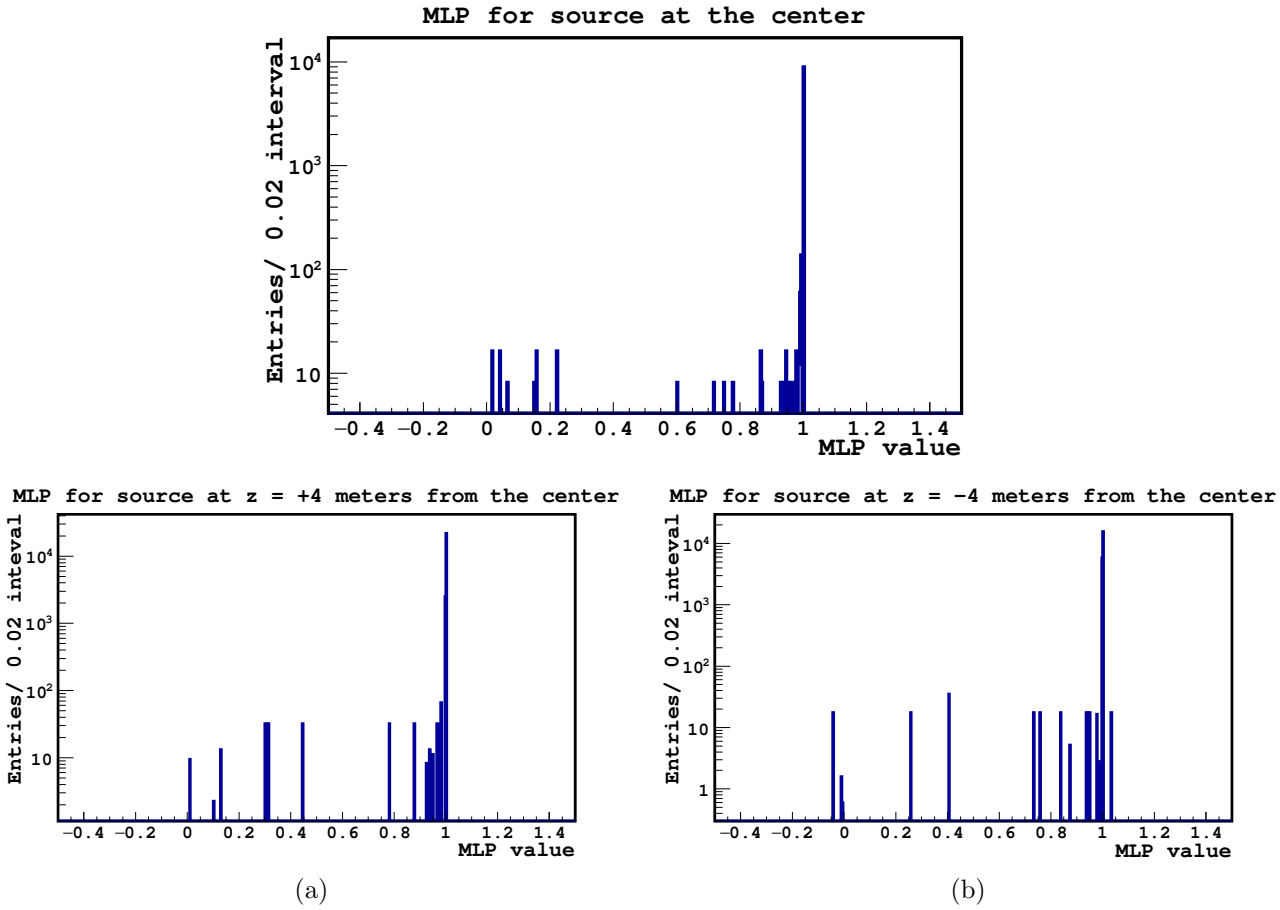

(a) (b)

Figure 6.3.4: MLP Distribution of the delayed event for the ^{241}Am-^{9}Be calibration data for the source placed at three different positions after subtracting the accidentals.

6.4 Energy Cuts

The energy cuts applied on the prompt and delayed events aid the identification of the IBD signals. The logic behind the energy cuts in the previous and current analyses is explained in the next two subsections.

6.4.1 Energy of Prompt Event

For all the geoneutrino analyses done with Borexino, the threshold for the prompt energy was fixed at 408 p.e. (≈0.8 MeV) after correcting for the energy resolution without any upper limit on the charge. This threshold is kept at 408 p.e. for the current analysis considering the IBD kinematic threshold of 1.8 MeV. During the period Feb 2010 - Jul 2011, data in Borexino was acquired with low threshold on all channels 1 of all laben boards. Therefore, these runs were reprocessed without the channels 1 to obtain the right prompt energy [26].

6.4.2 Energy of Delayed Event

The Q_{min} of delayed event corresponding to the 2.2 MeV gammas is 1100 p.e. In order to include the energy resolution and also neutrons that partially deposit energy in the buffer, the threshold was decreased to 700 p.e. in the 2010 analysis [19]. This was increased to 860 p.e. in 2013 to remove additional background events during the WE cycles where the gatti parameter did not work well below 860 p.e due to Rn contamination. (Figure 6.4.1).

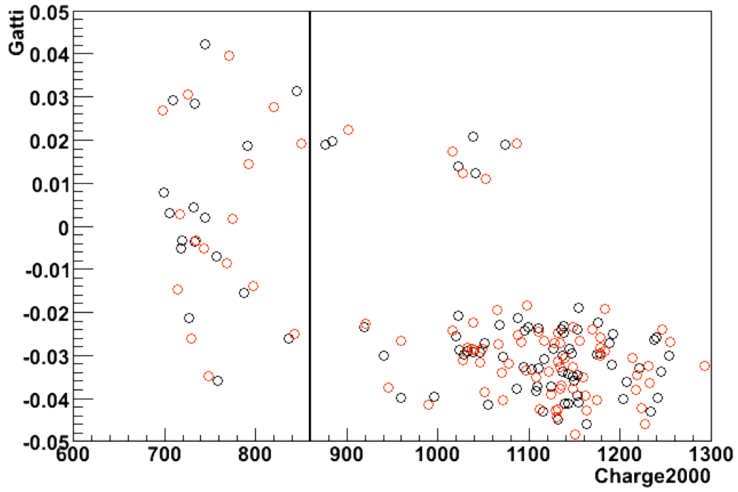

Figure 6.4.1: Gatti vs Normalized Q_{min} for delayed candidates without any DFV cut before (black) and after (red) reprocessing without channels 1. This analysis was done for the paper published in 2013 [17].

When studying the Gatti and MLP distributions for the optimised cuts, it was found that there is a possibility of reducing the Q_{min} of delayed event if MLP is used (Figure 6.4.2). In case of MLP, background discrimination looked better even at charges as low as 600 p.e. As there was increased level of backgrounds during the WE cycles [41], it was decided to keep the Q_{min} at 860 p.e. (for runs 13409-16503) to reduce Rn related backgrounds. It was important to study the effect of Q_{min} of delayed along with different DFV cuts as they are highly correlated. The combination of S/B ratio and uncertainty value looked reasonable for 700 p.e. after deciding upon the DFV cut of 10 cm which is discussed in the next section. Hence, the Q_{min} of delayed was reduced to 700 p.e. for all runs excluding the WE cycles.

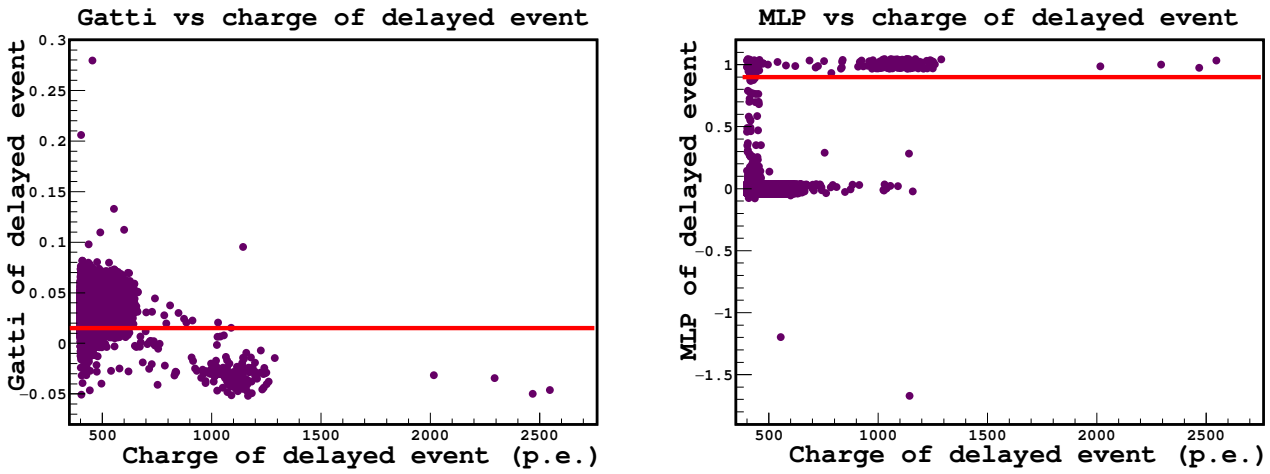

(a) (b)

Figure 6.4.2: Gatti (a) and MLP (b) distributions vs charge for delayed events. β-like interactions lie at gatti < 0.015 or MLP > 0.8.

The p-capture of neutrons emit 2.2 MeV gammas, thus the Q_{max} of delayed was kept at 1300 p.e (2.6 MeV) until 2015. In order to include the neutron capture on ^{12}C in the scintillator (Figure 6.4.3), the Q_{max} of delayed was increased to 3000 p.e. ($\approx$5.5 MeV). This increased the efficiency by 2.17% for the optimised cuts and 3 candidates were found when the expectation was 3 ± 2 candidates. The increase in efficiency led to an improvement of 0.4% in precision as discussed in Section 6.6.4.

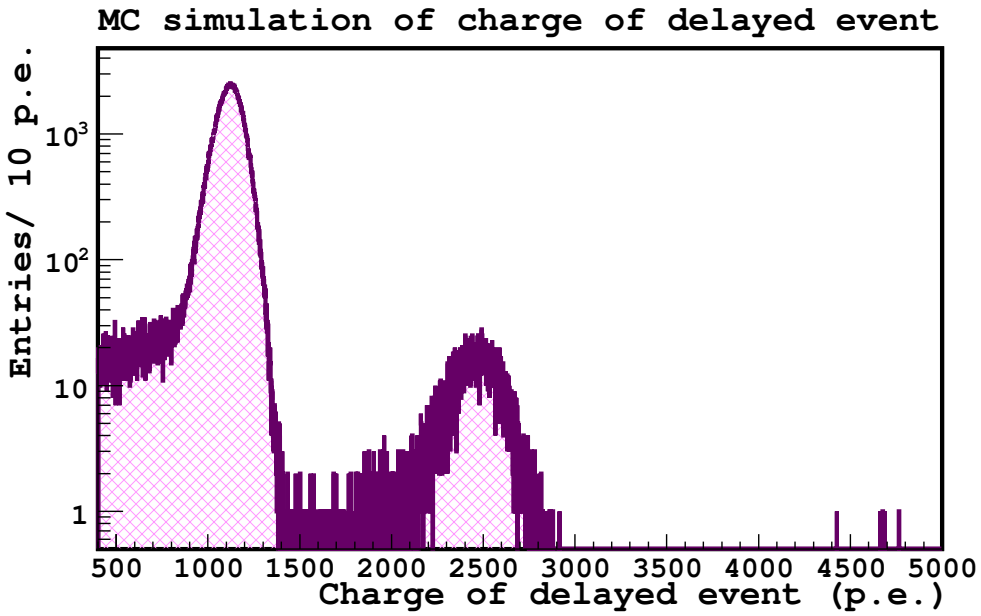

Figure 6.4.3: MC simulated charge of delayed for geoneutrinos with a threshold of 400 p.e.

6.5 Dynamical Fiducial Volume (DFV)

6.5.1 Borexino Vessel Shape

The Borexino (IV) shape keeps changing with time and requires regular monitoring and reconstruction. A leak of the scintillator from the IV to the buffer region within the OV started approximately in 2008. The small leak in the IV was reconstructed to have a location of $27^0 < \theta < 37^0$ and $225^0 < \phi < 270^0$. The leak was detected based on the large amount of events reconstructed outside the IV. In order to minimize the leak rate, the density difference between the scintillator and the buffer liquids was reduced by partial removal of DMP from the buffer by distillation, with negligible consequences on the buffer's optical behavior. Due to the presence of hole and buoyancy effects, the IV profile is not precisely spherical. Its shape is determined dynamically by identifying background events present on the vessel surface. The position of these events is fitted assuming uniformity on x-y planes so that the z-dependence of the vessel radius can be determined.

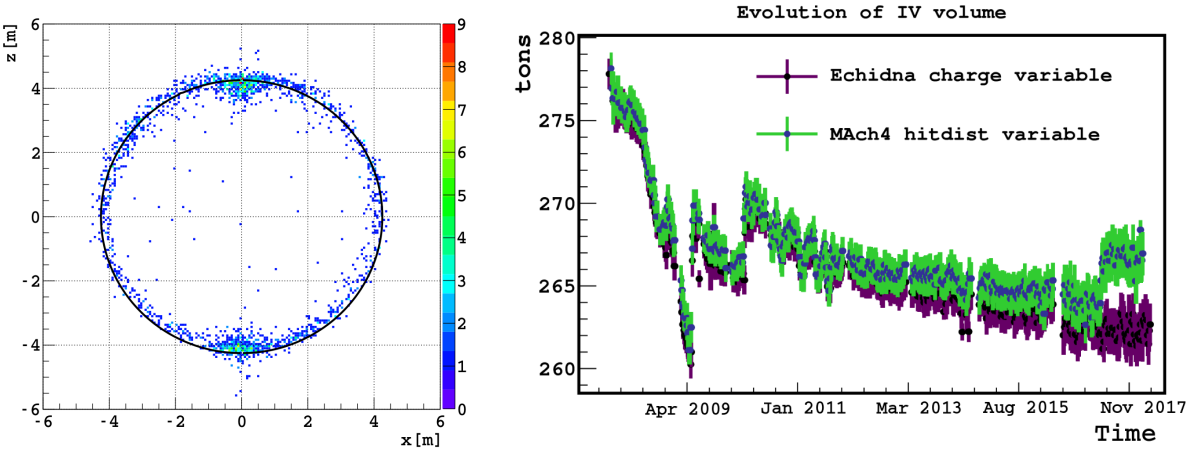

(a) (b)

Figure 6.5.1: (a) Distribution of events in the range 290-350 p.e. [36] (b) Evolution of the volume of IV over the years for the vessel shape reconstructed with the Mach4 variable and Echidna variable.

The official position reconstruction algorithm [36] exploits the abundance of possibly ^{210}Bi on the IV (Figure 6.5.1 (a)). The selection of these events is done with the use of Mach4 hitdist variable between 290-350 p.e. (also called the "Bismuth Valley"). In May 2018, it was found that recabling of channels done during April 2017 caused a sudden jump in the volume which was caused due to a problem in the used variable. Therefore, the vessel shapes for all data were reprocessed with the use of Echidna charge variable used for geoneutrino candidate selection. After the use of the Echidna charge variable, no jump was observed in the volume after recabling. The function used to fit the vessel shape within the (r, θ) distribution of selected events is defined as:

$$R_{shape}(r,\theta) = N_0(\theta)exp[\frac{(r-\mu(\theta))^2}{\sigma^2(\theta)}] + \sum_{i=1}^{2} G_i(r,\theta), \tag{6.5.1}$$

where r and θ are positions of each event on histogram plane, $N_0(\theta)$ is normalization factor defined as a 3rd degree polynomial of θ, $G_i(r,\theta)$ are two bidimensional Gaussian functions, $\sigma(\theta)$ is a linear function of θ.
The same fit function can also be used to fit the ^{14}C events that define the vessel shape [47] as shown in Figure 6.5.2 (a). Single cluster events with nhits value less than 130 are used for this reconstruction method. The differences in position that might arise due to these two methods can be used to calculate the systematic uncertainty in position as explained in Section 7.4.

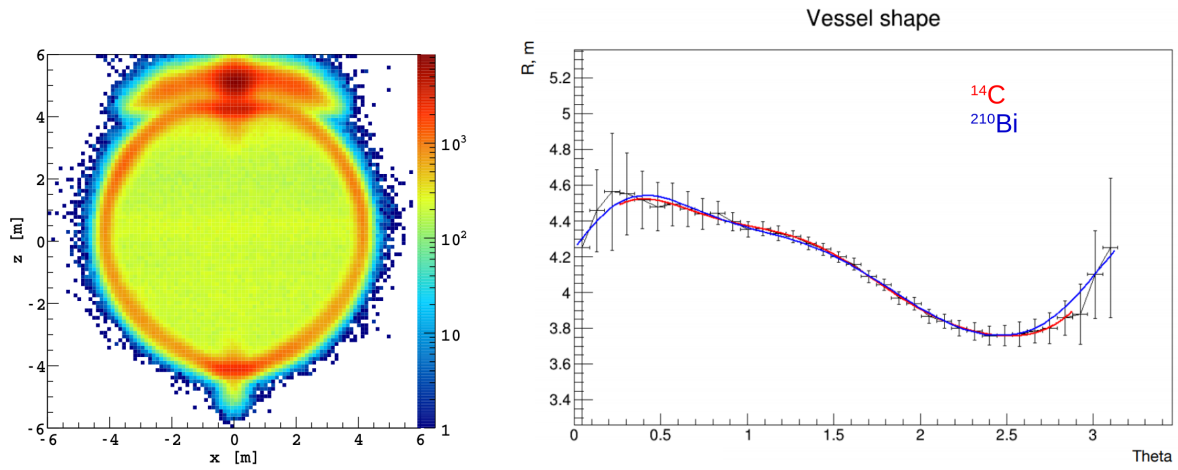

(a) (b)

Figure 6.5.2: (a) Distribution of ^{14}C in the vessel [36]. (b) Comparison of 2D histogram r vs θ for one week using the two methods [47].

6.5.2 Comparison of MC and Data

The radial distribution of the selected IBD candidates was compared with MC for different DFV cuts, keeping the other optimised selection cuts in order to see if there was any excess of events at larger radii. Data and MC agree well as shown in Figure 6.5.3. A slight excess of events seen without any DFV cut disappears after a the 10 cm DFV cut.

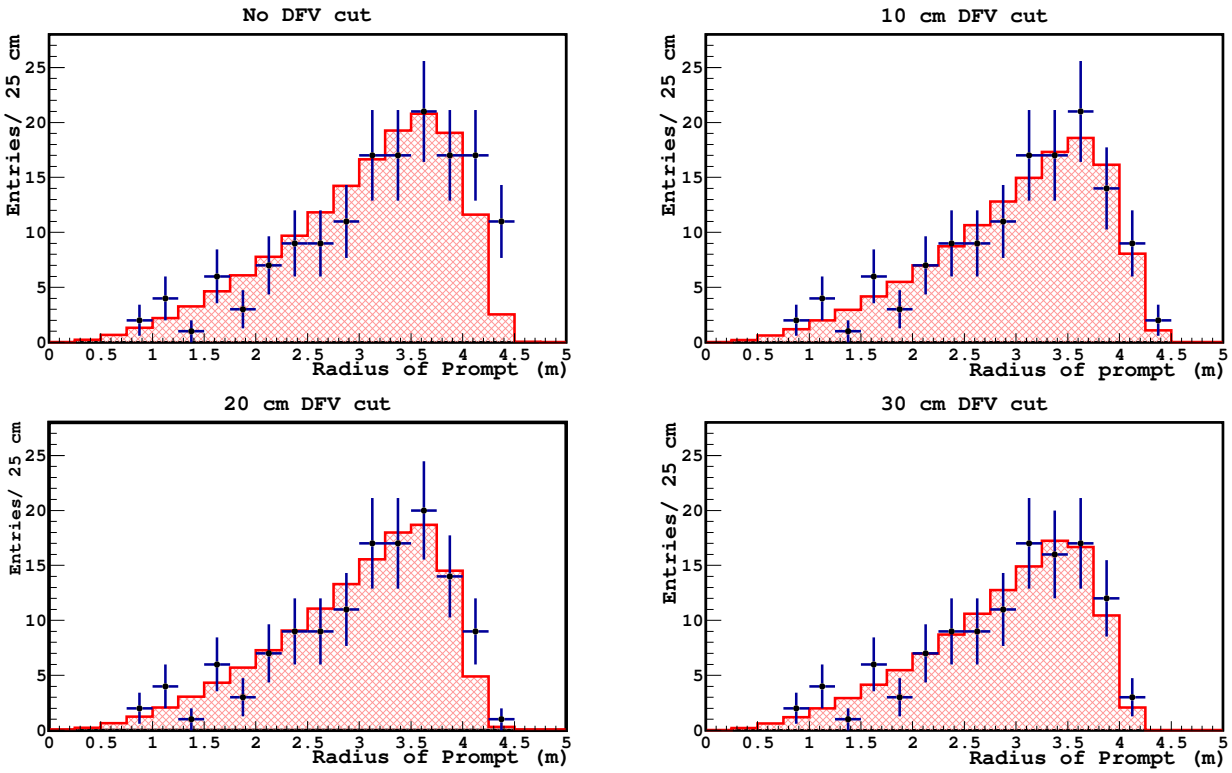

Figure 6.5.3: Comparison of radial distribution of prompt IBD events in data (blue) and geoneutrino MC (red) for different DFV cuts.

The first set of sensitivity studies was performed for different combinations of DFV cuts and the Q_{min} of delayed event. The sudden drop in the uncertainty for DFV cut of 20 cm to 10 cm as shown in Figure 6.5.4 (a) and the good S/B ratio for Q_{min} of delayed event at 700 p.e. shown in Figure 6.5.4 (b) favored the decision of choosing a DFV cut of 10 cm and the charge threshold of 700 p.e. for the delayed event.

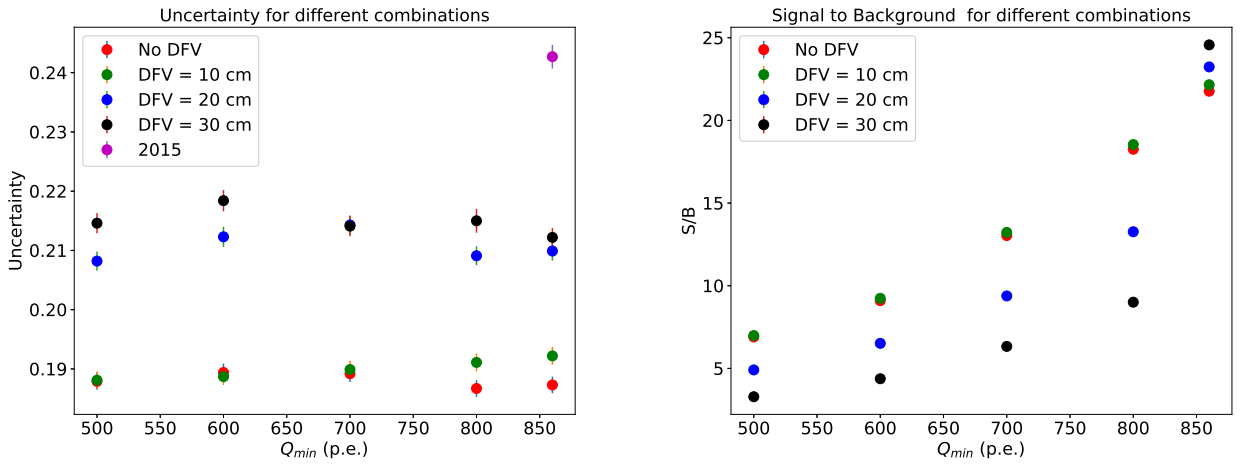

(a) (b)

Figure 6.5.4: Uncertainty values (a) and S/B ratio (b) for the different DFV cuts as a function of Q_{min} of delayed.

The uncertainty does not vary much for both no DFV cut and a DFV cut of 10 cm for Q_{min} cut in the [500,700] p.e. range. In addition, efficiency drop for no DFV cut (Section 6.6.3) proved that applying a 10 cm DFV cut is a safe way to reject background events and also reduce

the uncertainty of the measurement. This combination led to an improvement of 0.9% in the precision of the measurement. The change of DFV cut from 30 cm to 10 cm led to a 15% increase in the exposure and lowering the Q_{min} of delayed increased the efficiency by 1.1% and a 1.4% improvement in precision. These are discussed in Sections 6.6.3 and 6.6.4.

6.6 Influence of Selection Cuts

6.6.1 Comparison of Standard and Optimised Selection Cuts

The comparison of all the standard selection cuts used in the 2105 analysis [7] and the optimised selection cuts done for this work are listed in Table 6.6.1.

Selection Cut	**2015 [7]**	**This work**
Energy of prompt event	$>$ 408 p.e.	$>$ 408 p.e.
Energy of delayed event	860 - 1300 p.e.	700 - 3000 p.e. and 860 - 3000 p.e (WE)
dt (prompt-delayed)	20-1280 μs	2.5-12.5 μs and 20-1280 μs
dR (prompt-delayed)	1 m	1.1 m
Muon vetoes	2 s dead time for internal muons	2 s, 1.6 s, 2 ms dead times for different kinds of internal muons
	2 ms dead time for external muons	2 ms dead time for external muons
	Independent check of FADC muons	Combined FADC and Laben Analysis
DFV cut	Distance of prompt event from IV $>$ 30 cm	Distance of prompt event from IV $>$ 10 cm
α/β Discrimination	$\text{gatti}_d < 0.015$	$\text{MLP}_d > 0.8$
Multiplicity cut	Check for high energy events 2 ms before prompt, between prompt and delayed, and 2 ms after delayed	Check for high energy events 2 ms before prompt, between prompt and delayed, and 2 ms after delayed

Table 6.6.1: Comparison of the selection cuts used for the previously published results [7] and the optimised cuts done for this work.

6.6.2 Influence on Backgrounds

^{9}Li-^{8}He and ^{12}B background The number of IBD-like signals found 2 s after internal muons is 264 after all the optimised cuts. The decay time was estimated as 0.294 $\pm$ 0.023 s for the 288 candidates found without any DFV cut (Figure 6.6.1).

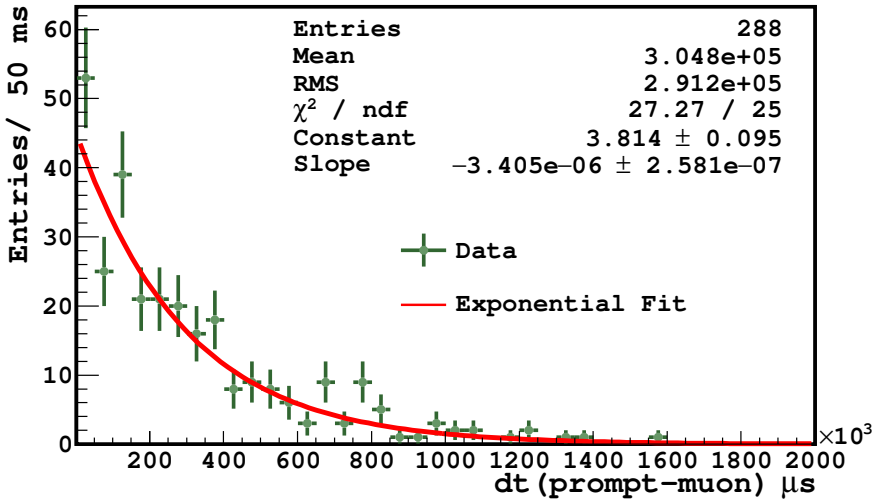

Figure 6.6.1: Distribution of absolute time difference between the prompt event and muon (dt (prompt-muon)) for the 288 hadronic candidates imitating IBD found after optimised cuts and without any DFV cut.

Due to the different kind of muon vetoes, it is important to estimate the amount of hadronic background in the candidate sample for the 1.6 s and 2 s vetoes. There were 241 of candidates found within 2 s after the BTB 4 (μ + n) and the BTB 0 muons. Considering the time scope of the exponential fit in Figure 6.6.1, 99.21% of the candidates lie within the time window [2 ms, 2 s] and 0.1% remain after 2 s. Thus the background after 2 s due to these kind of muons can be calculated as 241*0.001/0.9921 = 0.243 ± 0.016 (stat.) $^{+0.22}_{-0.07}$ (syst.). The number of candidates found within 1.6 s of the BTB 4 (μ - n) with ≥8000 decoded hits was 23. 98.89% of the candidates lie in the time window [2 ms, 1.6 s] and 0.4% lie after 1.6 s using the method described in Section 4.2.1. Therefore, the background due to these kind of muons can be calculated as 23*0.004/0.9889 = 0.093 ± 0.019 (stat.) $^{+0.16}_{-0.02}$ (syst.). The total amount of hadronic background in the antineutrino candidate sample after all the optimised selection cuts can be given as:

$$\boxed{N_{\text{Li-He-B}} = 0.336^{+0.27}_{-0.08}}$$

Random Coincidences There were 29357 events found in the time window [2, 20] s for all the optimised selection cuts. Scaling these events to the time window [0, 1280] μs, we get 29537*0.001280/18 = 2.1 events in the geoneutrino candidate sample. After considering the suppression factor, as discussed in Section 4.3, the random coincidental background can be given as:

$$\boxed{N_{\text{random}} = 2.3 \pm 0.012(stat) \pm 0.0012(syst)}$$

The dt (prompt-delayed) distribution for the accidental background in the time window 2-20 s and the energy distribution of prompt events in the window 2 ms - 20 s is shown in Figure 6.6.2.

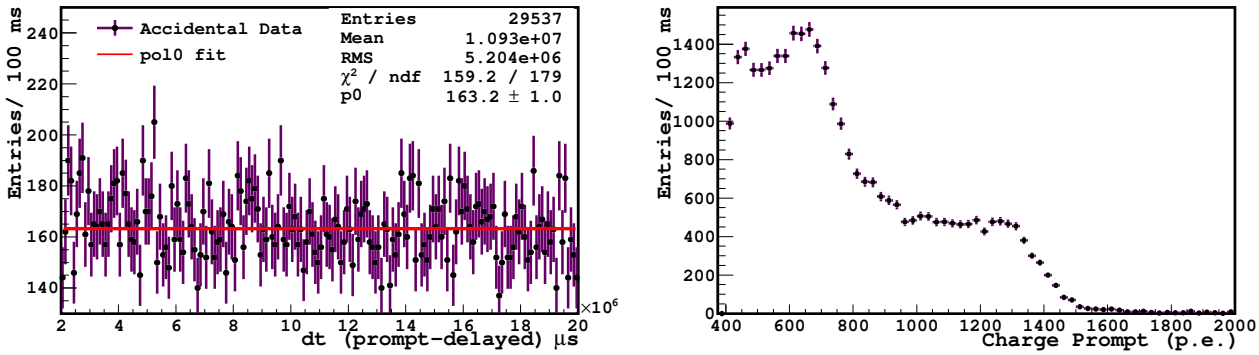

(a) (b)

Figure 6.6.2: (a) Distribution of absolute time difference between the prompt and delayed events (dt (prompt-delayed) for accidentals. (b) Energy distribution of prompt events of random coincidences.

Table 6.6.2 summarizes all the backgrounds with the optimised selection cuts. The hadronic background due to muons and the random coincidences were calculated independently as discussed in the previous subsections while the other backgrounds were scaled to the current exposure of 1671 ton·yr from the exposure 907 ton·yr reported in the paper published in 2015 [7]. The (α, n) background was evaluated using the ^{210}Po activity used in 2015.

Background	**2015 [7]**	**This work**
^{9}Li-^{8}He, ^{12}B	$0.194^{+0.125}_{-0.089}$	$0.336^{+0.27}_{-0.08}$
Random coincidences	Accidental background = 0.221 ± 0.004	2.3 ± 0.014
	Time correlated background = $0.035^{+0.029}_{-0.028}$	-
(α, n) in scintillator	0.165 ± 0.01	0.304 ± 0.02
(α, n) in buffer	<0.51	<0.938
(γ, n)	-	< 0.07
Fast n's (μ in WT)	<0.01	<0.02
Fast n's (μ in rock)	<0.43	<0.79
Untagged Muons	0.12 ± 0.01	0.22 ± 0.02
Fission in PMTs	0.032 ± 0.003	0.059 ± 0.006
^{214}Bi-^{214}Po	0.009 ± 0.013	0.009 ± 0.013
Total	$0.78^{+0.13}_{-0.10}$	$5.08^{+0.27}_{-0.09}$

Table 6.6.2: Comparison of backgrounds published in 2015 [7] with the backgrounds estimated for the current work with optimised selection cuts.

6.6.3 Influence on Efficiency

The MC efficiency was calculated as the average of the MC efficiencies of the simulated geoneutrinos and the reactor antineutrinos. MC efficiency is defined as,

$$\text{MC efficiency} = \frac{\text{No. of events passing the given selection cuts}}{\text{No . of events generated in a certain FV}} \tag{6.6.1}$$

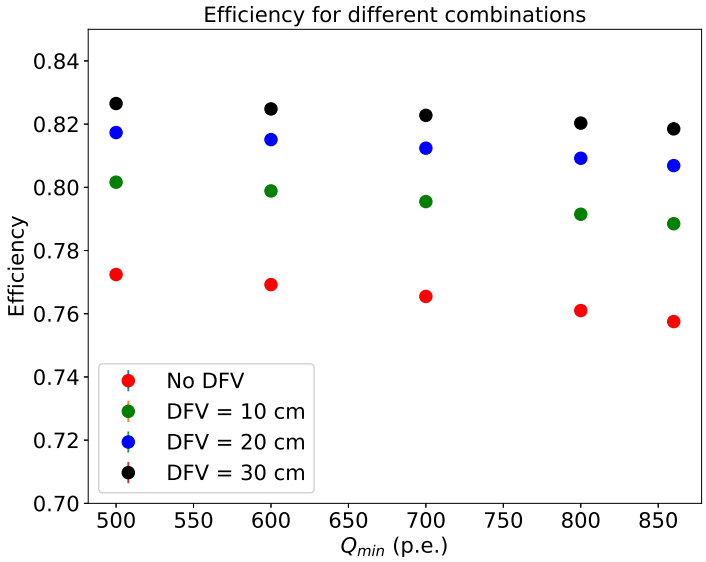

Figure 6.6.3: MC efficiency of different DFV cuts as a function of Q_{min} of delayed event.

The study of efficiency for different combinations of DFV cuts and Q_{min} of delayed event (Figure 6.6.3) proved that no matter the value of Q_{min} of delayed, the efficiency for no DFV cut was significantly lower than that for the other DFV cuts. The efficiency increase for every optimised selection cut is given in Table 6.6.3. The efficiency for the standard selection cuts was obtained as 82.3 ± 0.002% while the final efficiency obtained for all the optimised cuts was 87.1 ± 0.002%.

Selection Cut	**MC efficiency**
Standard selection cuts	82.3%
+ DFV = 10 cm + Q_{min} of delayed = 700 p.e.	80.2%
+ dR = 1.1 m	81.1%
+ Double cluster events	84.9%
+ ^{12}C capture of neutron	87.1%

Table 6.6.3: MC efficiencies for the optimised selection cuts.

The MC efficiencies for geoneutrinos from the ^{238}U and ^{232}Th chains were calculated as 82.8% and 79% respectively for the standard selection cuts with updated statistics and 87.6% and 83.6% respectively for the optimised selection cuts. This was done by scaling the number of prompt events above the 408 p.e. threshold in the MC simulated sample of all geoneutrinos, geoneutrinos coming the ^{238}U chain and geoneutrinos coming from the ^{232}Th chain.

6.6.4 Expected Precision from Sensitivity

The expected uncertainty from only the updated statistics, keeping the standard selection cuts obtained using the sensitivity tool is 21.2 ± 0.2% while the expected uncertainty after all the optimised selection cuts is 18.89 ± 0.14% (Figure 6.6.4). The improvement in precision for just the updated statistics is 3.1% when compared to 2015 (Figure 5.4.1) and the additional improvement in precision due to the optimised cuts is around 2.9%.

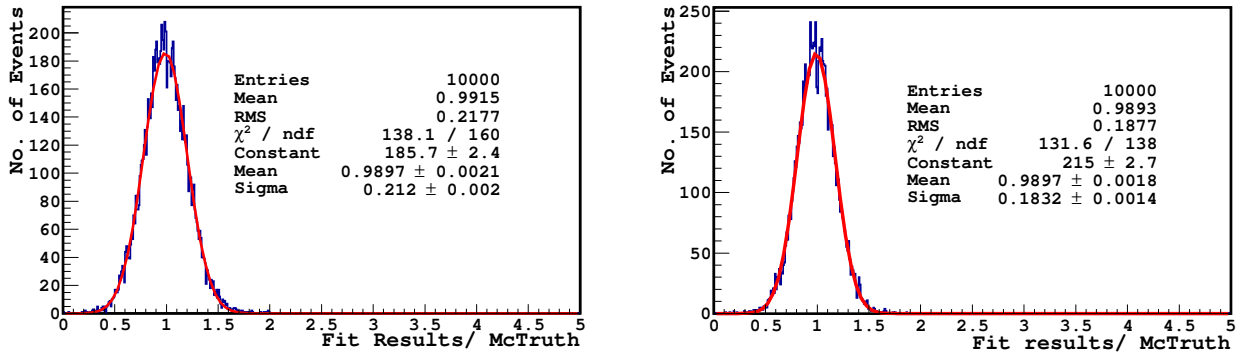

(a) (b)

Figure 6.6.4: Gaussian fits for FitResults/McTruth ratios for updated statistics with standard selection cuts (a) and optimised selection cuts (b).

The improvement in the precision of every optimised cut obtained using the sensitivity tool is listed in Table 6.6.4.

Selection cut	**Uncertainty from sensitivity**
2015	24.27 ± 0.19%
+ Updated statistics	21.2 ± 0.2%
+ DFV = 10 cm + Q_{min} of delayed= 700 p.e.	19.8 ± 0.2%
+ dR = 1.1 m	19.65 ± 0.15%
+ Double cluster Events	19.3 ± 0.2%
+ ^{12}C capture of neutron	18.89 ± 0.15%
+ New muon vetoes	18.32 ± 0.14%

Table 6.6.4: Expected uncertainty from the sensitivity studies for different optimised selection cuts.

6.6.5 Golden Candidates

The exposure, the number of antineutrino candidates, increase in number of candidates and the expected increase for every optimised cut are given in Table 6.6.5. The latter is calculated by scaling the exposure. The exposure is calculated using the density of the scintillator 0.8803 kg/m^3 as follows:

$$\boxed{\text{Exposure} = (\text{livetime - deadtime}) * \text{volume} * \text{density of the scintillator} * \text{MC efficiency}} \quad (6.6.2)$$

Selection Cut	**Exposure ton·yr**	**No. of candidates found**	**Difference in no. of candidates**	**Expected Increase**
2015 [7]	907	77	-	-
+ Updated statistics	1271	102	25	31 ± 6
+ DFV cut = 10 cm	1418	115	13	12 ± 3
+ Q_{min} of delayed =700 p.e.	1433	117	2	1 ± 1
+ New muon vetoes	1539	123	6	7 ± 3
+ Double cluster events	1612	130	7	5 ± 2
+ ^{12}C capture of neutron	1654	132	2	2 ± 1
+ dR = 1.1 m	1671	133	1	1 ± 1
+ $MLP_d > 0.8$	1671	131	-2	-

Table 6.6.5: Antineutrino candidates and the corresponding exposure for each optimised selection cut.

The final exposure of 1671 ton·yr is almost double the exposure of 907 ton·yr published in [7]. The expected number of candidates is 142 ± 12 when a gatti cut is used on the delayed event and 138 ± 12 when an MLP cut is used on the delayed. The total number of candidates found for gatti and MLP cut are 133 and 131 respectively, both of which lie within the expectation as seen in Table 6.6.5.

7 Final Results

7.1 Results with Updated Statistics

The two kinds of likelihood fit as explained in Section 5.2 were performed for the 102 candidates obtained from the increased statistics and standard selection cuts with a corresponding livetime of 2647 days and exposure of 1271 ton·yr.

U/Th fixed to chondritic ratio The results obtained for the updated statistics from fixing the U/Th ratio to the chondritic value, shown in Figure 7.1.1 are $N_{geo} = 31.3 \pm 7.1$ events and $N_{rea} = 69.8 \pm 9.4$ events. This corresponds to a statistical uncertainty of 22.7% on the geoneutrino signal.

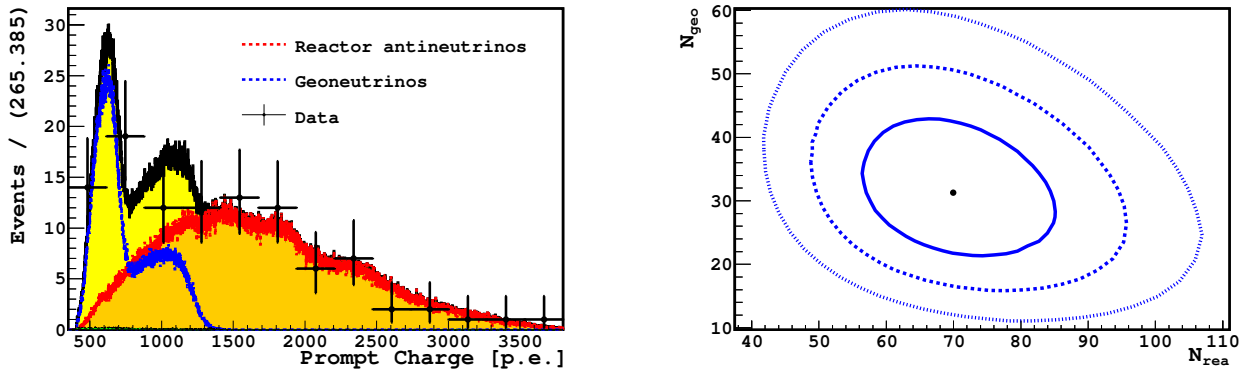

(a) (b)

Figure 7.1.1: (a) Likelihood fit and (b) 1σ, 2σ, and 3σ best-fit contours for N_{geo} and N_{rea} performed for the 102 candidates with U/Th fixed to the chondritic value.

U and Th free The results obtained by leaving the U and Th parameters free (Figure 7.1.2) are $N_U = 23.7 \pm 11.3$ events, $N_{Th} = 7.6 \pm 6.97$ events and $N_{rea} = 70 \pm 9.9$ events.

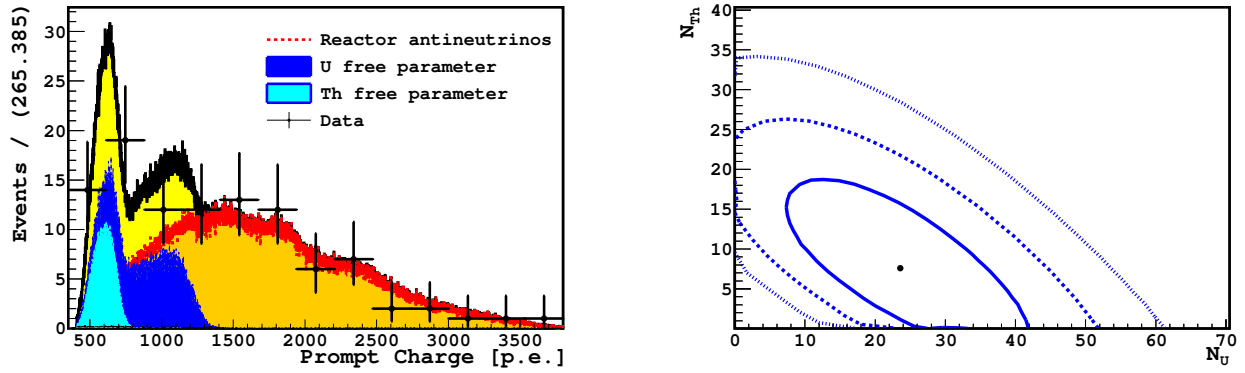

(a) (b)

Figure 7.1.2: (a) Likelihood fit and (b) 1σ, 2σ and 3σ best-fit contours performed for N_{Th} and N_U for the 102 candidates with U and Th as free fit parameters.

7.2 Results with Optimised Selection Cuts

The fits were performed for the 131 candidates obtained from the optimised cuts and increased statistics with a corresponding livetime of 2843 days and exposure of 1671 ton·yr. The results for every optimised cut are discussed in the next subsection.

U/Th fixed to chondritic ratio The obtained results (Figure 7.2.1) are $N_{geo} = 40.99 \pm 8$ events and $N_{rea} = 86.7 \pm 10.4$ events. This corresponds to a statistical uncertainty of 19.5% on the geoneutrino signal.

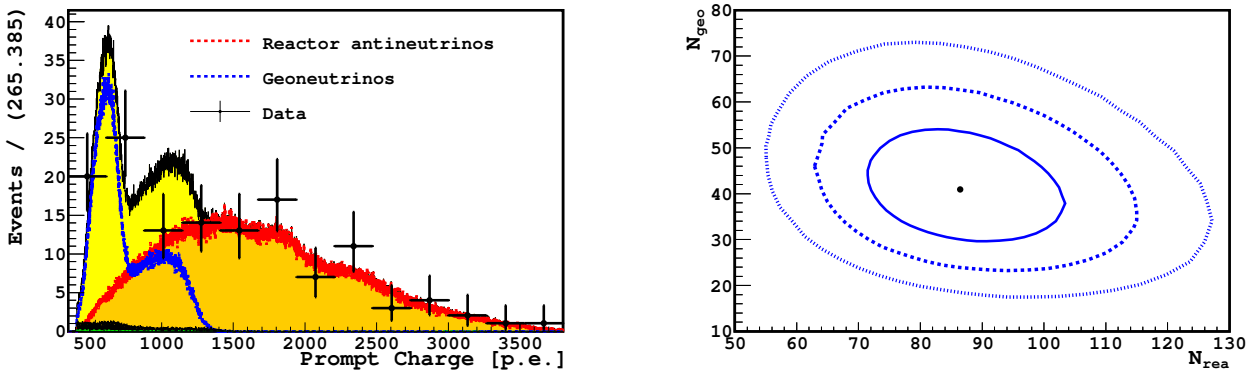

(a) (b)

Figure 7.2.1: (a) Likelihood fit and (b) 1σ, 2σ and 3σ best-fit contours for N_{geo} and N_{rea} performed for the 131 candidates with U/Th fixed to the chondritic value.

Free chondritic ratio The results obtained by leaving the U and Th parameters free (Figure 7.2.2) are $N_U = 19.7 \pm 12.2$ events, $N_{Th} = 17.8 \pm 8.1$ events and $N_{rea} = 90.3 \pm 11.2$ events.

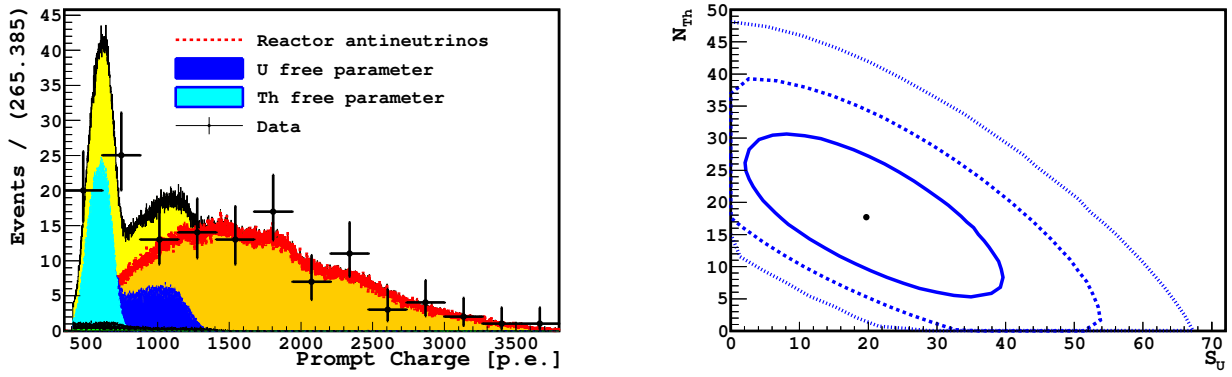

(a) (b)

Figure 7.2.2: (a) Likelihood fit and (b) 1σ, 2σ, and 3σ best-fit contours for N_{Th} and N_U performed for the 131 candidates with U and Th as free parameters.

7.3 Comparison of Statistical Uncertainties

The comparison of number of geoneutrino and reactor antineutrino events and their corresponding TNU values obtained from this work for different selection cuts are listed in Table 7.3.1

Selection	N_{geo} (events)	N_{rea} (events)	S_{geo} (TNU)	S_{rea} (TNU)	σ on S_{geo}
2015 statistics [7]	22.1 ± 5.8	49.2 ± 7.8	43.9 ± 11.2	97.8 ± 15.5	25.5% (with gatti)
	20.6 ± 5.6	49.1 ± 7.7	40.9 ± 11.1	97.5 ± 15.3	27.1% (with MLP)
+ Improved statistics	31.3 ± 7.1	69.8 ± 9.4	40.9 ± 9.3	91.3 ± 12.3	22.7%
+ DFV = 10 cm + Q_{min} delayed = 700 p.e.	37.3 ± 7.6	77.4 ± 9.8	43.3 ± 8.8	89.7 ± 11.4	20.4%
+ Double cluster events	43.1 ± 8	78.8 ± 9.9	47.7 ± 8.9	87.3 ± 11	18.5%
+ ^{12}C capture of neutron	43.3 ± 8.1	80.3 ± 10	46.7 ± 8.7	86.6 ± 10.8	18.7%
+ dR = 1.1 m	43.2 ± 8.1	80.2 ± 10	46.1 ± 8.7	85.6 ± 10.7	18.7%
+ New muon vetoes	42.7 ± 8.1	87 ± 10.4	42.5 ± 8.1	86.5 ± 10.3	18.9%
+ $MLP_d > 0.8$	41 ± 8	86.7 ± 10.4	40.7 ± 8	86.2 ± 10.3	19.5%

Table 7.3.1: Comparison of the number of geoneutrino and reactor antineutrino events and their corresponding signals in TNU for different selections obtained from this work.

The statistical uncertainty for the 2015 statistics [7] after using an MLP cut instead of the gatti cut is 27.14%. Thus, the increase of 0.6% in uncertainty in the last step in Table 7.3.1 after changing to MLP is consistent. The 6% improvement in the precision obtained on data is to be compared to the expected improvement of 6% from sensitivity studies as reported in Section 6.6.4.

7.4 Systematic Studies

Vessel shape and position reconstruction The average volume for a DFV cut of 10 cm is 257 ton [30]. The IV shape reconstruction induces systematic errors in the volume and also eventually the overall exposure and this needs to be studied. The maximum difference in the volume reconstructed using the official algorithm and the ^{12}C reconstruction algorithm over the entire period was around 0.8%.

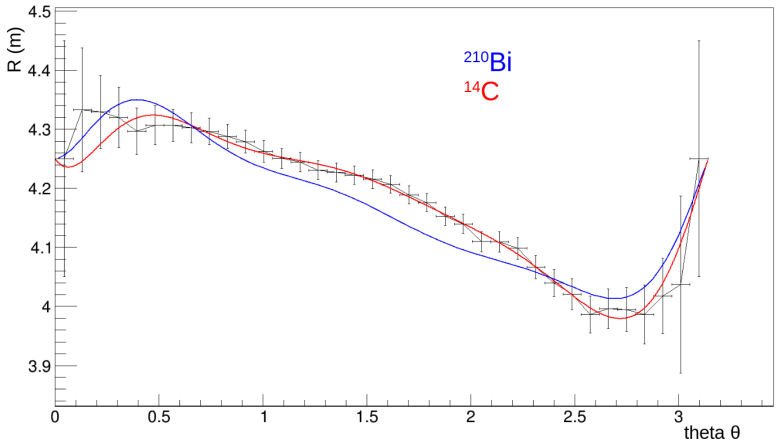

Figure 7.4.1: Comparison of the IV shapes from the two reconstruction algorithms for the week with the most displaced position on an antineutrino candidate.

In this work, the effects of the two reconstruction algorithms namely the ^{14}C and the ^{210}Bi as mentioned in Section 6.5 on the position of the candidate was also studied. Antineutrino candidates less than 10 cm from the IV were used for this. The maximum spread on the distance was

obtained as 1.4 cm for a candidate during the WE cycles. Even though, the number of candidates remain the same, this leads to a 4.1% systematic error in the position due to the different IV reconstruction algorithms. The comparison of the two algorithms for the corresponding week of the candidate is shown in Figure 7.4.1. The uncertainty in the position reconstruction was also calculated from the calibration data previously and has been reported to be 3.8% [27]. These systematic errors lead to an exposure of 1271 ± 10 (IV reco) ± 72 (pos.reco) ton·yr for the updated statistics and 1671 ± 13 (IV reco) ± 94 (pos.reco) ton·yr for the optimised cuts.

MC efficiency Discrepancies in the data and MC due to events closer to the IV can be studied using the event rate for the 2.2 MeV peak of the delayed event in ^{241}Am-^{9}Be calibration data. The spread in the efficiency and the uncertainty that arises from event losses closer to the FV edge led to a systematic error of 1.5 % in the MC efficiency in the previous analysis [27]. This is also extended to the current analysis. Thus the exposure with updated statistics can be given as 1271 ± 19 ton·yr and with optimised cuts can be given as 1671 ± 25 ton·yr when including just the systematic uncertainty due the MC efficiency.

Atmospheric neutrino background A recent study of atmospheric (anti)neutrinos in Borexino [28] indicated that it might become one of the backgrounds for geoneutrino analysis. The flux of different atmospheric neutrinos and the IBD-like reactions due to their interaction with ^{12}C and p in the scintillator is given in Figure 7.4.2.

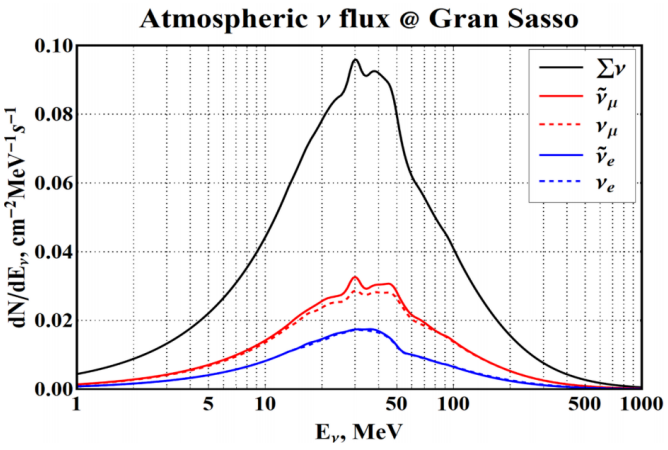

(a)

14.71878%	$\nu_\mu + {}^{12}C \rightarrow \nu_\mu + n + {}^{11}C$
10.07451%	$\nu_e + {}^{12}C \rightarrow \nu_e + n + {}^{11}C$
9.42839%	$\bar{\nu}_e + p \rightarrow e^+ + n$
7.64519%	$\nu_\mu + {}^{12}C \rightarrow \nu_\mu + n + p + {}^{10}B$
7.00214%	$\nu_\tau + {}^{12}C \rightarrow \nu_\tau + n + {}^{11}C$
6.60916%	$\bar{\nu}_\mu + {}^{12}C \rightarrow \bar{\nu}_\mu + n + {}^{11}C$
5.25160%	$\bar{\nu}_e + {}^{12}C \rightarrow \bar{\nu}_e + n + {}^{11}C$
5.10870%	$\nu_\tau + {}^{12}C \rightarrow \nu_\tau + n + p + {}^{10}B$
5.03725%	$\nu_e + {}^{12}C \rightarrow \nu_e + n + p + {}^{10}B$
4.03695%	$\bar{\nu}_\tau + {}^{12}C \rightarrow \bar{\nu}_\tau + n + {}^{11}C$
3.89405%	$\nu_\mu + {}^{12}C \rightarrow \nu_\mu + 2n + {}^{10}C$
3.64397%	$\bar{\nu}_\mu + {}^{12}C \rightarrow \bar{\nu}_\mu + n + p + {}^{10}B$
2.96519%	$\bar{\nu}_e + {}^{12}C \rightarrow \bar{\nu}_e + n + p + {}^{10}B$
2.35786%	$\nu_e + {}^{12}C \rightarrow \nu_e + 2n + {}^{10}C$
1.78626%	$\nu_\tau + {}^{12}C \rightarrow \nu_\tau + 2n + {}^{10}C$
1.67908%	$\bar{\nu}_\tau + {}^{12}C \rightarrow \bar{\nu}_\tau + n + p + {}^{10}B$
1.46473%	$\bar{\nu}_\mu + {}^{12}C \rightarrow \bar{\nu}_\mu + 2n + {}^{10}C$
1.21466%	$\bar{\nu}_e + {}^{12}C \rightarrow \bar{\nu}_e + 2n + {}^{10}C$
1.17893%	$\bar{\nu}_\tau + {}^{12}C \rightarrow \bar{\nu}_\tau + 2n + {}^{10}C$
4.9026%	*other 68 reactions*

(b)

Figure 7.4.2: (a) Different atmoshperic neutrino fluxes at LNGS. (b) Amount of IBD-like events formed due to different reactions in the scintillator. (Figures used from [28])

This analysis was done by generating 500k events in a spherical vessel of radius 4.25 m and filtering events according to the standard selection cuts used for geoneutrino analysis. This yielded 5.68 ± 2.36 events due to ^{12}C-capture and 0.009 ± 0.9 events due to p-cature in the current geoneutrino sample. In this work, the effect of the background due to ^{12}C capture on the final fit results was studied for the updated statistics with standard selection cuts as shown in Figure 7.4.3. The results obtained were N_{geo} = 30.1 ± 7.1 events and N_{rea} = 66.5 ± events. After comparing these values to the results obtained in Section 7.1, systematic errors of 1.2 events in N_{geo} and 3.3 events in N_{rea} were obtained due to atmospheric neutrino background. After leaving the U and Th parameters free, a difference of 1.2 events was observed in N_U.

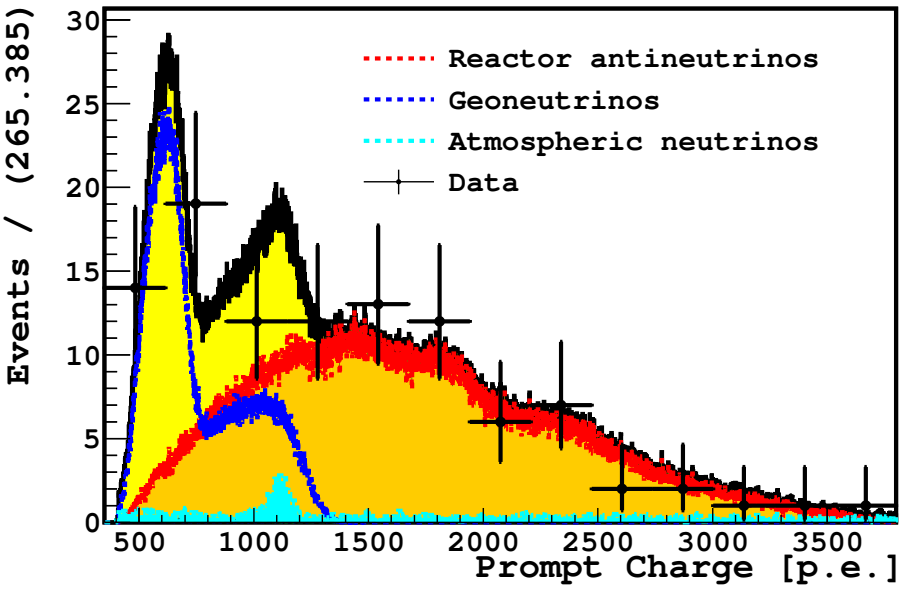

Figure 7.4.3: Likelihood fit results after the inclusion of atmoshperic neutrino background on the 102 candidates obtained from updated statistics with standard selection cuts.

Reactor antineutrinos with and without bump at 5 MeV The effect of the reactor antineutrinos with and without bump at 5 MeV as explained in Section 4.1 was studied on the fit results. The comparison of the MC generated prompt energy spectra of reactor antineutrinos with and without bump is shown in Figure 7.4.4.

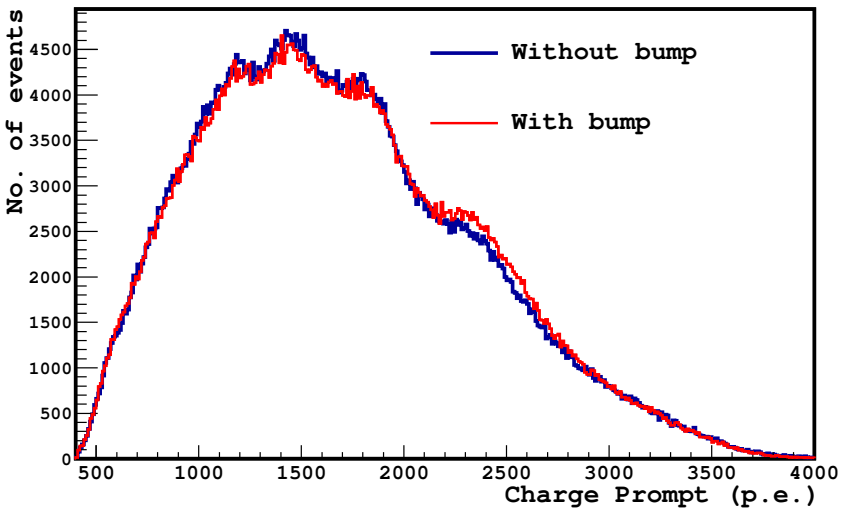

Figure 7.4.4: Comparison of MC prompt energy spectra for reactor antineutrinos with and without bump at 5 MeV (The spectrum without the bump was scaled to the number of entries in the spectrum with the bump).

The effect was studied for the optmized selection cuts and the results obtained were $N_{geo} = 40.8 \pm 8$ events and $N_{rea} = 86.8 \pm 10.4$ events. After comparing these values to the results obtained in Section 7.2, systematic errors of 0.11 events in N_{geo} and 0.18 events in N_{rea} were obtained due to the 5 MeV bump in reactor antineutrino spectra. After leaving the U and Th parameters free, a difference of 0.2 events in N_U and a difference of 0.3 events in N_{Th} were observed.

7.5 Interpretation of Results

The total exposure after considering the systematic errors can be given as 1271 ± 74 ton·yr for the improved statistics with the same selections as in [7] and 1671 ± 98 ton·yr for the optimised selection cuts. Including the systematic error on exposure, the systematic errors arising due to atmospheric neutrinos, and due to the 5 MeV bump at the reactor antineutrino spectra, the final values and the geoneutrino fluxes of the U and Th chains are compared to the values in [7] in Table 7.5.1.

Criteria	**2015 [7]**	**Updated Statistics**	**Optimised Cuts**
Exposure	907 ± 44 ton·yr	1271 ± 74 ton·yr	1671 ± 98 ton·yr
Efficiency	84.2 ± 1.5%	82.3 ± 1.5%	87.1 ± 1.5%
Antineutrino candidates	77	102	131
Fixed chondritic ratio			
N_{geo} [events]	$23.7^{+6.5}_{-5.7}$	31.3 ± 7.1	41 ± 8
N_{rea} [events]	$52.7^{+8.5}_{-7.7}$	69.8 ± 9.4	86.7 ± 10.4
S_{geo} [TNU]	$43.5^{+11.8}_{-10.4}$(stat) $^{+2.7}_{-2.4}$(syst)	40.9 ± 9.3(stat) $^{+2.97}_{-2.7}$(syst)	$40.7^{+8}_{7.9}$(stat) $^{+2.9}_{-2.5}$(syst)
S_{rea} [TNU]	$96.6^{+15.6}_{-14.2}$(stat) $^{+4.9}_{-5.0}$(syst)	91.2 ± 12.3(stat) $^{+7.1}_{-6.6}$(syst)	$86.2^{+10.3}_{-10.4}$(stat) $^{+7.1}_{-6.6}$(syst)
Uncertainty	26.2%	23.8%	20.6%
S_U [TNU]	$34.6^{+5.9}_{-4.8}$	$30.7^{+7.2}_{-7.4}$	$30.5^{+6.2}_{-6.4}$
S_{Th} [TNU]	$8.9^{+2.4}_{-1.5}$	$10.2^{+2.4}_{-2.3}$	$10.2^{+2.1}_{-2.3}$
ϕ(U)	(2.7±0.7) x 10^6 cm^{-2}s^{-1}	(2.4±0.8) x 10^6 cm^{-2}s^{-1}	(2.4±0.5) x 10^6 cm^{-2}s^{-1}
ϕ(Th)	(2.3±0.6) x 10^6 cm^{-2}s^{-1}	(2.5±0.6) x 10^6 cm^{-2}s^{-1}	(2.5±0.5) x 10^6 cm^{-2}s^{-1}
Free chondritic ratio			
N_U [events]	$14.2^{+10.2}_{-9.1}$	23.7 ± 11.3	19.7 ± 12.2
N_{Th} [events]	$8.2^{+6.2}_{-6.3}$	7.6 ± 6.97	17.8 ± 8.1
S_U [TNU]	-	$18.2^{+8.7}_{-8.6}$(stat)$^{+1.5}_{-1.4}$(syst)	$19.9^{+12.4}_{-12.3}$(stat)$^{+1.8}_{-1.6}$(syst)
S_{Th} [TNU]	-	5.6±5.1(stat)±3.6(syst)	17.2±7.8(stat)±1(syst)
ϕ(U)	-	(1.4±0.7) x 10^6 cm^{-2}s^{-1}	(1.6±1) x 10^6 cm^{-2}s^{-1}
ϕ(Th)	-	(1.4±1.5) x 10^6 cm^{-2}s^{-1}	(4.2±2) x 10^6 cm^{-2}s^{-1}

Table 7.5.1: Comparison of the final results to the values published in [7].

The reactor antineutrino prediction [49] of (84.8 ± 4.2) TNU for without bump and (79.9 ± 4) TNU for with bump at LNGS lies within the 1σ band of reactor antineutrino background obtained from the fit results. The fluxes were calculated using the formulas 1.4.2 and 1.4.1 as mentioned earlier in Section 1.4. The results are compared to the BSE models in Figure 7.5.1. This is to be compared to Figure 3.3.2.

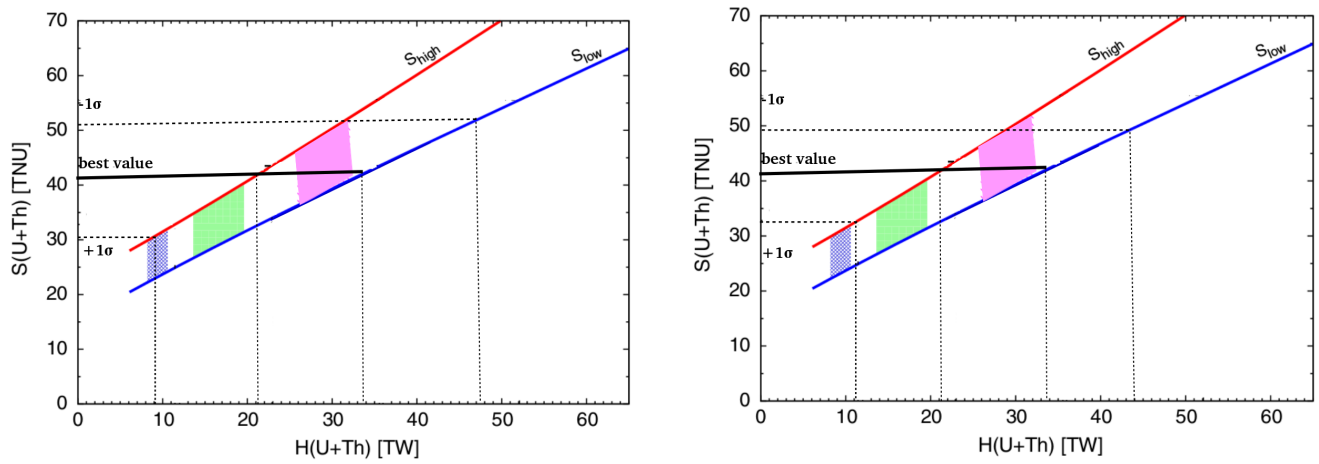

(a) (b)

Figure 7.5.1: Final results compared to the three BSE models namely cosmochemical (blue), geochemical (green), and geodynamical (magenta) for (a) updated statistics only and (b) updated statistics with the optimised selection cuts.

The mantle signal can be extracted from the obtained results and the expected total crustal contribution at LNGS, i.e. $S_{(LOC+ROC)} = 23.4 \pm 2.8$ TNU [42]. The obtained results in 2015 [7] and the results obtained in this work are compared to the crustal contribution in Figure 7.5.2.

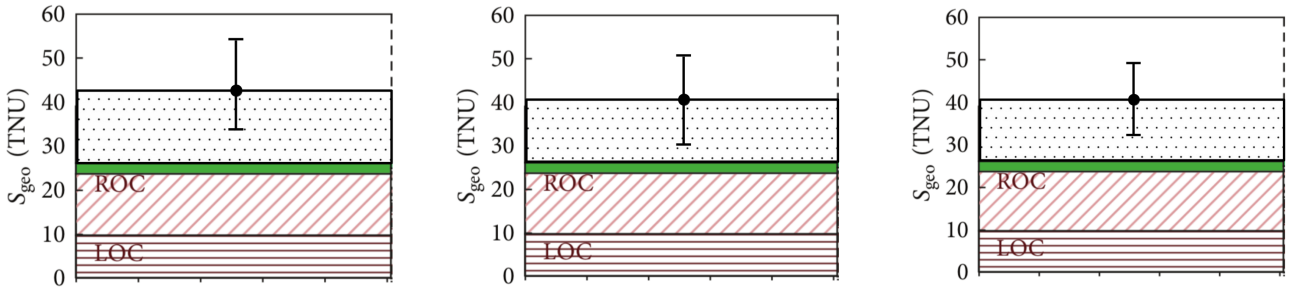

(a) (b) (c)

Figure 7.5.2: $S_{(LOC+ROC)}$ compared to the obtained geoneutrino signal (a) in 2015 [7] (b) for the updated statistics in the current work and (c) for the optmized selection cuts in the current work (Figure reused from [42]).

8 Outlook

8.1 Inner Detector Flag (IDF)

Truncation of Clusters A cluster is defined as an aggregation of decoded hits in the DAQ time window of Borexino. The cluster duration is not truncated for all events in Borexino due to a bug in the software, allowing high energy events to have a cluster duration greater than 1.5 μs. This is important for the distinction of muon events in the higher energy ranges as the cluster duration affects the mean time and energy of the cluster. As mentioned in Section 4.2, the IDF and special d4 conditions rely on the mean time of the cluster. When studying the mean time (short variable) of clusters as a function of their visible energy (nhits short) as previously done in [15] (Figure 4.2.1) for the entire data set, there was a class of tt1 BTB 0 events with a cluster duration greater than 1.5 μs. The IDF flag tagged events with high mean time even if the mean time vs nhits distribution was different than the MTB muons. This indicates that these are not just muons, but a mixture of different kinds of events including noise and retriggering of muons as seen in Figure 8.1.1

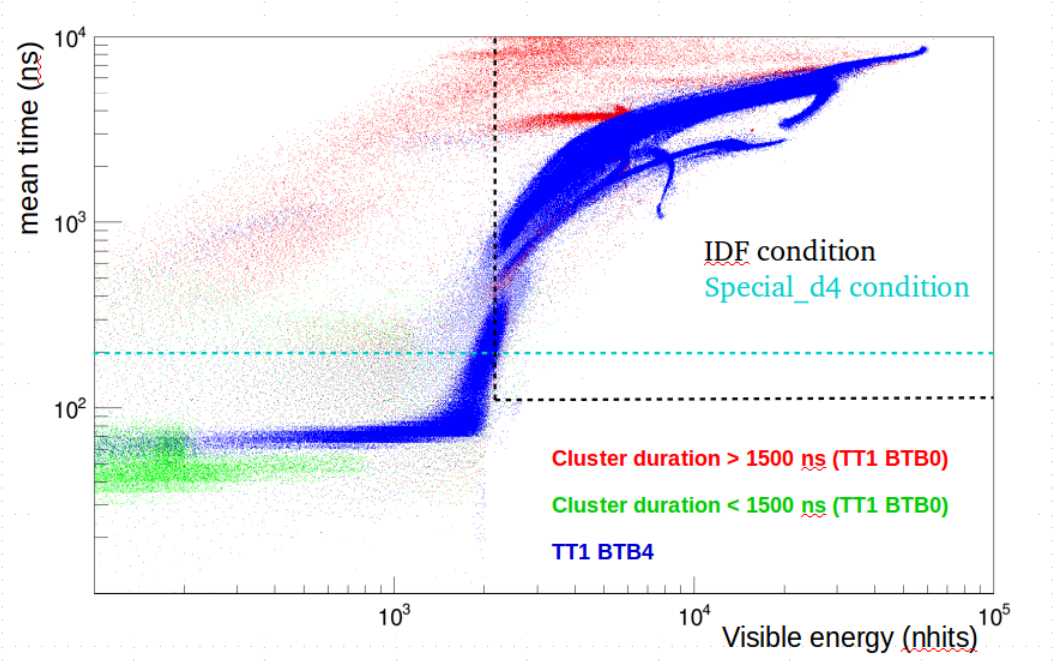

Figure 8.1.1: Mean time short vs nhits short for BTB 4 events (blue), BTB 0 events with cluster duration above (red) and below 1.5 μs (green). The IDF and special d4 conditions are marked by the dashed lines.

In order to study the effects of truncating the clusters, studies were done on one month of truncated and normal data. High energy events were split into more clusters and this affected the mean time and the energy of the clusters but not the peak time as expected. The total number of muons tagged was almost the same (99.9995%) as of the previously tagged muons were tagged before truncation. But, 17.7% of BTB 0 IDF muons were not tagged as IDF muons any more. 42 out of 236 events were missed and these 42 events can be divided into three classes: 7 of them were retriggering of BTB 0 IDF muons (Figure 8.1.2), 34 of them were consecutive chains of noise events (Figure 8.1.3) and 1 event was preceded by a service trigger with a muon falling in the DAQ window at the same time. The third type is explained in Section 8.2.

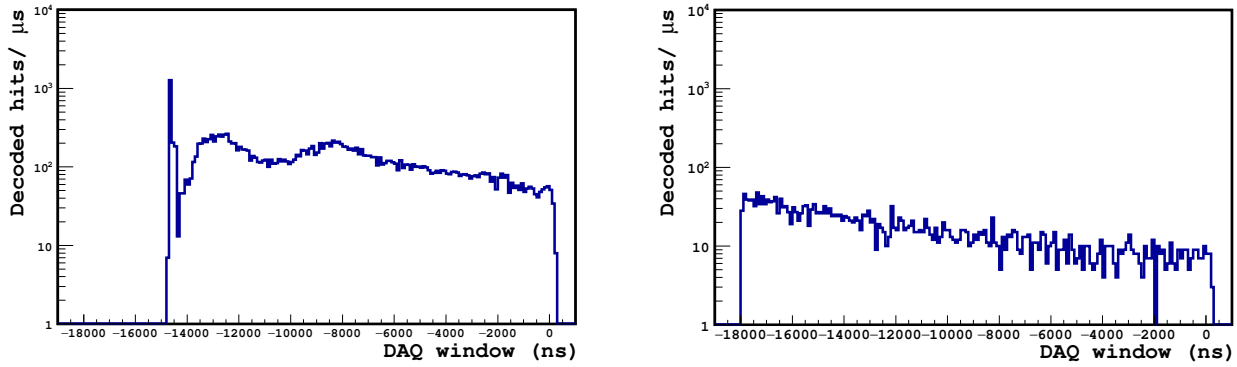

(a) (b)

Figure 8.1.2: (a) BTB 0 IDF muon. (b) Subsequent event that is a retriggering after (a) tagged as IDF muon before cluster truncation.

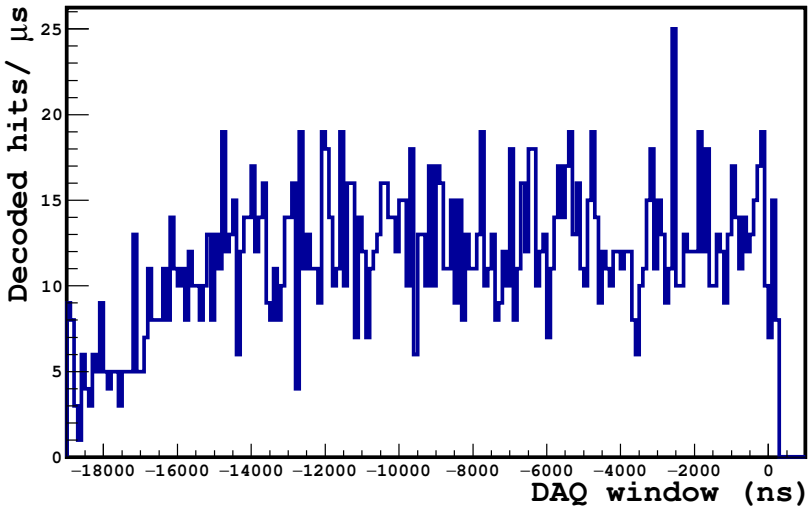

Figure 8.1.3: Example of noise event tagged as IDF muon before cluster truncation.

Thus, the over-efficiency of the IDF flag can be reduced by truncating the clusters. This resulted in a 0.03% and 0.04% increase in the mutual efficiencies of the MTB and MCR flags w.r.t the IDF flag, respectively. The 0.0005% of the total muons which was missed accounts to one muon. This was an exclusive special d4 muon whose mean time dropped to 180.8 ns after truncation, just below the threshold of the special d4 condition. In addition, a BTB 4 muon previously tagged as IDF muon was also missed after truncation. These muons can be tagged by studying the change in nhits and mean time distributions of muons before and after truncation which requires more statistics and slight retuning of the IDF conditions.

Mutual inefficiency of IDF The mutual efficiency of the IDF flag w.r.t to the MTB and MCR flags have been decreasing over the years as mentioned in Section 4.2.7. In order to study which of the three IDF conditions cause the decrease, the mutual efficiency of IDF w.r.t. MTB was studied for the three conditions separately. It was found that the efficiency has been decreasing in the energy range 80-900 nhits as shown in Figure 8.1.4 (a) and it is correlated to the decreasing amount of active PMTs in the detector as shown in Figure 8.1.4 (b).

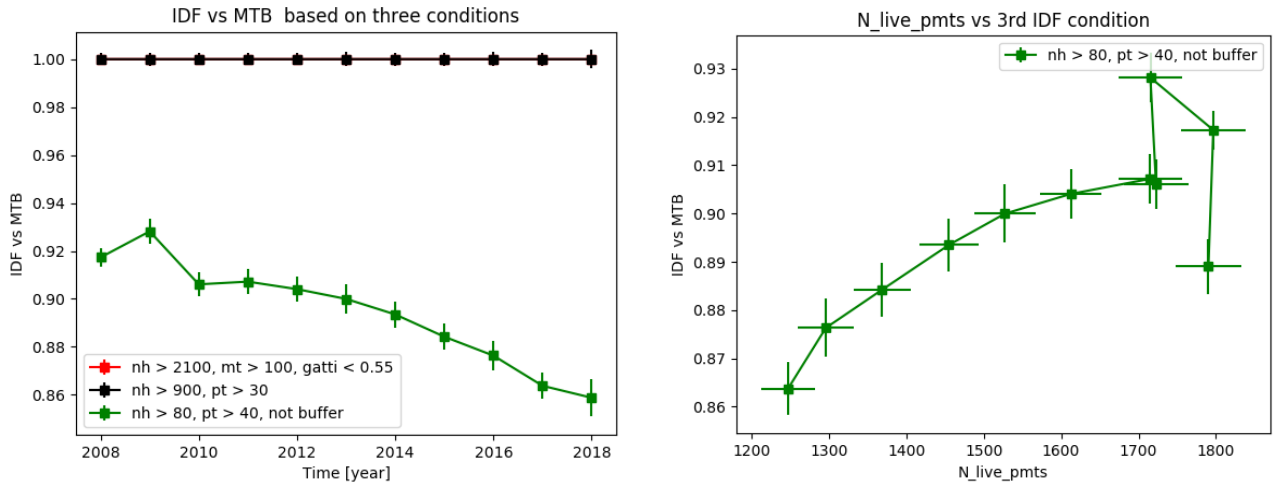

(a) (b)

Figure 8.1.4: Mutual efficiency of IDF w.r.t. MTB for the three IDF conditions. (b) Mutual efficiency of IDF w.r.t. MTB for the third IDF condition as a function of number of active PMTs.

8.2 Special Muons

New Special Flag As discussed in the previous section, while observing the muons missed after truncation, there was a muon which fell into the DAQ window of a service trigger and the succeeding event which was actually the retriggering of the muon was tagged as an IDF muon before truncation (Figure 8.2.1). This warrants the further study of these muons, i.e. the amount of these kind of muons and their effect on the muon tagging efficiency. After studying their trends, a new special flag can be introduced based on the number of decoded hits in service triggers.

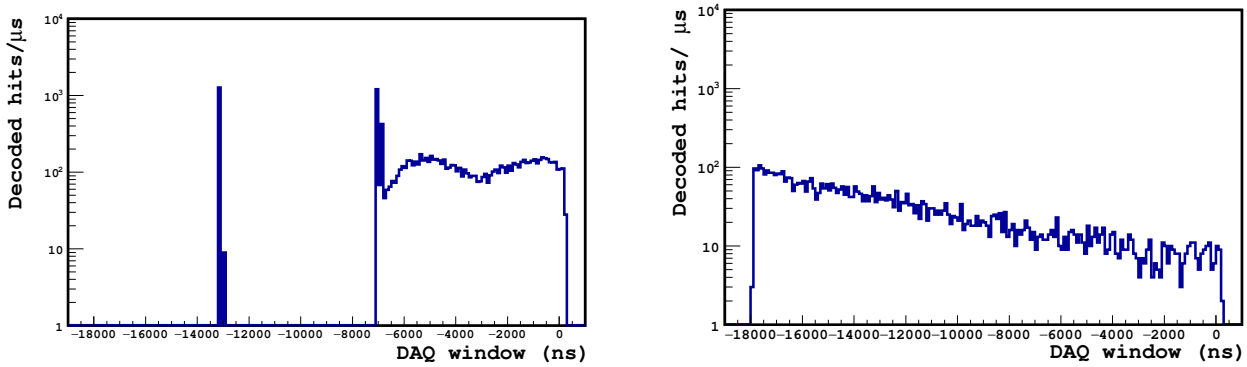

(a) (b)

Figure 8.2.1: (a) Service trigger showing a peak at around 2 μs and a muon falling into the gate at around 9 μs. (b) Retriggering of the muon from (a) tagged as IDF muon before truncation.

Special d3 muons The amount of BTB 0 muons in the sample of internal muons reduced from 38% to 6.5% as previously mentioned in Section 6.1. 6.5% is still a high amount of muons given that the mutual efficiency of MTB is around 99%. 67% of the BTB 0 muons are tagged as special d3 which is suspiciously high indicating that retriggering of muons might also be tagged as special d3. In order to check if there is over-efficiency in the special d3 tagging, the number of single cluster events in the entire data set and the corresponding amount of dead time in the electronics after these events have to be studied. This will help in identifying the amount of muons expected during the electronics dead time when considering an ideal rate of 4300 muons/day.

8.3 Spatial Muon Vetoes

In the independent study done on ^{9}Li-^{8}He vetoes [53], an important improvement suggested was vetoing a specific part of the detector based on muon track reconstruction. Most of the muons with high amount of decoded hits where the hadronic background can be seen, have four track points, thus leading to more efficient track reconstruction. Construction of a cyclinder using these track points and the location of the IBD-like prompt event from the hadronic background can be useful in vetoing only a certain part of the detector as shown if Figure 8.3.1.

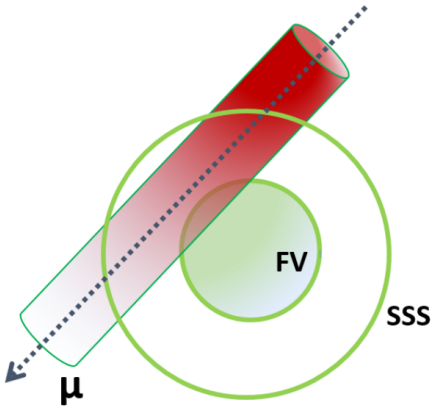

Figure 8.3.1: Representation of spatial vetoes based on muon track reconstruction [53].

8.4 Backgrounds

Untagged Muons The mutual inefficiency obtained in Section 4.2.7 can be used to calculate the amount of background arising from the untagged muons. One such background will be the hadronic background arising from these untagged muons. The 0.196% inefficiency corresponds to an additional number of 27518 muons in the entire data set. As explained in Section 6.1 and 6.6.2, 7.4% of the muons are either μ + n or BTB 0 muons which gives an estimate of 25 untagged muons of this kind. The tagged muons of this kind formed 241 IBD-like signals, thus giving an estimate of 0.0044 on the hadronic background due to untagged muons. 34.8% of the muons were of the type BTB 4 (μ -n) and formed 23 IBD-like signals. Therefore, the amount of hadronic background due to the untagged muons of this kind would be 0.0462. Thus, the total estimate of hadronic background due to untagged muons can be given as 0.051. The same logic can be extended to other backgrounds arising from the untagged muons, for example, muons which are folowed by two neutrons can imitate the prompt and delayed signals of IBD. This needs the evaluation of the amount of muons in the current sample which are followed by two neutrons in the tt128 gate.

Re-evaluation of other backgrounds The other backgrounds which were scaled using the exposure in this work needs to be revaluated for the precise expectation on the background events in the geoneutrino candidate sample. The changes in the detector over the years and the optimised cuts might have changed the behaviour of certain backgrounds. For example, the (γ,n) and (α, n) backgrounds might not scale with the exposure and might increase drastically near the IV due to the presence of background events on the IV.

9 References

[1] http://physics.nist.gov/physrefdata/xcom/html/xcom1.html.

[2] https://root.cern.ch/roofit.

[3] http://www.nndc.bnl.gov/.

[4] S. Abe, T. Ebihara, S. Enomoto, K. Furuno, Y. Gando, K. Ichimura, H. Ikeda, K. Inoue, Y. Kibe, Y. Kishimoto, M. Koga, A. Kozlov, Y. Minekawa, T. Mitsui, K. Nakajima, K. Nakajima, K. Nakamura, M. Nakamura, K. Owada, I. Shimizu, Y. Shimizu, J. Shirai, F. Suekane, A. Suzuki, Y. Takemoto, K. Tamae, A. Terashima, H. Watanabe, E. Yonezawa, S. Yoshida, J. Busenitz, T. Classen, C. Grant, G. Keefer, D. S. Leonard, D. McKee, A. Piepke, M. P. Decowski, J. A. Detwiler, S. J. Freedman, B. K. Fujikawa, F. Gray, E. Guardincerri, L. Hsu, R. Kadel, C. Lendvai, K.-B. Luk, H. Murayama, T. O'Donnell, H. M. Steiner, L. A. Winslow, D. A. Dwyer, C. Jillings, C. Mauger, R. D. McKeown, P. Vogel, C. Zhang, B. E. Berger, C. E. Lane, J. Maricic, T. Miletic, M. Batygov, J. G. Learned, S. Matsuno, S. Pakvasa, J. Foster, G. A. Horton-Smith, A. Tang, S. Dazeley, K. E. Downum, G. Gratta, K. Tolich, W. Bugg, Y. Efremenko, Y. Kamyshkov, O. Perevozchikov, H. J. Karwowski, D. M. Markoff, W. Tornow, K. M. Heeger, F. Piquemal, and J.-S. Ricol. Precision measurement of neutrino oscillation parameters with kamland. *Phys. Rev. Lett.*, 100:221803, Jun 2008.

[5] M. Agostini, K. Altenmüller, S. Appel, V. Atroshchenko, Z. Bagdasarian, D. Basilico, G. Bellini, J. Benziger, D. Bick, G. Bonfini, L. Borodikhina, D. Bravo, B. Caccianiga, F. Calaprice, A. Caminata, M. Canepa, S. Caprioli, M. Carlini, P. Cavalcante, A. Chepurnov, K. Choi, D. D'Angelo, S. Davini, A. Derbin, X.F. Ding, L. Di Noto, I. Drachnev, K. Fomenko, A. Formozov, D. Franco, F. Froborg, F. Gabriele, C. Galbiati, C. Ghiano, M. Giammarchi, M. Goeger-Neff, A. Goretti, M. Gromov, C. Hagner, T. Houdy, E. Hungerford, Aldo Ianni, Andrea Ianni, A. Jany, D. Jeschke, V. Kobychev, D. Korablev, G. Korga, D. Kryn, M. Laubenstein, E. Litvinovich, F. Lombardi, P. Lombardi, L. Ludhova, G. Lukyanchenko, I. Machulin, M. Magnozzi, G. Manuzio, S. Marcocci, J. Martyn, E. Meroni, M. Meyer, L. Miramonti, M. Misiaszek, V. Muratova, B. Neumair, L. Oberauer, B. Opitz, F. Ortica, M. Pallavicini, L. Papp, A. Pocar, G. Ranucci, A. Razeto, A. Re, A. Romani, R. Roncin, N. Rossi, S. Schönert, D. Semenov, P. Shakina, M. Skorokhvatov, O. Smirnov, A. Sotnikov, L.F.F. Stokes, Y. Suvorov, R. Tartaglia, G. Testera, J. Thurn, M. Toropova, E. Unzhakov, A. Vishneva, R.B. Vogelaar, F. von Feilitzsch, H. Wang, S. Weinz, M. Wojcik, M. Wurm, Z. Yokley, O. Zaimidoroga, S. Zavatarelli, K. Zuber, and G. Zuzel. The monte carlo simulation of the borexino detector. *Astroparticle Physics*, 97:136 – 159, 2018.

[6] M. Agostini, K. Altenmüller, S. Appel, V. Atroshchenko, D. Basilico, G. Bellini, J. Benziger, D. Bick, G. Bonfini, L. Borodikhina, D. Bravo, B. Caccianiga, F. Calaprice, A. Caminata, S. Caprioli, M. Carlini, P. Cavalcante, A. Chepurnov, K. Choi, D. D'Angelo, S. Davini, A. Derbin, X.F. Ding, L. Di Noto, I. Drachnev, K. Fomenko, D. Franco, F. Froborg, F. Gabriele, C. Galbiati, C. Ghiano, M. Giammarchi, M. Goeger-Neff, A. Goretti, M. Gromov, C. Hagner, T. Houdy, E. Hungerford, Aldo Ianni, Andrea Ianni, A. Jany, D. Jeschke, V. Kobychev, D. Korablev, G. Korga, D. Kryn, M. Laubenstein, B. Lehnert, E. Litvinovich, F. Lombardi, P. Lombardi, L. Ludhova, G. Lukyanchenko, I. Machulin, S. Manecki, G. Manuzio, S. Marcocci, J. Martyn, E. Meroni, M. Meyer, L. Miramonti, M. Misiaszek, M. Montuschi, V. Muratova, B. Neumair, L. Oberauer, B. Opitz, F. Ortica, M. Pallavicini, L. Papp, A. Pocar, G. Ranucci, A. Razeto, A. Re, A. Romani, R. Roncin, N. Rossi, S. Schönert, D. Semenov, P. Shakina, M. Skorokhvatov, O. Smirnov, A. Sotnikov, L.F.F. Stokes, Y. Suvorov, R. Tartaglia, G. Testera, J. Thurn, M. Toropova, E. Unzhakov, A. Vishneva, R.B. Vogelaar, F. von Feilitzsch, H. Wang, S. Weinz, M. Wojcik, M. Wurm, Z. Yokley, O. Zaimidoroga, S. Zavatarelli, K. Zuber, and G. Zuzel. Seasonal modulation of the 7be solar neutrino rate in borexino. *Astroparticle Physics*, 92:21 – 29, 2017.

[7] M. Agostini, S. Appel, G. Bellini, J. Benziger, D. Bick, G. Bonfini, D. Bravo, B. Caccianiga, F. Calaprice, A. Caminata, P. Cavalcante, A. Chepurnov, K. Choi, D. D'Angelo, S. Davini, A. Derbin, L. Di Noto, I. Drachnev, A. Empl, A. Etenko, G. Fiorentini, K. Fomenko, D. Franco, F. Gabriele, C. Galbiati, C. Ghiano, M. Giammarchi, M. Goeger-Neff, A. Goretti, M. Gromov, C. Hagner, T. Houdy, E. Hungerford, Aldo Ianni, Andrea Ianni, K. Jedrzejczak, M. Kaiser, V. Kobychev, D. Korablev, G. Korga, D. Kryn, M. Laubenstein, B. Lehnert, E. Litvinovich, F. Lombardi, P. Lombardi, L. Ludhova, G. Lukyanchenko, I. Machulin, S. Manecki, W. Maneschg, F. Mantovani, S. Marcocci, E. Meroni, M. Meyer, L. Miramonti, M. Misiaszek, M. Montuschi, P. Mosteiro, V. Muratova, B. Neumair, L. Oberauer, M. Obolensky, F. Ortica, K. Otis, L. Pagani, M. Pallavicini, L. Papp, L. Perasso, A. Pocar, G. Ranucci, A. Razeto, A. Re, B. Ricci, A. Romani, R. Roncin, N. Rossi, S. Schönert, D. Semenov, H. Simgen, M. Skorokhvatov, O. Smirnov, A. Sotnikov, S. Sukhotin, Y. Suvorov, R. Tartaglia, G. Testera, J. Thurn, M. Toropova, E. Unzhakov, R. B. Vogelaar, F. von Feilitzsch, H. Wang, S. Weinz, J. Winter, M. Wojcik, M. Wurm, Z. Yokley, O. Zaimidoroga, S. Zavatarelli, K. Zuber, and G. Zuzel. Spectroscopy of geoneutrinos from 2056 days of borexino data. *Phys. Rev. D*, 92:031101, Aug 2015.

[8] Claude J. Allègre, Jean-Paul Poirier, Eric Humler, and Albrecht W. Hofmann. The chemical composition of the earth. *Earth and Planetary Science Letters*, 134(3):515 – 526, 1995.

[9] Fengpeng An, Guangpeng An, Qi An, Vito Antonelli, Eric Baussan, John Beacom, Leonid Bezrukov, Simon Blyth, Riccardo Brugnera, Margherita Buizza Avanzini, Jose Busto, Anatael Cabrera, Hao Cai, Xiao Cai, Antonio Cammi, Guofu Cao, Jun Cao, Yun Chang, Shaomin Chen, Shenjian Chen, Yixue Chen, Davide Chiesa, Massimiliano Clemenza, Barbara Clerbaux, Janet Conrad, Davide D'Angelo, Hervé De Kerret, Zhi Deng, Ziyan Deng, Yayun Ding, Zelimir Djurcic, Damien Dornic, Marcos Dracos, Olivier Drapier, Stefano Dusini, Stephen Dye, Timo Enqvist, Donghua Fan, Jian Fang, Laurent Favart, Richard Ford, Marianne Göger-Neff, Haonan Gan, Alberto Garfagnini, Marco Giammarchi, Maxim Gonchar, Guanghua Gong, Hui Gong, Michel Gonin, Marco Grassi, Christian Grewing, Mengyun Guan, Vic Guarino, Gang Guo, Wanlei Guo, Xin-Heng Guo, Caren Hagner, Ran Han, Miao He, Yuekun Heng, Yee Hsiung, Jun Hu, Shouyang Hu, Tao Hu, Hanxiong Huang, Xingtao Huang, Lei Huo, Ara Ioannisian, Manfred Jeitler, Xiangdong Ji, Xiaoshan Jiang, Cécile Jollet, Li Kang, Michael Karagounis, Narine Kazarian, Zinovy Krumshteyn, Andre Kruth, Pasi Kuusiniemi, Tobias Lachenmaier, Rupert Leitner, Chao Li, Jiaxing Li, Weidong Li, Weiguo Li, Xiaomei Li, Xiaonan Li, Yi Li, Yufeng Li, Zhi-Bing Li, Hao Liang, Guey-Lin Lin, Tao Lin, Yen-Hsun Lin, Jiajie Ling, Ivano Lippi, Dawei Liu, Hongbang Liu, Hu Liu, Jianglai Liu, Jianli Liu, Jinchang Liu, Qian Liu, Shubin Liu, Shulin Liu, Paolo Lombardi, Yongbing Long, Haoqi Lu, Jiashu Lu, Jingbin Lu, Junguang Lu, Bayarto Lubsandorzhiev, Livia Ludhova, Shu Luo, Vladimir Lyashuk, Randolph Möllenberg, Xubo Ma, Fabio Mantovani, Yajun Mao, Stefano M Mari, William F McDonough, Guang Meng, Anselmo Meregaglia, Emanuela Meroni, Mauro Mezzetto, Lino Miramonti, Thomas Mueller, Dmitry Naumov, Lothar Oberauer, Juan Pedro Ochoa-Ricoux, Alexander Olshevskiy, Fausto Ortica, Alessandro Paoloni, Haiping Peng, Jen-Chieh Peng, Ezio Previtali, Ming Qi, Sen Qian, Xin Qian, Yongzhong Qian, Zhonghua Qin, Georg Raffelt, Gioacchino Ranucci, Barbara Ricci, Markus Robens, Aldo Romani, Xiangdong Ruan, Xichao Ruan, Giuseppe Salamanna, Mike Shaevitz, Valery Sinev, Chiara Sirignano, Monica Sisti, Oleg Smirnov, Michael Soiron, Achim Stahl, Luca Stanco, Jochen Steinmann, Xilei Sun, Yongjie Sun, Dmitriy Taichenachev, Jian Tang, Igor Tkachev, Wladyslaw Trzaska, Stefan van Waasen, Cristina Volpe, Vit Vorobel, Lucia Votano, Chung-Hsiang Wang, Guoli Wang, Hao Wang, Meng Wang, Ruiguang Wang, Siguang Wang, Wei Wang, Yi Wang, Yi Wang, Yifang Wang, Zhe Wang, Zheng Wang, Zhigang Wang, Zhimin Wang, Wei Wei, Liangjian Wen, Christopher Wiebusch, Björn Wonsak, Qun Wu, Claudia-Elisabeth Wulz, Michael Wurm, Yufei Xi, Dongmei Xia, Yuguang Xie, Zhi-zhong Xing, Jilei Xu, Baojun Yan, Changgen Yang, Chaowen Yang, Guang Yang, Lei Yang, Yifan Yang, Yu Yao, Ugur Yegin, Frédéric Yermia, Zhengyun You, Boxiang Yu, Chunxu Yu, Zeyuan Yu, Sandra Zavatarelli, Liang Zhan, Chao Zhang, Hong-Hao Zhang, Jiawen Zhang, Jingbo Zhang, Qingmin Zhang, Yu-Mei Zhang, Zhenyu Zhang, Zhenghua Zhao, Yangheng Zheng, Weili Zhong, Guorong Zhou, Jing Zhou, Li Zhou, Rong Zhou, Shun Zhou, Wenxiong Zhou, Xiang Zhou, Yeling Zhou, Yufeng Zhou, and Jiaheng Zou. Neutrino physics with juno. *Journal of Physics G: Nuclear and Particle Physics*, 43(3):030401, 2016.

[10] T. Araki, S. Enomoto, K. Furuno, Y. Gando, K. Ichimura, H. Ikeda, K. Inoue, Y. Kishimoto, M. Koga, Y. Koseki, T. Maeda, T. Mitsui, M. Motoki, K. Nakajima, H. Ogawa, M. Ogawa, K. Owada, J.-S. Ricol, I. Shimizu, J. Shirai, F. Suekane, A. Suzuki, K. Tada, S. Takeuchi, K. Tamae, Y. Tsuda, H. Watanabe, J. Busenitz, T. Classen, Z. Djurcic, G. Keefer, D. Leonard, A. Piepke, E. Yakushev, B. E. Berger, Y. D. Chan, M. P. Decowski, D. A. Dwyer, S. J. Freedman, B. K. Fujikawa, J. Goldman, F. Gray, K. M. Heeger, L. Hsu, K. T. Lesko, K.-B. Luk, H. Murayama, T. O'Donnell, A. W. P. Poon, H. M. Steiner, L. A. Winslow, C. Mauger, R. D. McKeown, P. Vogel, C. E. Lane, T. Miletic, G. Guillian, J. G. Learned, J. Maricic, S. Matsuno, S. Pakvasa, G. A. Horton-Smith, S. Dazeley, S. Hatakeyama, A. Rojas, R. Svoboda, B. D. Dieterle, J. Detwiler, G. Gratta, K. Ishii, N. Tolich, Y. Uchida, M. Batygov, W. Bugg, Y. Efremenko, Y. Kamyshkov, A. Kozlov, Y. Nakamura, H. J. Karwowski, D. M. Markoff, K. Nakamura, R. M. Rohm, W. Tornow, R. Wendell, M.-J. Chen, Y.-F. Wang, and F. Piquemal. Experimental investigation of geologically produced antineutrinos with kamland. *Nature*, 436:499 EP –, Jul 2005. Article.

[11] Ricardo Arevalo and William F. McDonough. Chemical variations and regional diversity observed in morb. *Chemical Geology*, 271(1):70 – 85, 2010.

[12] Ricardo Arevalo, William F. McDonough, and Mario Luong. The k/u ratio of the silicate earth: Insights into mantle composition, structure and thermal evolution. *Earth and Planetary Science Letters*, 278(3):361 – 369, 2009.

[13] H Back, G Bellini, J Benziger, D Bick, G Bonfini, D Bravo, M Buizza Avanzini, B Caccianiga, L Cadonati, F Calaprice, C Carraro, P Cavalcante, A Chavarria, A Chepurnov, D D'Angelo, S Davini, A Derbin, A Etenko, F von Feilitzsch, G Fernandes, K Fomenko, D Franco, C Galbiati, S Gazzana, C Ghiano, M Giammarchi, M Goeger-Neff, A Goretti, L Grandi, E Guardincerri, S Hardy, Aldo Ianni, Andrea Ianni, A Kayunov, S Kidner, V Kobychev, D Korablev, G Korga, Y Koshio, D Kryn, M Laubenstein, T Lewke, E Litvinovich, B Loer, F Lombardi, P Lombardi, L Ludhova, I Machulin, S Manecki, W Maneschg, G Manuzio, Q Meindl, E Meroni, L Miramonti, M Misiaszek, D Montanari, P Mosteiro, V Muratova, L Oberauer, M Obolensky, F Ortica,

K Otis, M Pallavicini, L Papp, L Perasso, S Perasso, A Pocar, R S Raghavan, G Ranucci, A Razeto, A Re, A Romani, N Rossi, D Rountree, A Sabelnikov, R Saldanha, C Salvo, S Schönert, H Simgen, M Skorokhvatov, O Smirnov, A Sotnikov, S Sukhotin, Y Suvorov, R Tartaglia, G Testera, D Vignaud, R B Vogelaar, J Winter, M Wojcik, A Wright, M Wurm, J Xu, O Zaimidoroga, S Zavatarelli, and G Zuzel. Borexino calibrations: hardware, methods, and results. *Journal of Instrumentation*, 7(10):P10018, 2012.

[14] H.O. Back, M. Balata, G. Bellini, J. Benziger, S. Bonetti, B. Caccianiga, F. Calaprice, F. Dalnoki-Veress, D. D'Angelo, A de Bellefon, H. de Kerret, A. Derbin, A. Etenko, K. Fomenko, R. Ford, D. Franco, C. Galbiati, S. Gazzana, M.G. Giammarchi, M. Goeger, A. Goretti, C. Grieb, S. Hardy, A. Ianni, A.M. Ianni, G. Korga, Y. Kozlov, D. Kryn, M. Laubenstein, M. Leung, E. Litvinovich, P. Lombardi, L. Ludhova, I. Machulin, I. Manno, D. Manuzio, G. Manuzio, F. Masetti, K. McCarty, E. Meroni, L. Miramonti, M. Misiaszek, D. Montanari, M.E. Monzani, V. Muratova, L. Niedermeier, L. Oberauer, M. Obolensky, F. Ortica, M. Pallavicini, L. Papp, L. Perasso, A. Pocar, R.S. Raghavan, G. Ranucci, A. Razeto, A. Sabelnikov, C. Salvo, S. Schönert, T. Shutt, H. Simgen, M. Skorokhvatov, O. Smirnov, A. Sonnenschein, A. Sotnikov, S. Sukhotin, Y. Suvorov, V. Tarasenkov, R. Tartaglia, G. Testera, D. Vignaud, R.B. Vogelaar, F. Von Feilitzsch, B. Williams, M. W'ojcik, O. Zaimidoroga, S. Zavatarelli, and G. Zuzel. Pulse-shape discrimination with the counting test facility. *Nuclear Instruments and Methods in Physics Research Section A: Accelerators, Spectrometers, Detectors and Associated Equipment*, 584(1):98 – 113, 2008.

[15] G Bellini, J Benziger, D Bick, S Bonetti, M Buizza Avanzini, B Caccianiga, L Cadonati, F Calaprice, C Carraro, A Chavarria, A Chepurnov, D D'Angelo, S Davini, A Derbin, A Etenko, F von Feilitzsch, K Fomenko, D Franco, C Galbiati, S Gazzana, C Ghiano, M Giammarchi, M Goeger-Neff, A Goretti, E Guardincerri, S Hardy, Aldo Ianni, Andrea Ianni, M Joyce, V Kobychev, Y Koshio, D Korablev, G Korga, D Kryn, M Laubenstein, C Lendvai, T Lewke, E Litvinovich, B Loer, F Lombardi, P Lombardi, L Ludhova, I Machulin, S Manecki, W Maneschg, G Manuzio, Q Meindl, E Meroni, L Miramonti, M Misiaszek, D Montanari, V Muratova, L Oberauer, M Obolensky, F Ortica, M Pallavicini, L Papp, L Perasso, S Perasso, A Pocar, R S Raghavan, G Ranucci, A Razeto, A Re, A Romani, D Rountree, A Sabelnikov, R Saldanha, C Salvo, S Schönert, H Simgen, M Skorokhvatov, O Smirnov, A Sotnikov, S Sukhotin, Y Suvorov, R Tartaglia, G Testera, D Vignaud, R B Vogelaar, J Winter, M Wojcik, A Wright, M Wurm, J Xu, O Zaimidoroga, S Zavatarelli, and G Zuzel. Muon and cosmogenic neutron detection in borexino. *Journal of Instrumentation*, 6(05):P05005, 2011.

[16] G. Bellini, J. Benziger, D. Bick, G. Bonfini, D. Bravo, M. Buizza Avanzini, B. Caccianiga, L. Cadonati, F. Calaprice, P. Cavalcante, A. Chavarria, A. Chepurnov, D. D'Angelo, S. Davini, A. Derbin, A. Empl, A. Etenko, K. Fomenko, D. Franco, C. Galbiati, S. Gazzana, C. Ghiano, M. Giammarchi, M. Göger-Neff, A. Goretti, L. Grandi, C. Hagner, E. Hungerford, Aldo Ianni, Andrea Ianni, V. Kobychev, D. Korablev, G. Korga, D. Kryn, M. Laubenstein, T. Lewke, E. Litvinovich, B. Loer, P. Lombardi, F. Lombardi, L. Ludhova, G. Lukyanchenko, I. Machulin, S. Manecki, W. Maneschg, G. Manuzio, Q. Meindl, E. Meroni, L. Miramonti, M. Misiaszek, R. Möllenberg, P. Mosteiro, V. Muratova, L. Oberauer, M. Obolensky, F. Ortica, K. Otis, M. Pallavicini, L. Papp, L. Perasso, S. Perasso, A. Pocar, G. Ranucci, A. Razeto, A. Re, A. Romani, N. Rossi, R. Saldanha, C. Salvo, S. Schönert, H. Simgen, M. Skorokhvatov, O. Smirnov, A. Sotnikov, S. Sukhotin, Y. Suvorov, R. Tartaglia, G. Testera, D. Vignaud, R.B. Vogelaar, F. von Feilitzsch, J. Winter, M. Wojcik, A. Wright, M. Wurm, J. Xu, O. Zaimidoroga, S. Zavatarelli, and G. Zuzel. Cosmogenic backgrounds in borexino at 3800 m water-equivalent depth. *Journal of Cosmology and Astroparticle Physics*, 2013(08):049, 2013.

[17] G. Bellini, J. Benziger, D. Bick, G. Bonfini, D. Bravo, M. Buizza Avanzini, B. Caccianiga, L. Cadonati, F. Calaprice, P. Cavalcante, A. Chavarria, A. Chepurnov, D. DAngelo, S. Davini, A. Derbin, A. Empl, A. Etenko, G. Fiorentini, K. Fomenko, D. Franco, C. Galbiati, S. Gazzana, C. Ghiano, M. Giammarchi, M. Goeger-Neff, A. Goretti, L. Grandi, C. Hagner, E. Hungerford, Aldo Ianni, Andrea Ianni, V.V. Kobychev, D. Korablev, G. Korga, Y. Koshio, D. Kryn, M. Laubenstein, T. Lewke, E. Litvinovich, B. Loer, P. Lombardi, F. Lombardi, L. Ludhova, G. Lukyanchenko, I. Machulin, S. Manecki, W. Maneschg, F. Mantovani, G. Manuzio, Q. Meindl, E. Meroni, L. Miramonti, M. Misiaszek, P. Mosteiro, V. Muratova, L. Oberauer, M. Obolensky, F. Ortica, K. Otis, M. Pallavicini, L. Papp, L. Perasso, S. Perasso, A. Pocar, G. Ranucci, A. Razeto, A. Re, B. Ricci, A. Romani, N. Rossi, A. Sabelnikov, R. Saldanha, C. Salvo, S. Schönert, H. Simgen, M. Skorokhvatov, O. Smirnov, A. Sotnikov, S. Sukhotin, Y. Suvorov, R. Tartaglia, G. Testera, D. Vignaud, R.B. Vogelaar, F. von Feilitzsch, J. Winter, M. Wojcik, A. Wright, M. Wurm, J. Xu, O. Zaimidoroga, S. Zavatarelli, and G. Zuzel. Measurement of geo-neutrinos from 1353 days of borexino. *Physics Letters B*, 722(4):295 – 300, 2013.

[18] G. Bellini, J. Benziger, D. Bick, G. Bonfini, D. Bravo, M. Buizza Avanzini, B. Caccianiga, L. Cadonati, F. Calaprice, P. Cavalcante, A. Chavarria, A. Chepurnov, D. D'Angelo, S. Davini, A. Derbin, A. Empl, A. Etenko, K. Fomenko, D. Franco, F. Gabriele, C. Galbiati, S. Gazzana, C. Ghiano, M. Giammarchi, M. Göger-Neff, A. Goretti, L. Grandi, M. Gromov, C. Hagner, E. Hungerford, Aldo Ianni, Andrea Ianni,

V. Kobychev, D. Korablev, G. Korga, D. Kryn, M. Laubenstein, T. Lewke, E. Litvinovich, B. Loer, F. Lombardi, P. Lombardi, L. Ludhova, G. Lukyanchenko, I. Machulin, S. Manecki, W. Maneschg, G. Manuzio, Q. Meindl, E. Meroni, L. Miramonti, M. Misiaszek, M. Montuschi, P. Mosteiro, V. Muratova, L. Oberauer, M. Obolensky, F. Ortica, K. Otis, M. Pallavicini, L. Papp, C. Pena-Garay, L. Perasso, S. Perasso, A. Pocar, G. Ranucci, A. Razeto, A. Re, A. Romani, N. Rossi, R. Saldanha, C. Salvo, S. Schönert, H. Simgen, M. Skorokhvatov, O. Smirnov, A. Sotnikov, S. Sukhotin, Y. Suvorov, R. Tartaglia, G. Testera, D. Vignaud, R. B. Vogelaar, F. von Feilitzsch, J. Winter, M. Wojcik, A. Wright, M. Wurm, J. Xu, O. Zaimidoroga, S. Zavatarelli, and G. Zuzel. Final results of borexino phase-i on low-energy solar neutrino spectroscopy. *Phys. Rev. D*, 89:112007, Jun 2014.

[19] G. Bellini, J. Benziger, S. Bonetti, M. Buizza Avanzini, B. Caccianiga, L. Cadonati, F. Calaprice, C. Carraro, A. Chavarria, F. Dalnoki-Veress, D. D'Angelo, S. Davini, H. de Kerret, A. Derbin, A. Etenko, G. Fiorentini, K. Fomenko, D. Franco, C. Galbiati, S. Gazzana, C. Ghiano, M. Giammarchi, M. Goeger-Neff, A. Goretti, E. Guardincerri, S. Hardy, Aldo Ianni, Andrea Ianni, M. Joyce, V.V. Kobychev, Y. Koshio, G. Korga, D. Kryn, M. Laubenstein, M. Leung, T. Lewke, E. Litvinovich, B. Loer, P. Lombardi, L. Ludhova, I. Machulin, S. Manecki, W. Maneschg, G. Manuzio, Q. Meindl, E. Meroni, L. Miramonti, M. Misiaszek, D. Montanari, V. Muratova, L. Oberauer, M. Obolensky, F. Ortica, M. Pallavicini, L. Papp, L. Perasso, S. Perasso, A. Pocar, R.S. Raghavan, G. Ranucci, A. Razeto, A. Re, B. Ricci, P. Risso, A. Romani, D. Rountree, A. Sabelnikov, R. Saldanha, C. Salvo, S. Schönert, H. Simgen, M. Skorokhvatov, O. Smirnov, A. Sotnikov, S. Sukhotin, Y. Suvorov, R. Tartaglia, G. Testera, D. Vignaud, R.B. Vogelaar, F. von Feilitzsch, J. Winter, M. Wojcik, A. Wright, M. Wurm, J. Xu, O. Zaimidoroga, S. Zavatarelli, and G. Zuzel. Observation of geo-neutrinos. *Physics Letters B*, 687(4):299 – 304, 2010.

[20] G. Bellini, D. Bick, G. Bonfini, D. Bravo, B. Caccianiga, F. Calaprice, A. Caminata, P. Cavalcante, A. Chavarria, A. Chepurnov, D. D'Angelo, S. Davini, A. Derbin, A. Etenko, G. Fernandes, K. Fomenko, D. Franco, C. Galbiati, C. Ghiano, M. Göger-Neff, A. Goretti, C. Hagner, E. Hungerford, Aldo Ianni, Andrea Ianni, V. Kobychev, D. Korablev, G. Korga, D. Krasnicky, D. Kryn, M. Laubenstein, J. M. Link, E. Litvinovich, F. Lombardi, P. Lombardi, L. Ludhova, G. Lukyanchenko, I. Machulin, S. Manecki, W. Maneschg, E. Meroni, M. Meyer, L. Miramonti, M. Misiaszek, P. Mosteiro, V. Muratova, L. Oberauer, M. Obolensky, F. Ortica, K. Otis, M. Pallavicini, E. Pantic, L. Papp, S. Perasso, A. Pocar, G. Ranucci, A. Razeto, A. Re, A. Romani, N. Rossi, R. Saldanha, C. Salvo, S. Schönert, D. Semenov, H. Simgen, M. Skorokhvatov, O. Smirnov, A. Sotnikov, S. Sukhotin, Y. Suvorov, R. Tartaglia, G. Testera, E. Unzhakov, R. B. Vogelaar, H. Wang, M. Wojcik, M. Wurm, O. Zaimidoroga, S. Zavatarelli, and G. Zuzel. Sox: Short distance neutrino oscillations with borexino. *Journal of High Energy Physics*, 2013(8):38, Aug 2013.

[21] The KamLAND Collaboration, A. Gando, Y. Gando, K. Ichimura, H. Ikeda, K. Inoue, Y. Kibe, Y. Kishimoto, M. Koga, Y. Minekawa, T. Mitsui, T. Morikawa, N. Nagai, K. Nakajima, K. Nakamura, K. Narita, I. Shimizu, Y. Shimizu, J. Shirai, F. Suekane, A. Suzuki, H. Takahashi, N. Takahashi, Y. Takemoto, K. Tamae, H. Watanabe, B. D. Xu, H. Yabumoto, H. Yoshida, S. Yoshida, S. Enomoto, A. Kozlov, H. Murayama, C. Grant, G. Keefer, A. Piepke, T. I. Banks, T. Bloxham, J. A. Detwiler, S. J. Freedman, B. K. Fujikawa, K. Han, R. Kadel, T. O'Donnell, H. M. Steiner, D. A. Dwyer, R. D. McKeown, C. Zhang, B. E. Berger, C. E. Lane, J. Maricic, T. Miletic, M. Batygov, J. G. Learned, S. Matsuno, M. Sakai, G. A. Horton-Smith, K. E. Downum, G. Gratta, K. Tolich, Y. Efremenko, O. Perevozchikov, H. J. Karwowski, D. M. Markoff, W. Tornow, K. M. Heeger, and M. P. Decowski. Partial radiogenic heat model for earth revealed by geoneutrino measurements. *Nature Geoscience*, 4:647 EP –, Jul 2011. Article.

[22] J. H. Davies and D. R. Davies. Earth's surface heat flux. *Solid Earth*, 1(1):5–24, 2010.

[23] G. L. Fogli, E. Lisi, A. Palazzo, and A. M. Rotunno. Combined analysis of kamland and borexino neutrino signals from th and u decays in the earth's interior. *Phys. Rev. D*, 82:093006, Nov 2010.

[24] A Gando, Y Gando, H Hanakago, H Ikeda, Kazuo Inoue, K Ishidoshiro, H Ishikawa, Masayuki Koga, R Matsuda, S Matsuda, T Mitsui, D Motoki, K Nakamura, A Obata, A Oki, Y Oki, M Otani, I Shimizu, Junpei Shirai, and M P. Decowski. Reactor on-off antineutrino measurement with kamland. *Phys. Rev. D*, 88:033001, 08 2013.

[25] Antineutrino Working Group. Analytical calculation of fast neutrons from rock. *Borexino Internal Reports*, 2009.

[26] Antineutrino Working Group. Update of geoneutrino analysis. *Borexino Internal Reports*, 2012.

[27] Antineutrino Working Group. Update of geoneutrino analysis. *Borexino Internal Reports*, 2015.

[28] Antineutrino Working Group. Atmospheric and hep neutrinos. *Borexino general meeting*, June 2018.

[29] Antineutrino Working Group. Reactor antineutrino spectrum in borexino. *Borexino general meeting*, June 2018.

[30] D. Han. Dynamical fiducial volume (dfv) studies. May 2018.

[31] Stanley R. Hart and Alan Zindler. In search of a bulk-earth composition. *Chemical Geology*, 57(3):247 – 267, 1986.

[32] Patrick Huber and Thomas Schwetz. Precision spectroscopy with reactor antineutrinos. *Phys. Rev. D*, 70:053011, Sep 2004.

[33] C. Jaupart, S. Labrosse, and J.C. Mareschal. Temperatures, heat and energy in the mantle of the earth. *Treatise of Geophysics, D.J. Stevenson, Ed.*, pages 1–53, 2007.

[34] M. Javoy, E. Kaminski, F. Guyot, D. Andrault, C. Sanloup, M. Moreira, S. Labrosse, A. Jambon, P. Agrinier, A. Davaille, and C. Jaupart. The chemical composition of the earth: Enstatite chondrite models. *Earth and Planetary Science Letters*, 293(3):259 – 268, 2010.

[35] E. Litvinovich and G. Lukyanchenko. Fadc data. user's guide. *Borexino Internal Reports*, 2015.

[36] F. Lombardi. The dynamical fiducial volume (dfv) implementation in bxfilter. *Borexino Internal Reports*, 2015.

[37] L. Ludhova. Low energy neutrino physics - geoneutrinos. *Particle Physics II lectures, Institute III B, Faculty of Mathematics, Computer Science and Natural Sciences, RWTH Aachen University*, Summer Semester 2017.

[38] L. Ludhova and S. Zavatarelli. Expected signal from european reactors and its systematic error. *Borexino Internal Reports*, 2009.

[39] L. Ludhova and S. Zavatarelli. (γ, n) reactions background. *Borexino Internal Reports*, 2009.

[40] L. Ludhova and S. Zavatarelli. Preliminary analysis on the coincidences signals due to the fast cosmogenic neutrons. *Borexino Internal Reports*, 2009.

[41] L. Ludhova and S. Zavatarelli. Rn contamination during we and the possible induced backgrounds for anti-analyses. *Borexino Internal Reports*, 2014.

[42] L. Ludhova and S. Zavaterelli. Studying the earth with geoneutrinos. *Advances in High Energy Physics*, 2013.

[43] William McDonough and S. Sun. The composition of the earth. *Chemical Geology*, 120:223–253, 03 1995.

[44] D.-M. Mei and A. Hime. Muon-induced background study for underground laboratories. *Phys. Rev. D*, 73:053004, Mar 2006.

[45] B. Neumair. Some extra backgrounds in a coincidence search. *Borexino analysis meeting*, May 2018.

[46] Hugh St.C ONeill and Herbert Palme. Collisional erosion and the non-chondritic composition of the terrestrial planets. *Philosophical Transactions of the Royal Society of London A: Mathematical, Physical and Engineering Sciences*, 366(1883):4205–4238, 2008.

[47] V. Orekhov. C-14 vessel shape reconsnstruction. *Borexino analysis meeting*, May 2015.

[48] H. Palme and H. S. C. O'Neill. Cosmochemical estimates of mantle composition. *Treatise on Geochemistry*, 2:568, December 2003.

[49] B. Ricci. Expected reactor antineutrino signal. September 2018.

[50] Vincent J. M. Salters and Andreas Stracke. Composition of the depleted mantle. *Geochemistry, Geophysics, Geosystems*, 5(5), 2004.

[51] P. Alvarez Sanchez, R. Barzaghi, G. Bellini, J. Benziger, B. Betti, L. Biagi, D. Bick, G. Bonfini, D. Bravo, M. Buizza Avanzini, B. Caccianiga, L. Cadonati, C. Carraro, P. Cavalcante, G. Cerretto, A. Chavarria, D. DAngelo, S. Davini, C. De Gaetani, A. Derbin, A. Etenko, H. Esteban, K. Fomenko, D. Franco, C. Galbiati, S. Gazzana, C. Ghiano, M. Giammarchi, M. Göger-Neff, A. Goretti, L. Grandi, E. Guardincerri, S. Hardy, Aldo Ianni, Andrea Ianni, M. Jones, A. Kayunov, V. Kobychev, D. Korablev, G. Korga, Y. Koshio, D. Kryn, M. Laubenstein, T. Lewke, E. Litvinovich, B. Loer, P. Lombardi, F. Lombardi, L. Ludhova, I. Machulin, S. Manecki, W. Maneschg, G. Manuzio, Q. Meindl, E. Meroni, L. Miramonti, M. Misiaszek, D. Missiaen, D. Montanari, P. Mosteiro, V. Muratova, L. Oberauer, M. Obolensky, F. Ortica, K. Otis, M. Pallavicini, L. Papp, D. Passoni, L. Pinto, L. Perasso, S. Perasso, V. Pettiti, C. Plantard, A. Pocar, R.S. Raghavan, G. Ranucci, A. Razeto, A. Re, A. Romani, N. Rossi, A. Sabelnikov, R. Saldanha, C. Salvo, S. Schönert, J. Serrano, H. Simgen, M. Skorokhvatov, O. Smirnov, A. Sotnikov, P. Spinnato, S. Sukhotin, Y. Suvorov, R. Tartaglia, G. Testera, D. Vignaud, M.G. Visconti, R.B. Vogelaar, F. von Feilitzsch, J. Winter, M. Wojcik, A. Wright, M. Wurm, J. Xu, O. Zaimidoroga, S. Zavatarelli, and G. Zuzel. Measurement of cngs muon neutrino speed with borexino. *Physics Letters B*, 716(3):401 – 405, 2012.

[52] The Borexino Collaboration, M. Agostini, K. Altenmüller, S. Appel, V. Atroshchenko, Z. Bagdasarian, D. Basilico, G. Bellini, J. Benziger, D. Bick, I. Bolognino, G. Bonfini, D. Bravo, B. Caccianiga, F. Calaprice, A. Caminata, S. Caprioli, M. Carlini, P. Cavalcante, F. Cavanna, A. Chepurnov, K. Choi, L. Collica, D. D'Angelo, S. Davini, A. Derbin, X. F. Ding, A. Di Ludovico, L. Di Noto, I. Drachnev, K. Fomenko, A. Formozov, D. Franco, F. Gabriele, C. Galbiati, M. Gschwender, C. Ghiano, M. Giammarchi, A. Goretti, M. Gromov, D. Guffanti, C. Hagner, T. Houdy, E. Hungerford, A. Ianni, A. Ianni, A. Jany, D. Jeschke, V. Kobychev, D. Korablev, G. Korga, V. A. Kudryavtsev, S. Kumaran, T. Lachenmaier, M. Laubenstein, E. Litvinovich, F. Lombardi, P. Lombardi, L. Ludhova, G. Lukyanchenko, L. Lukyanchenko, I. Machulin, G. Manuzio, S. Marcocci, J. Maricic, J. Martyn, S. Meighen-Berger, E. Meroni, M. Meyer, L. Miramonti, M. Misiaszek, V. Muratova, B. Neumair, L. Oberauer, B. Opitz, V. Orekhov, F. Ortica, M. Pallavicini, L. Papp, Ö. Penek, L. Pietrofaccia, N. Pilipenko, A. Pocar, A. Porcelli, G. Raikov, G. Ranucci, A. Razeto, A. Re, M. Redchuk, A. Romani, N. Rossi, S. Rottenanger, S. Schönert, D. Semenov, M. Skorokhvatov, O. Smirnov, A. Sotnikov, L. F. F. Stokes, Y. Suvorov, R. Tartaglia, G. Testera, J. Thurn, M. Toropova, E. Unzhakov, A. Vishneva, R. B. Vogelaar, F. von Feilitzsch, S. Weinz, M. Wojcik, M. Wurm, Z. Yokley, O. Zaimidoroga, S. Zavatarelli, K. Zuber, and G. Zuzel. Modulations of the Cosmic Muon Signal in Ten Years of Borexino Data. *ArXiv e-prints 1808.04207*, August 2018.

[53] S. Weinz. Phd thesis, improved veto for cosmogenic background and calibration studies for the borexino/sox experiment. 2018.

[54] Rhea K. Workman and Stanley R. Hart. Major and trace element composition of the depleted morb mantle (dmm). *Earth and Planetary Science Letters*, 231(1):53 – 72, 2005.

10 Publications

1. The Borexino Collaboration, M. Agostini, K. Altenmüller, S. Appel, V. Atroshchenko, Z. Bagdasarian, D. Basilico, G. Bellini, J. Benziger, D. Bick, I. Bolognino, G. Bonfini, D. Bravo, B. Caccianiga, F. Calaprice, A. Caminata, S. Caprioli, M. Carlini, P. Cavalcante, F. Cavanna, A. Chepurnov, K. Choi, L. Collica, D. D'Angelo, S. Davini, A. Derbin, X. F. Ding, A. Di Ludovico, L. Di Noto, I. Drachnev, K. Fomenko, A. Formozov, D. Franco, F. Gabriele, C. Galbiati, M. Gschwender, C. Ghiano, M. Giammarchi, A. Goretti, M. Gromov, D. Guffanti, C. Hagner, T. Houdy, E. Hungerford, A. Ianni, A. Ianni, A. Jany, D. Jeschke, V. Kobychev, D. Korablev, G. Korga, V. A. Kudryavtsev, S. Kumaran, T. Lachenmaier, M. Laubenstein, E. Litvinovich, F. Lombardi, P. Lombardi, L. Ludhova, G. Lukyanchenko, L. Lukyanchenko, I. Machulin, G. Manuzio, S. Marcocci, J. Maricic, J. Martyn, S. Meighen-Berger, E. Meroni, M. Meyer, L. Miramonti, M. Misiaszek, V. Muratova, B. Neumair, L. Oberauer, B. Opitz, V. Orekhov, F. Ortica, M. Pallavicini, L. Papp, Ö. Penek, L. Pietrofaccia, N. Pilipenko, A. Pocar, A. Porcelli, G. Raikov, G. Ranucci, A. Razeto, A. Re, M. Redchuk, A. Romani, N. Rossi, S. Rottenanger, S. Schönert, D. Semenov, M. Skorokhvatov, O. Smirnov, A. Sotnikov, L. F. F. Stokes, Y. Suvorov, R. Tartaglia, G. Testera, J. Thurn, M. Toropova, E. Unzhakov, A. Vishneva, R. B. Vogelaar, F. von Feilitzsch, S. Weinz, M. Wojcik, M. Wurm, Z. Yokley, O. Zaimidoroga, S. Zavatarelli, K. Zuber, and G. Zuzel. Modulations of the Cosmic Muon Signal in Ten Years of Borexino Data. ArXiv e-prints 1808.04207, August 2018.

Acknowledgements

First and foremost, I would like to thank my supervisor Prof. Dr. Livia Ludhova for being a constant source of motivation for me throughout the past year. This work would not have been possible without her guidance, patience and never ending enthusiasm for Physics and Geology. I am deeply indebted to Dr. Zara Bagdasarian for being there for me from day one and for always being patient enough to answer even the silly questions I threw at odd hours. I will always be grateful to her for proofreading this thesis, and sprinkling some of her glitter on it. I would like to thank my colleague Mariia Redchuk for bringing more Python into my life and for always offering me random facts that I would not have learnt otherwise. I would also like to thank my colleague Ömer Penek for inquiring about my well being at regular intervals and keeping the work environnment more relaxed. I am grateful to my colleague Dong Han for helping me obtain the results presented in this work. I would like to thank my colleagues from the Borexino Collaboration, especially the antineutrino working group for their expertise and help throughout. I am really grateful to my parents, Kumaran and Vasanthi, and my brother, Aswin for always being there and supporting all my academic endeavors. This section would not be complete if I did not thank my dearest friend and colleague, Rikhav for being my family away from home throughout my Masters.